

FREQUENCY CONTROL IN POWER
SYSTEMS WITH HIGH PENETRATION
OF POWER ELECTRONICS
INTERFACED POWER SOURCES

A THESIS SUBMITTED TO THE UNIVERSITY OF MANCHESTER
FOR THE DEGREE OF DOCTOR OF PHILOSOPHY
IN THE FACULTY OF SCIENCE AND ENGINEERING

2019

Mingyu Sun
School of Engineering
Department of Electrical and Electronic Engineering

Contents

Abstract	13
Declaration	14
Copyright Statement	15
Acknowledgements	16
List of Abbreviations	17
1 Introduction	19
1.1 Background	19
1.2 Motivation	20
1.2.1 Frequency Stability	20
1.2.2 Power System Developments with Renewable Energy Sources	21
1.2.3 Challenges to Traditional Frequency Control	24
1.2.4 Synchronised Measurement Technology	25
1.3 Objectives	26
1.4 Contribution	27
1.5 Outline of the Thesis	29
2 Existing Frequency Control Methods	32
2.1 Introduction	32
2.2 Frequency Control	32
2.2.1 The Scope of Frequency Control	33
2.2.2 Motivation for Frequency Control	34
2.2.3 Frequency Control in the UK	35

2.3	Elements of Existing Frequency Control	36
2.3.1	Primary Control	37
2.3.2	Secondary Control	38
2.3.3	Tertiary Control	39
2.3.4	Under Frequency Load shedding	40
2.4	The Performance of Existing Frequency Control	40
2.5	Chapter Summary	41
3	Power Electronics Interfaces of Renewable Energy Sources	43
3.1	Chapter Introduction	43
3.2	The Principle of Power Electronics in Power System	44
3.3	Power Electronic Converter Topologies	45
3.3.1	Ideal Voltage Source Converter	46
3.3.2	Practical Voltage Source Converter	47
3.3.3	AC and DC Filters	50
3.4	Control of VSC HVDC converter	51
3.4.1	Overview	51
3.4.2	Design of Current Control for VSC	52
3.4.3	Dynamic of the AC Side in Phasor Domain	54
3.4.4	Current Control in $\alpha\beta$ Frame	54
3.4.5	Active and Reactive Power Control of VSC	60
3.5	Simulation of Power Response of a VSC Converter on RTDS	61
3.6	Chapter Summary	62
4	Analysis of Frequency Control in Low-Inertia System	63
4.1	Chapter Introduction	63
4.2	Definition of Inertia in Power System	64
4.3	Transition to Low-Inertia Systems	65
4.3.1	Inertia and Frequency response	66
4.3.2	Inertia Trends and Directions	67
4.3.3	The Rate of Change of Frequency	68
4.4	Frequency Containment with Reduced System Inertia	70
4.4.1	Enhanced Frequency Control	70

4.4.2	Fast Frequency Response	70
4.5	Frequency Response of Low-Inertia Systems	73
4.6	The Impact of High RoCoF on Distributed Generation Operation	75
4.6.1	Reduced 36-Zone GB System Model	77
4.6.2	Modelling of Distributed Generation	78
4.6.3	Modelling of RoCoF Relay and Simulation results	78
4.7	Chapter Summary	81
5	Estimation of the Inertia of a Power System	82
5.1	Chapter Introduction	82
5.2	Defining the Inertia Constant	84
5.3	Estimating inertia constant using the Swing Equation	85
5.3.1	Deriving a Suitable form of the Swing Equation	86
5.3.2	Existing H Estimation Methods	88
5.4	Inertia Calculation Application	89
5.4.1	ICA Execution	90
5.5	Estimation of the Rate of Frequency Change	92
5.6	ICA Testing and Validation Through Computer Simulated Tests	94
5.6.1	Single-machine Test System Case	94
5.6.2	Multi-machine Test System Case	96
5.7	Chapter Summary	99
6	Development of an RTDS Hardware-In-the-Loop Testbed	100
6.1	Chapter Introduction	100
6.2	Real Time Digital Simulation	101
6.3	Hardware and Software Integration	102
6.3.1	Hardware	102
6.3.2	Software	105
6.3.3	Power System Model	106
6.4	Hardware-In-the-Loop Testing Techniques	108
6.4.1	RTS-based Simulation Only	109
6.4.2	Controller Hardware-In-the-Loop (CHIL)	109
6.4.3	Power Hardware-In-the-Loop (PHIL)	110

6.5	Chapter Summary	110
7	Decentralised Adaptive Under Frequency Load Shedding Scheme	111
7.1	Introduction	111
7.2	Principles and Challenges of Applying The Swing Equation To LoG Event Size Estimation	113
7.3	Local Estimation of CoI RoCoF and LoG Event Size	114
7.3.1	Local Estimation of the CoI RoCoF	115
7.3.2	Proposed UFLS Scheme	116
7.4	Performance Evaluation	119
7.4.1	Test System and Relays Settings	120
7.4.2	Accuracy of Local RoCoF Estimation	122
7.4.3	General Evaluation of the Proposed UFLS Scheme	122
7.4.4	Sensitivity to Various Factors	124
7.4.5	An Adjustment Coefficient to Optimize UFLS Performance	126
7.5	Validation in the GB Test System	128
7.6	Chapter Summary	130
8	Fast Frequency Response using Wide Area Monitoring and Control System	132
8.1	Chapter Introduction	132
8.2	Monitoring and Control Scheme	133
8.2.1	Overview of the EFCC Scheme	134
8.2.2	Design of Regional Aggregators (RA)	136
8.2.3	Design of Central Supervisor (CS)	138
8.2.4	Design of Local Controller (LC)	140
8.3	Validation of the EFCC Scheme	143
8.3.1	GB Test System Modelling in RTDS	144
8.3.2	CHIL Validation of the EFCC Scheme	145
8.3.3	Virtual PMUs Placement and PMU's Weight Calculation	145
8.4	Test Description and Cases	147
8.5	Chapter Summary	159

9	Thesis Summary	160
9.1	Conclusion	160
9.2	Future Developments	162
A	Network Data of Test Systems	176
A.1	Kundur’s Two-Area Test System	176
A.2	IEEE 9-Bus Test System	176
A.3	IEEE 39-Bus Test System	181
B	List of Publications	185

Word count 40397

List of Tables

2-1	Operation requirements of GB Grid Code.	36
4-1	Frequency response requirements for the example.	74
5-1	Inertia calculation errors for the single-machine test system.	96
5-2	Results of the estimated inertia of the 3-machine test system.	97
7-1	Specifications of the IEEE 39-bus system in different scenarios.	120
7-2	Specifications of conventional UFLS settings.	122
7-3	Performance of the proposed UFLS scheme.	124
7-4	UFLS triggering instants by different relays.	124
7-5	Frequency nadirs for different RES penetration levels.	126
7-6	UFLS relay placement in GB test system.	129
7-7	Specifications of conventional UFLS settings in GB test system.	130
7-8	Performance of proposed UFLS scheme in GB test system.	130
7-9	Performance of conventional UFLS scheme in GB test system.	131
8-1	EFCC resource information for CHIL test.	146
8-2	PMU placements in GB test system.	147
8-3	Availability of service providers in test case 1.	149
8-4	Availability of service providers in test case 3.	152
A-1	Line data for the Kundur's two-area test network	177
A-2	Load flow data for the Kundur's two-area test network	177
A-3	Generator dynamic data for the Kundur's two-area test network	177
A-4	Synchronous machine parameters	178
A-5	Exciter parameters	179

A-6 Transformer parameters	179
A-7 Line parameters	180
A-8 Load parameters	181
A-9 Transformer Data	182
A-10 Bus Data	183
A-11 Transmission Line Data	184

List of Figures

1-1	Depiction of the main stages of the adaptive frequency control.	27
2-1	Classification of power system frequency stability.	33
2-2	An example of short and long term frequency control.	34
2-3	A block diagram of a TGOV1 governor controller.	38
2-4	Characteristic of primary and secondary control.	39
3-1	A general illustration of power electronics in power system, adapted from [7].	44
3-2	A ideal Voltage Source Converter.	46
3-3	Ideal VSC equipped with DC-side and AC-side filters.	48
3-4	Simplified schematic diagram of the two-level VSC	48
3-5	The pulse-width modulation (PWM) switching strategy.	49
3-6	The modulating signal, carrier signal, and AC-side terminal voltage, based on the SPWM switching strategy [47].	49
3-7	Space phasor in the stationary reference frame.	53
3-8	Practical VSC converter with filters.	54
3-9	Space phasor with the rotating frame.	56
3-10	The dynamics of the AC side current in dq frame.	57
3-11	A block diagram of the current controller for the system.	58
3-12	The Whole block diagram including current controller and control plant in dq -frame.	59
3-13	The decoupled control loop for d -axis.	60
3-14	A block diagram of active power regulator.	60
3-15	A block diagram of reactive power regulator.	61
3-16	Frequency step responses of the converter plant.	61
3-17	Step responses of the AC voltage regulator and active power regulator. . . .	62

4-1	Inertia response for loss of 163 MW generation in IEEE 9-bus system. . . .	66
4-2	System inertia forecast in the GB system [57].	68
4-3	Instantaneous absolute RoCoF, a relationship between absolute loss size and inertia.	69
4-4	Concept for enhanced response service [57].	71
4-5	Simulation of a 500 MW loss of generation in IEEE 39-bus system.	73
4-6	Simulation of a 500 MW generation loss in IEEE 39-bus test system with FFR.	75
4-7	Simulation of a 500 MW generation loss in IEEE 39-bus test system with varying amounts of FFR.	76
4-8	Simulation of a 500 MW generation loss in IEEE 39-bus test system with different time delays of FFR.	76
4-9	Reduced GB 36-zone model in DIgSILENT PowerFactory.	77
4-10	Modelling of Distribution Generators in GB 36-zone system.	78
4-11	Block diagram of the designed RoCoF relay.	79
4-12	Impact of RoCoF relay on frequency response.	80
4-13	Impact of RoCoF relay on system RoCoF.	80
5-1	A generic WAMS architecture that could support the ICA.	90
5-2	Estimated test signal rate of frequency change.	93
5-3	Frequencies for a single-machine test system; the black and grey lines denote a load increase and decrease respectively.	95
5-4	Frequency derivatives for a single-machine test system, the black and grey lines denote a load increase and decrease respectively.	95
5-5	Three-machine, 60 Hz test power system.	97
5-6	Frequency response of COI for tests with the 3-machine tests system. . . .	98
6-1	RTDS cubic and its key components.	101
6-2	RTDS testbed architecture and communication infrastructure.	102
6-3	PQ power source model in phase reference.	107
7-1	Frequency responses and inflection points.	115
7-2	Diagram of Inflection Point Detector.	116

7-3	Comparison of estimated LoG for different inertia levels of the tripped generator.	119
7-4	IEEE 39-bus test system.	121
7-5	The distribution of the RoCoF estimation error.	122
7-6	The frequency response of the proposed UFLS scheme following LoG events of different size.	123
7-7	The frequency response of the proposed UFLS scheme following LoG events of different size.	125
7-8	The frequency response of the proposed UFLS scheme following LoG events of different size.	127
7-9	The frequency response of the proposed UFLS scheme following LoG events of different size.	128
7-10	Single-line diagram of GB test system in RTDS.	129
8-1	Schematic of the design of the EFCC scheme.	135
8-2	Response characteristics of resources	138
8-3	Definition of the pseudo ramp rate	139
8-4	Comparison of detection window on RoCoF	141
8-5	Examples of resource allocation within a region.	142
8-6	Test setup for validation of the EFCC scheme.	143
8-7	Single line diagram of the GB test system.	145
8-8	System frequency response of a 1000 MW load increase event at bus 9 of region 1.	149
8-9	Simulation results of a 1000 MW load increase event at bus 9 of region 1.	149
8-10	Simulation results of a 1000 MW load increase at bus 9 of region 1 with two different service pulling off speed.	150
8-11	Simulation results of a 1000 MW load increase at bus 9 of region 1.	151
8-12	System frequency response of a 1500 MW load increase event at bus 9 of region 1.	151
8-13	Simulation results of a 1500 MW load increase event at bus 9 of region 1.	152
8-14	System frequency of a 1000 MW load increase event at bus 21 of region 2	153
8-15	Simulation results of a 1000 MW load increase event at bus 21 of region 2	153
8-16	Simulation result of a 140 ms single line ground fault at bus 3 of region 1	154

8-17	Voltages measured by PMU during 140 ms single line ground fault at bus 3 of region 1	155
8-18	System frequency of generator tripping after a fault at bus 5 in region 1 . . .	156
8-19	Simulation result of generator tripping after a fault at bus 5 of region 1 . . .	156
8-20	Simulation result of generator tripping after a fault at bus 5 of region 1 (zoomed)	157
8-21	System frequency of different PMU weight configurations	157
8-22	System frequency of different PMU weight configurations (zoomed)	158
8-23	System RoCoF of different PMU weight configurations	158
A-1	Single line diagram of Kundur's two area test system.	176
A-2	Single line diagram of IEEE 9-bus test system.	178
A-3	Single line diagram of IEEE 39-bus test system.	181

Abstract

The University of Manchester

Mingyu Sun

Doctor of Philosophy

Frequency Control in Power Systems with High Penetration of Power Electronics interfaced Power Sources

31 March, 2019

The increased penetration of Power Electronics (PE) interfaced power sources is significantly affecting the dynamic performance of the existing power system. These changes are such that in the future it may no longer be possible to guarantee the security of operation, especially for frequency control. The increased level of uncertainties, particularly the reduction of and variation in system inertia that will be faced in the future, must be resolved through the use of adaptive online solutions to ensure system security and the introduction of novel technologies. This technology is based on the extensive usage of novel sensors and Information and Communication Technology (ICT). The solutions proposed in this thesis are based on the application of Synchronised Measurement Technology (SMT) and Wide Area Monitoring, Protection and Control (WAMPC) type solutions.

The objective of this thesis is to analyse the challenges for existing frequency control methods and to create new frequency control methods. The intent is to contribute to the developments of new corrective control of frequency for future power systems in two ways: online estimation of system inertia and swing equation based adaptive frequency control.

The research presented includes a method for online estimation of the system inertia using wide area measurements. The availability of synchronised measurements will allow it to replace the traditional methods. With estimated system inertia, a decentralised under frequency load shedding scheme is proposed to adaptively adjust load shedding amount using local measurements. This is particularly effective before a complete WAMPC scheme can be established in the system and can act as an important protection scheme in parallel with future WAMPC based frequency control scheme. Furthermore, a fast frequency control scheme using WAMPC is then presented, which uses real-time frequency data from PMUs and determines the required responses. The system takes into account the impact of the frequency event on different parts of the network and allocates responses at a regional level. The characteristics and capabilities of connected resources are considered so that a coordinated and optimised response is dispatched immediately following the event.

A high-fidelity Real Time Digital Simulator (RTDS) based real-time simulation testbed used for the validation process is also constructed and presented in this thesis to facilitate the validation of novel techniques for power system protection and control. Methods proposed in this thesis are validated using the testbed through Controller-In-the-Loop (CIL) and Controller Hardware-In-the-Loop (CHIL) testing techniques.

Declaration

No portion of the work referred to in the thesis has been submitted in support of an application for another degree or qualification of this or any other university or other institute of learning.

Copyright Statement

- i.** The author of this thesis (including any appendices and/or schedules to this thesis) owns certain copyright or related rights in it (the “Copyright”) and s/he has given The University of Manchester certain rights to use such Copyright, including for administrative purposes.
- ii.** Copies of this thesis, either in full or in extracts and whether in hard or electronic copy, may be made **only** in accordance with the Copyright, Designs and Patents Act 1988 (as amended) and regulations issued under it or, where appropriate, in accordance with licensing agreements which the University has from time to time. This page must form part of any such copies made.
- iii.** The ownership of certain Copyright, patents, designs, trade marks and other intellectual property (the “Intellectual Property”) and any reproductions of copyright works in the thesis, for example graphs and tables (“Reproductions”), which may be described in this thesis, may not be owned by the author and may be owned by third parties. Such Intellectual Property and Reproductions cannot and must not be made available for use without the prior written permission of the owner(s) of the relevant Intellectual Property and/or Reproductions.
- iv.** Further information on the conditions under which disclosure, publication and commercialisation of this thesis, the Copyright and any Intellectual Property and/or Reproductions described in it may take place is available in the University IP Policy (see <http://documents.manchester.ac.uk/DocuInfo.aspx?DocID=487>), in any relevant Thesis restriction declarations deposited in the University Library, The University Library’s regulations (see <http://www.manchester.ac.uk/library/aboutus/regulations>) and in The University’s Policy on Presentation of Theses.

Acknowledgements

I would like to express my sincere gratitude to Prof. Vladimir Terzija for providing the funding, supervision, and all the encouragement and support during my PhD study and research.

I would also like to thank Dr Sadegh Azizi for the generous help he has offered to me, and my colleagues for their help in all aspects of my life during my study at The University of Manchester. It has been an honour and a privilege to be part of the research team with all brilliant members.

Finally, although it is impossible to put into words, I would like to take this opportunity to express my gratitude and love to my wife and my parents. Without their love and support, it would have been impossible for me to carry out this PhD research and to finish this thesis.

List of Abbreviations

AC	Alternative Current
AGC	Automatic Generation Control
AUFLS	Adaptive Under Frequency Load Shedding
BJT	Bipolar Junction Transistor
CCGT	Combined Cycle Gas Turbine
CHP	Combined Heat and Power
CIGRE	International Council on Large Electric Systems
CIL	Controller-In-the-Loop
CoI	Centre of Inertia
CS	Central Supervisor
DC	Direct Current
DFIG	Doubly Fed Induction Generator
DG	Distributed Generation
DUT	Device Under Test
EFCC	Enhanced Frequency Control Capability
EMTP	Electromagnetic Transient Simulation Program
EU	European Union
FES	Future Energy Scenario
FFR	Fast Frequency Response
GB	Great Britain
GE	General Electric
GPS	Global Positioning System
HIL	Hardware-In-the-Loop
HVDC	High Voltage Direct Current
ICA	Inertia Calculation Application

IEEE	Institute of Electrical and Electronics Engineers
IGBT	Insulated Gate Bipolar Transistor
IGBT	Insulated Gate Bipolar Transistor
IPD	Inflection Point Detector
LCC	Line Commutated Converter
LoG	Loss of Generation
MCS	Monitoring and Control Scheme
MOSFET	Metal-Oxide-Semiconductor Field-Effect Transistor
NG	National Grid
PE	Power Electronics
PHIL	Power Hardware-In-the-Loop
PLC	Programmable Logic Controller
PMU	Phasor Measurement Unit
PV	Photo Voltaic
PWM	Pulse Width Modulation
RA	Regional Aggregator
RES	Renewable Energy Source
RoCoF	Rate of Change of Frequency
RTDS	Real Time Digital Simulator
RTS	Real Time Simulator
SIPS	System Integrity Protection Scheme
SMT	Synchronised Measurement Technology
SPWM	Sinusoidal PWM
UFLS	Under Frequency Load Shedding
VSC	Voltage Source Converter
WAMC	Wide Area Monitoring and Control
WAMPAC	Wide Area Monitoring Protection And Control
WAMS	Wide Area Monitoring System

Chapter 1

Introduction

This chapter is to present the basic background, motivation, objectives and contributions of this research. The background of this thesis is described in Section 1.1. Section 1.2 provides a brief description of the motivation of this research. The main objectives of the research are presented in Section 1.3, and the contributions made by the research are described in Section 1.4. A short introduction to the organization of thesis is summarised in Section 1.5.

1.1 Background

An electric power system plays an essential role in modern society and provides reliable and safe electricity supply to all consumers. As environmental pollution and climate change have become an international concern, the world is transforming into a low-carbon economy. Many commitments to promote renewable energy have been made through climate change policies worldwide, which often feature specific renewable energy goals [1]. Increasingly ambitious climate targets in some countries will require action across all energy end-use sectors. In 2017, 25 C40 member cities from across the world established goals to reach net-zero emissions by 2050 [2]. In the United States, the nine northeast states that make up the Regional Greenhouse Gas Initiative agreed to reduce 75 per cent of power-sector CO₂ emissions across the region by 2030 [3]. In China, a target of generating over 15 per cent of its total power from renewable energy by 2020 with 420 GW of hydro, 50 GW solar, 200 GW of wind, 30 GW of biomass has been revealed [2]. In Europe [4], up to 75 per cent of the total demand is forecasted to be supplied by Renewable Energy Sources (RES) by 2050.

In the United Kingdom, National Grid's Electricity Ten Year Statement (ETYS) [5] has

demonstrated four Future Energy Scenarios (FES) which represent GB networks with different speeds of decarbonisation and levels of decentralisation in the future. Among the four scenarios, the Community Renewables and Two Degrees cases are particularly interesting for this research because of the massive development of renewable energy and new technologies. In both cases, the UK 2050 emission target of reducing 80 per cent greenhouse gas can be achieved, indicating a massive need to increase RES in the system. A number of scenarios for 2050 see up to 75 per cent of final energy consumption coming from RES [6].

Despite the clean energy supplied by RES, there are also challenges brought by the growing penetration of RES. Most of the RES like Photo Voltaic (PV), Wind Turbine and Energy Storage are connected through Power Electronic (PE) converter. The converter decouples the RES from the system [7], while the rotating parts of conventional machines inherently provide inertia to the system. So replacing conventional sources with RES will reduce the inertia of the whole power system. The reduced system inertia can lead to critical frequency security issues like higher Rate of Change of Frequency (RoCoF) and lower frequency nadir in case of an under-frequency event. It has been widely studied and discussed that such critical issues cannot be addressed within the confines of the existing electricity grid [8].

1.2 Motivation

1.2.1 Frequency Stability

Frequency stability is defined as: "the ability of a power system to maintain steady frequency following a severe system upset resulting in a significant imbalance between generation and load" by a joint IEEE/CIGRE working group in [9]. Therefore, frequency control strategies are designed to secure the frequency stability of a power system.

The stability of frequencies is necessary to be maintained because the frequency of a power system is a crucial index of a power system. The balance between the active power of the generation and demand in the system is reflected through frequency. Any event that interferes with this active power balance will, therefore, cause the frequency to deviate from the nominal value. Such disturbances include the loss or de-loading of a generator and a sudden increase or decrease in the demand.

Many power system elements' normal operations depend on the frequency of the power

they are supplied with. For example, generator turbine blades experience cumulative physical damage when it is operating at a frequency which is over 2.5 Hz from the nominal value. Many auxiliary functions in a power plant are driven by induction motors, and those motors will slow down in an under-frequency event, may affect the operational security [10]. Therefore, a substantial deviation from nominal can cause the behaviour of many system elements to vary dramatically from their designed behaviour and resulting in cascading failures which further stress the power system, exacerbate the frequency deviation and eventually lead to blackout [11].

However, with the growing proportion of PE-interfaced RES, it may no longer be possible to guarantee the security of power supply with the traditional frequency control strategy. The increased uncertainty and the reduction of system inertia must be overcome through a smarter solution with new techniques. In future power systems, because the increasing levels of uncertainty that will be encountered in the future can seriously undermine traditional deterministic frequency control, it is vital to develop an adaptive method to overcome the issues [12]. Modern technologies such as synchronised phasor measurement, fast and secure communication capabilities allow the development of unexplored solutions against new brought challenges [13]. Applications based on those technologies like Fast Frequency Response and Wide Area Monitoring Protection and Control (WAMPC) have become an area of great interest.

1.2.2 Power System Developments with Renewable Energy Sources

Renewable energy is generally defined as energy that is collected from resources which are naturally replenished on a human timescale, such as sunlight, wind, rain, tides, waves, and geothermal heat [14]. The RES can either be installed at transmission level with large capacities or in the distribution level on a smaller scale. Distributed Generation (DG) connected to the distribution network is referred to as Distributed Energy Resources (DER) [1].

RES typically includes hydro, biomass, biogas, solar power, wind power, and geothermal power. Grid-connected electricity storage can also be classified as a RES system. The technologies which use converter as interfaces like wind power, solar power, energy storage, and High Voltage Direct Current (HVDC) are briefly introduced in the following sections to give an overview of its principle and the impact on the system.

Wind Power

Wind power is widely used in around the world. From 2004 to 2017, the worldwide installed capacity of wind power has been growing from 47 GW to 539 GW - a more than 1000 per cent increase within 13 years [1], [15]. Offshore wind energy sources are currently one of the most expensive energy technologies. The total cost of offshore wind farms is 90 per cent more expensive than conventional gas turbines and 50 per cent more expensive than nuclear plants [16]. This high expense is a result of the technical difficulties of offshore turbine construction and connection to the onshore grid. Extra construction and materials are needed to set up turbines in the sea, and the investment in new offshore technologies is also attributed to this cost [7]. Onshore wind energy, on the other hand, is the most cost-effective renewable energy source around.

Wind turbine generation is often designed to use either fixed speed or variable speed units. Fixed speed wind turbines are usually manufactured in the early days. The nature of the fixed speed induction generators, like squirrel cage induction generators, suffer from poor energy efficiency and need to equip capacitor banks at the terminal as they have no reactive power control capability [17]. The weaknesses of the fixed speed turbine are the driver of the development of variable speed units. Two forms of widely implemented variable wind speed turbine are Doubly Fed Induction Generators (DFIGs) and Permanent Magnet Synchronous Machines (PMSMs); Both types of wind turbines have taken great advantage of the development of Power Electronics converters.

A DFIG uses a power electronic converter to interface with the rotor winding of the induction generator and supplies power directly to the grid. The PE converter controls the speed of the induction machine through the frequency of the rotor current. DFIG is currently the preferred technology for large wind farms as it costs less due to the smaller scale of PE converter, 20 per cent to 30 per cent of the DFIG rating. While, the converter used in a PMSM needs to be rated at 100 per cent of the rating of the PMSM, making a significant difference in the cost [18].

Solar Power and Energy Storage

While solar power is one of the fastest growing sources of RES, the power it produces is usually intermittent during the day and completely unavailable in the night. One important

nature of the power system is that the energy must be consumed as much as generated and cannot be easily stored. So solar power and energy storage can make a great combination while the energy storage absorbs the excessive power from solar during the day and continue to supply power in the night. The whole system is also connected through the PE interface so that it has the potential to offer valuable services to the system.

For the energy storage of the system, there are two main applications. One is the peak shifting, utilised to shift power from peak time to off-peak time. The other one, which is more interesting to this thesis, is that it can contribute to system frequency regulation for fast frequency response [19]–[21].

High Voltage Direct Current (HVDC) Transmission

For long-distance transmission and underwater interconnector, HVDC technology is increasingly applied in the modern power system. HVDC is a cost-effective way to transfer energy for the distance above 70 to 100 kilometres [22], which is quite suitable for the off-shore transmission system. Secondly, as it uses the PE converter to connect AC and DC networks, it can also be used to connect isolated system areas. The capacity level in GB has increased considerably in the past, and the current interconnector capacity level for GB is 3.8 GW. According to National Grid's Future Energy Scenarios, this level will continue to grow to 25 - 30 GW by 2030 [5]. Similarly, the converter used by the HVDC system could contribute to system frequency regulation like other PE-interfaced RES [23].

Demand Side Response

The Demand Side Response (DSR) is defined as a deliberate change to an end user's natural pattern of metered electricity consumption by a signal from another party [24]. The core concept behind DSR is that the loads change itself in real time to support the system operation and control. Ideal DSR loads are thermal loads or energy storage units like Electric Vehicles which is flexible and controllable by their nature. It can be used both for peak shifting and frequency control. To enable DSR to participate in frequency control, more advanced communication and control infrastructure needs to be implemented in the system [24], [25].

Distributed Generation

Generation connected to the distribution networks has been an area of significant growth in recent years, encouraged by the government's support for low carbon technologies [21], [26]. In the future, the capacity level of Distributed Generation installed in the GB system will be significant. The capacity of distributed wind turbines and solar power is forecasted to be 8 GW and 10 GW by 2035, and the total distributed capacity of all DGs is expected to be 27.5 GW by 2035 [5].

1.2.3 Challenges to Traditional Frequency Control

Since the existing electricity grid has been developed in various parts of the world during the past century, similar technologies are generally adopted by different countries and utility companies. The basic topology of the electrical power system has remained unchanged with clear differentiation between generation, transmission, and distribution subsystems. So in such a strictly hierarchical system, the source has no real-time information about the service status of demand. The utility companies operate the system at the transmission level, and the distribution network remains outside of real-time control. For instance, in North America, which has established one of the world's most advanced electrical power systems, less than a quarter of the distribution network is equipped with information and communications systems, and the distribution automation penetration at the system feeder level is estimated to be only 15 per cent to 20 per cent.

In the new century, RES have attracted considerable interest in power system developments and have grown significantly while the traditional generation such as gas turbines and nuclear power plants will continue to play an essential role in ensuring the security of supply. If we compare the total energy output and the installed capacity of conventional generation and RES, the total energy output of traditional generation accounts more than that in the capacity, which reflects the nature of renewable energy. The reason behind is that RES such as solar power and wind power is by its nature intermittent and not stable for the long term, which address both the need of traditional generator support and new technology to overcome this disadvantage.

The primary influence of renewable energy to power system frequency control is the reduction of system inertia and conventional generation reserves. The PE converter used

by RES decouples itself from the system, so it cannot interact with the system during the frequency disturbance event in a way like the inertial and governor response from conventional synchronous generators. Furthermore, due to the regulation of distribution grid code, RoCoF relay of DG may mistakenly trip itself during the frequency event because of higher RoCoF it measured, which can potentially lead the system to even worse condition. Rather than the current preference of large centralised generating units, DG can result in more problematic frequency control in the future power system due to the lack of its operational information [27].

However, it can also be seen as an opportunity to the system frequency security because that RES like wind farm, PV, energy storage, plus DSR can quickly change their output to respond to disturbances [19], [28]. So a supplementary controller can be designed to bring this to life. This technique is often referred to as synthetic inertia or fast frequency response [29], [30].

1.2.4 Synchronised Measurement Technology

Conventional measuring devices in the power system usually has a report rate of less than 1 Hz, which significantly limited the modern power system protection and control development. Nevertheless, measurements from different devices are not aligned with a unified time source, which brings further challenges. As the technology of GPS and other satellite-based timing system came in mature, Synchronised Measurement Technology (SMT) such as Phasor Measurement Unit (PMU) has shown a great advantage of a much higher reporting rate at 50/60 Hz with all measurements aligned with the same timing source. It has then been a key enabler of the wide area monitoring, protection and control (WAMPAC) systems which is very much desired by many power system operators [31]. A number of recently proposed frequency control methods such as fast frequency control, adaptive under frequency load shedding are only feasible if sufficient SMT is available to provide accurate time-stamped measurements of phasors, frequency and many other signals in the system.

With the SMT, a real time monitoring system would be readily available to the system operator and applications can be built upon the data such as oscillation detection, stability monitoring, dynamic state estimator and fast frequency control.

Despite all the benefits and advantages brought by the SMT and WAMPAC system, there are several practical challenges to be overcome. Communication network is one of the

key components of WAMPAC that determines the successful operation of those WAMPAC based methods. It grants fast and reliable data transmission and provides data storage and concentration tools which supply information gathered by SMT to new control methods and applications [32]. The speed of data transmission and the extraction of grid information will be critical factors in determining the success of any power system monitoring and control applications, as any correction must be acted sufficiently fast to allow the disturbance to be contained. However due to the slow adaptation of the fast communication network, many WAMPAC based novel system control, especially closed loop control, has not yet been widely adopted in many countries. Therefore, it is interesting to study methods that rely on a limited communication infrastructure and limited number of PMUs.

1.3 Objectives

The main objective of the research presented in this thesis is to create improved frequency control methods including Fast Frequency Response and Adaptive Under Frequency Load Shedding in a power system with high penetration of RES. This research intends to contribute to the development of adaptive control of frequency for future power systems in two ways: online estimation of system inertia and adaptive frequency control using estimated system inertia.

On the other hand, as secured operation and control of power system requires an increasing number of different types of equipment, testing of these types of equipment and devices is vital and necessary during the design stage before any implementation in the system. Verification of its interaction with the rest of the power system under a real or high-fidelity environment is crucially important. Therefore, besides creating new frequency control methods, another goal of this research is to construct a Real Time Digital Simulator (RTDS) testbed, which can perform real-time digital simulation and Hardware-In-the-Loop (HIL) testing. The RTDS HIL testbed is then used to conduct the validation of the proposed methods in this thesis.

The detailed objectives of this research can be summarised:

- Assess the impact of reduced system inertia on existing frequency control.
- Create a method for estimating the inertia of a power system.

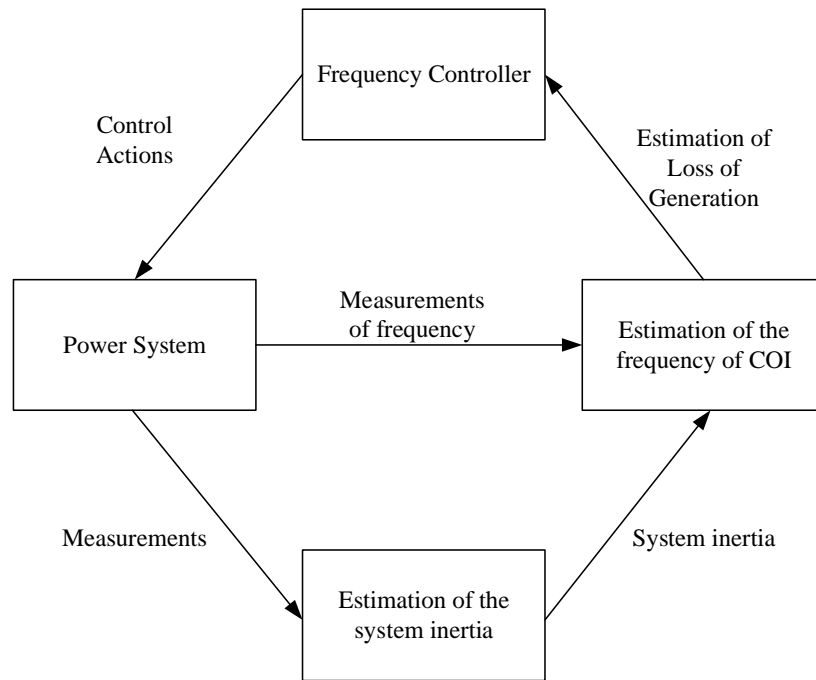


Figure 1-1: Depiction of the main stages of the adaptive frequency control.

- Create a method for adaptive UFLS using local measurement.
- Investigate the use of wide area monitoring measurements for frequency control.
- Construct a real-time simulation testbed for the validation of proposed methods.
- Validate the methods created in this thesis using DigSILENT PowerFactory and RTDS HIL testbed.

1.4 Contribution

The research presented in this thesis focuses on the creation of local and wide-area monitoring and control methods to conduct emergency frequency control for power systems with high penetrations of PE interfaced RES. The major contributions of this research can be concluded as follows:

Assessment of the impact of reduced system inertia on existing frequency control

By reviewing the existing methods of frequency control and the developments in power systems and power electronic technology, the challenges of current practices and the necessity of the new algorithm are addressed. The critical elements of this are summarised:

- The system inertia and the reserve of conventional units are both reduced because of high penetration of RES, resulting in less capable of handling active power deficit in the system.
- Traditional control methods as primary control and secondary control are limited due to the decommissioning of synchronous generators.
- Traditional emergency control such as UFLS is not suitable for the future grid as the settings are based on offline study and not adaptive to the varied inertia of the system.

Creation of an on-line method for estimating the inertia of a power system

Creation of an online method for the estimation of the inertia of that system (Chapter 5). This method takes advantage of the wide area measurement and swing equation. The key benefits are:

- The availability of synchronised measurements can enable new emerging methods to replace the traditional methods of estimating system inertia which are usually offline and post-event.
- The inertia is an essential parameter in evaluating the initial frequency disturbance and responding to it. Therefore, online estimation of system inertia is an enabler technology for any proposed adaptive frequency control methods to be realised.

Creation of an adaptive UFLS scheme using local estimated CoI frequency

Feed by estimated system inertia, an adaptive UFLS is proposed using a local CoI RoCoF estimation technique. The key contributions are:

- A method is created to estimate the frequency and RoCoF of the CoI of the system using local measurement.
- Based on system inertia and RoCoF, a method to estimate the Loss of Generation (LoG) is created.
- By knowing the LoG, an adaptive UFLS strategy is designed, to shed a portion of the estimated LoG to achieve an effective frequency containment.

Validation of a Fast Frequency Control using WAMS using HIL testing

A HIL testing methodology for WAMS is developed and a novel Wide-Area Monitoring and Control (WAMC) system, termed “Enhanced Frequency Control Capability (EFCC)” is validated. Frequency control challenges and the need for faster frequency response are addressed with consideration of the regional impact of events and the coordination of a range of different resources for responding on a localised basis.

- The scheme uses real-time data from PMUs installed at both transmission and distribution levels for monitoring the network and determining the required responses.
- The system takes into account the impact of the frequency event on different parts of the network and allocates responses at a regional level. The characteristics and capabilities of different connected resources are considered. So a coordinated and optimised response is dispatched immediately following the event, offering effective and enhanced frequency control for low-inertia power systems.

Creation of Real Time Digital Simulator based testbed for HIL testing and validation of new power system techniques

A high fidelity RTDS based real time simulation testbed is constructed in the lab to facilitate the simulation and validation of proposed frequency control methods, using Controller-in-the-loop (CIL) and Hardware-in-the-Loop (HIL) techniques. Algorithms or devices under test are verified through real-time simulation in a closed loop manner.

1.5 Outline of the Thesis

Chapter 2 – Existing Frequency Control Methods

This chapter describes the mechanisms used for frequency control and the motivation behind those methods. Profound understanding of the operation of frequency control and its challenges are critical for proposing new frequency control methods to be capable of overcoming the challenges of the future system.

Chapter 3 – Power Electronics Interfaces of Renewable Energy Sources

This chapter provides a review of the fundamental theories of Power Electronics converter used by RES including the modelling, control strategy, and challenges and potential benefit for frequency control of VSC converter. Understanding of concepts introduced in this chapter is the foundation for developments of new methods and algorithms which are discussed in later chapters.

Chapter 4 – Analysis of Frequency Control in Low-Inertia System

This chapter presents how system inertia evolves as the power system develops in the future. The impact of reduced system inertia on the frequency control and the effectiveness of current frequency containment methods are discussed.

Chapter 5 – Estimation of the Inertia of a Power system

This chapter describes the development of a new algorithm for accurate and reliable system inertia estimation based on wide area frequency and active power measurements. A discussion of the method and its challenges of estimating RoCoF is also presented.

Chapter 6 – Development of an RTDS Hardware-In-the-Loop Testbed

This chapter describes a Real Time Digital Simulator based testbed for the testing and validation using high-fidelity real-time models to facilitate the simulation and validation of proposed frequency control methods.

Chapter 7 – Decentralised Adaptive Under Frequency Load Shedding Scheme

In this chapter, a novel decentralised adaptive Under Frequency Load Shedding (UFLS) strategy which has the capability of estimating Centre of Inertia (CoI) RoCoF and the Loss of Generation (LoG) locally. An algorithm is introduced to remove the effect of local frequency oscillation and to identify the CoI frequency and RoCoF of CoI based on local measurement. Based on system inertia and RoCoF, a method to estimate the amount of Loss of Generation (LoG) is created. In the end, a 4-step UFLS strategy is designed, to shed a portion of the estimated LoG to achieve an effective frequency containment.

Chapter 8 – Fast Frequency Response using Wide Area Monitoring and Control System

This chapter presents the design and validation of a novel Wide Area Monitoring Protection and Control (WAMPAC) system, termed “Enhanced Frequency Control Capability (EFCC)”. The scheme uses real-time data from PMUs for monitoring the network and determining the required responses. The system takes into account the impact of the frequency event on different parts of the network and allocates responses at a regional level. The characteristics and capabilities of different connected resources are considered, so that a coordinated and optimised response is dispatched immediately following the event, thereby providing effective and enhanced frequency control for low-inertia power systems.

Chapter 9 – Thesis Summary

This chapter presents the conclusions and summarises highlights the main contributions. Possible suggestions for future research are proposed.

Chapter 2

Existing Frequency Control Methods

2.1 Introduction

This chapter provides a detailed description of the motivation for frequency control and its implementation in modern power systems. Section 2.1 discusses the importance of developing an understanding of frequency control before attempting to create new methods. The importance of the role played by frequency control in power systems is discussed in Section 2.2, while Section 2.3 describes the practical implementation of frequency control. Finally, Section 2.4 describes the success enjoyed by frequency control in the current operating environment and the challenge of new power system developments. Section 2.5 summarises the elements of this chapter that are most relevant to the objectives of the thesis.

This knowledge is necessary to further understand the challenges faced by frequency control. This understanding could then be used to inform the design of the new control methods presented in this thesis.

2.2 Frequency Control

There are three main categories of stability in power systems: voltage stability, rotor angle stability and frequency stability [10]. Frequency control is controlling schemes designed to ensure the balance of active power in the system and frequency stability, which is defined as: "the ability of a power system to maintain steady frequency following a severe system upset resulting in a significant imbalance between generation and load" by a joint IEEE/CIGRE

working group in [9]. The role that frequency control plays in ensuring the frequency stability of a power system means that providing satisfactory frequency control is one of the key tasks of a system operator.

2.2.1 The Scope of Frequency Control

The responsibility of frequency control is to balance the second through second load and generation changes occurring in a power system and to ensure that the frequency is about nominal throughout the day. Continuous frequency control services, also referred to as long term frequency control, in the modern power system have successfully accomplished this task.

In addition, it is the responsibility of frequency control to limit the frequency deviation following a significant disturbance to the active power balance in the system, e.g. the loss of a generator and to return the frequency back to the nominal value within the required time. This type of frequency control is usually classified as short term or occasional frequency control services. The two types of frequency deviation can be explained by Figure 2-1.

The difference between occasional and continuous services is represented in Figure 2-2. For longer periods, it is not the task of frequency control to balance the more significant variations in load that occur in the system on the time scale of hours or days. These changes in larger time scale are accommodated by dispatching the system generation through market-based power balancing mechanisms.

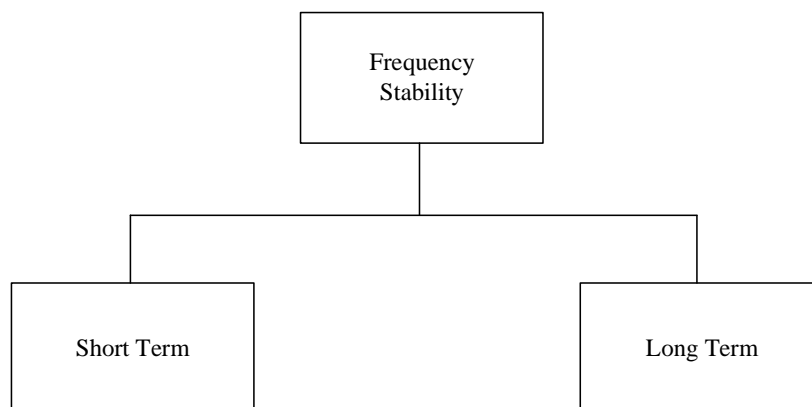


Figure 2-1: Classification of power system frequency stability.

2.2.2 Motivation for Frequency Control

Power systems are complex systems vulnerable to a wide variety of disruptions. Active power disturbances are of significant concern to the frequency control because of the relationship between frequency and the active power balance discussed in the previous section. Any excess or deficit of active power generation such as loss of generation units, load centre and interconnectors could cause a significant frequency deviation from the nominal value [33].

Power systems are designed to operate in a narrow range near nominal frequency. Many elements of the power system will begin to experience non-standard operation and possibly being damaged if forced to operate at a frequency that is over or below its operational limits. The threat of frequency instability caused by improper operation at the non-nominal frequency is the origin of the motivation for frequency control in power systems.

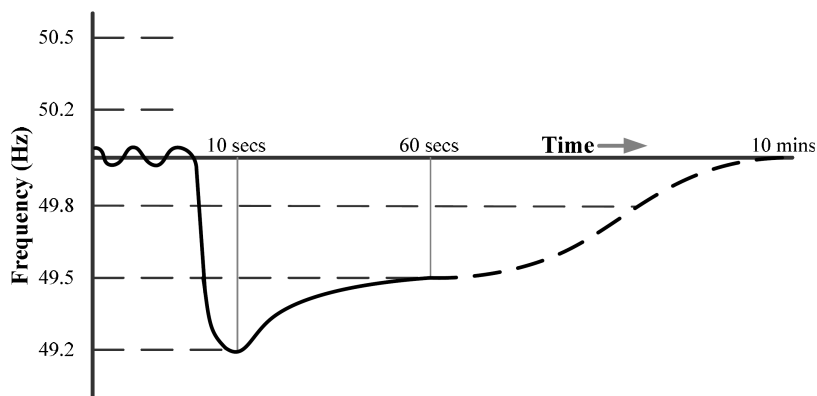


Figure 2-2: An example of short and long term frequency control.

The frequency deviation, however, can potentially lead to a more significant disturbance across the system. For example, some generators might be tripped during an under-frequency event by its protection relay [34]. The consequences of such an event will further enlarge the active power imbalance in the system which means a further deviation of the system frequency [9]. Again, the lower frequency could initiate more generators to be tripped. This procedure will continue until the system is no longer capable of maintaining stability and then a blackout is inevitable unless corrective control actions such as under frequency load shedding and controlled islanding are deployed. This cascading event is usually initiated by the loss of an older steam turbine unit with less robust operation stability against frequency deviations than those modern generator designs [34].

Therefore, low-frequency conditions are considered to be more severe than high-frequency conditions in a power system. For a high-frequency event, any additional loss of a generator tripped by high frequency, the loss of generation will contribute to correct the imbalance instead of exacerbating it in a low-frequency event [33].

It is reported [11], [35] that in some recent blackouts, frequency instability has played a role and can pose a problem in both densely meshed and lightly meshed power systems. However, in isolated systems, the threat of frequency instability is more significant as they have access through tie - lines to fewer external generation resources. Large systems tend to have more substantial inertia which will limit the rate of change of frequency in case of a large frequency event. Additionally, the frequency varies across the system because it can take one to three seconds for the frequency disturbance to spread over the power system which technically allows more time for frequency control to participate.

2.2.3 Frequency Control in the UK

Practices of frequency control differ significantly between the various power systems in the world. In this section frequency regulation in the GB transmission system are described as an example.

The National Grid (NG) is responsible for the operation of the transmission network in the Great Britain. National Grid's primary control has three components [36]: Primary Response, Secondary Response and High Frequency Response. The primary response must be available within ten seconds; the secondary response must be available within thirty seconds and continuing for up to 30 minutes. A speed of 10 seconds and indefinitely sustainability is required for a high frequency response. The details of what each of these response stages involves are described in the next section, but it is important to recognise here the short time frames in which frequency control is expected to operate.

National Grid's frequency control regulation is described in the Grid Code [36], defining the duties for different participating units like large power stations, network operators, PE converter stations, providers of ancillary services and any externally interconnected system operators. The nominal frequency of the GB system is 50 Hz with a ± 0.5 Hz margin. The frequency control thresholds and operational limits used by National Grid are presented in Table 2-1, and this highlights the narrow range that the power system frequency must be kept within. It is clearly noted that the requirement for severe under frequency event is

much stricter than over frequency event.

Table 2-1: Operation requirements of GB Grid Code.

Frequency Range	Requirement
51.5 Hz - 52.0 Hz	Operation for at least 15 minutes is required each time the frequency is above 51.5 Hz.
51.0 Hz - 51.5 Hz	Operation for at least 90 minutes is required each time the frequency is above 51 Hz.
49.0 Hz - 51.0 Hz	Continuous operation is required.
47.5 Hz - 49.0 Hz	Operation for at least 90 minutes is required each time the frequency is below 49 Hz.
47.0 Hz - 47.5 Hz	Operation for at least 20 seconds is required each time the frequency is below 47.5 Hz.

Frequency control services are treated as a commodity, and therefore the value of any service that is offered by a generator must be defined. The methods used to define the frequency services offered include [37]: benchmarking of the actual service provided by a unit through online monitoring and assessment, measuring the dynamic response of service, and testing of units to identify the service that can be expected from them and the frequency region in which this service can be delivered.

The sources of reserve and other frequency services used are [37]: partially-loaded steam plants, pumped storage plants, partially-loaded gas turbines, open cycle and combined cycle gas turbines, interconnections with external systems, and loads with frequency activated relays. Loads with frequency activated relays constitute the system's ability to perform Under Frequency Load Shedding (UFLS), and these relays use the absolute magnitude of frequency as thresholds to trigger their operation.

Minimum frequency response provisions for new build generation units have been imposed to try to ensure that as the system develops the available frequency response services continue to be sufficient. It is required that frequency response capability is 10 per cent and minimum de-load capability is 65 per cent in terms of the generators rated capacity [36].

2.3 Elements of Existing Frequency Control

The frequency control services available to the operator of the transmission system are divided into three levels of control which are primary control, secondary control and tertiary

control [9], [38]. These levels of control include different speed of response and the sustainable time of the service. The combination of different characteristics of each control will allow the frequency across the entire system to be managed and emergency actions that can be called upon as a last resort to limit the size and duration of any large frequency excursions that develop.

2.3.1 Primary Control

The purpose of the primary frequency control is to restore the balance between the power generation and demand in responding to a frequency deviation within a few seconds. The governor of the generator provides the primary control. A sudden power imbalance in the system results in a change of the electrical loading and electrical torque of a generator which slows down the rotor speed of that generator. This change in rotor speed will act as an input to the governor to control the output of the generator.

This change of the output of the generator is achieved by comparing the measured rotor speed to the reference, e.g. nominal rotor speed, to calculate and detect any deviation. Any deviation in speed signal can then be used to determine the adjustment for the mechanical power input of the generator. This adjustment will correct the power imbalance seen at the generator terminals and reduce the speed deviation. A block diagram of a typical governor can be seen in Figure 2-3.

In the case of multiple generators participating in primary frequency control, generators must operate at the same frequency or those generators would act against each other, attempting to control the system frequency to their frequency set point [37]. To avoid such undesired response, speed droop is another key input signal to the governor of the generator. The droop R is defined as the change in frequency, f , normalised to the nominal frequency, f_n , divided by the change in power output, P , normalised to a given power base, P_n . The inverse of the droop is referred to as the stiffness of the generator.

$$\frac{\Delta f}{f_n} / \frac{\Delta P}{P_n} = R \quad (2-1)$$

The use of speed droop allows units with different characteristics to move to the same new frequency balance by distributing the total active power imbalance in the system between the units with the same speed change in each unit. The units with a smaller droop will take over more load, and vice versa. The speed droop characteristic of a generator is

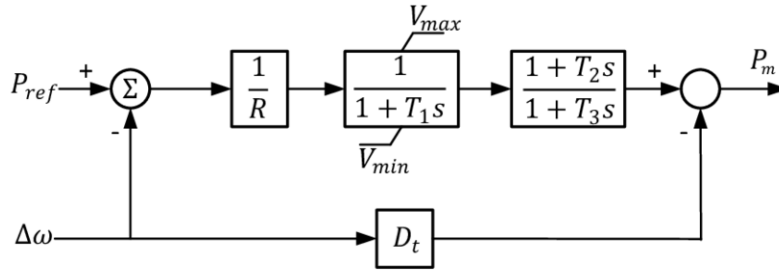


Figure 2-3: A block diagram of a TGOV1 governor controller.

implemented through a feedback loop in the generator control system and implemented in the governor model. This takes the form of the previous change in primary energy input being used to reduce the change in speed signal seen by the governor. In a simplified block diagram of a type TGOV1 governor [39], this is represented by dividing the subtract of the reference signal and speed deviation by the value of the generator speed droop, as seen in Figure 2-3.

However, for a significant disturbance and speed deviation, this mechanism does have its own disadvantages as the need of a large change in system generation could lead a unit to reach its maximum output. This would result that this unit would become unavailable for droop response and a different, potentially less stiff, unit would be relied upon.

On the other hand, system loads are also sensitive to a change in frequency. However, the response of the loads to frequency changes is far less significant than the generators. For example, when comparing the typical stiffness of loads, $K_L = 0.5 - 3$ and typical stiffness of generators $K_T = 20$ as given in [37].

2.3.2 Secondary Control

The purpose of the secondary control is to restore the system frequency to the nominal with consideration of the power flow limit of transmission lines in the system. Secondary control is necessary and essential because the primary control can only limit the deviation of the frequency and is not capable of correcting it because of the speed droop [40].

This secondary control is achieved by moving the load reference set point of generation units to allow an extra offset to the original setpoints, returning the frequency back to the nominal value. A combined process of primary and secondary control can be shown in Figure 2-4. We assume an active power deficit in the system, the system frequency will start

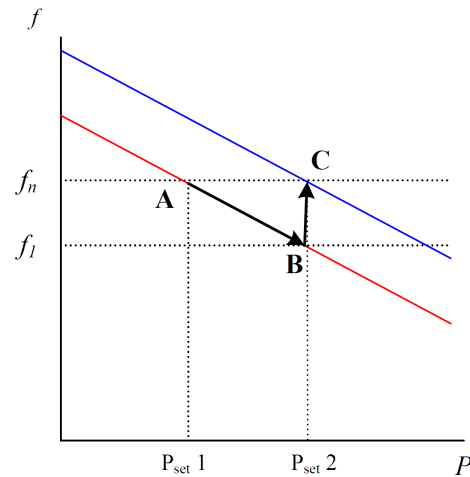


Figure 2-4: Characteristic of primary and secondary control.

to fall from point A, and the primary control will start to act to limit the frequency to f_1 at position B along the red line which is the droop characteristic. As the frequency settles down, the secondary control then moves the power setpoint of the generator from position $P_{set,1}$ to $P_{set,2}$ so the droop characteristic will shift to its right side and its new position is marked in blue. Based on the principle of droop control, the speed of generator will then increase accordingly to return to its nominal value, f_n , at position C.

Droop characteristic shifting and setpoint moving in this way are achieved by adding an offset in the load reference of generators. This additional feedback causes the controller to see an additional speed deviation that is larger than the one there is. The response to this new deviation allows the speed of the generator to be returned to nominal while generating more power.

2.3.3 Tertiary Control

Tertiary control is different from primary and secondary control because it does not deal directly with controlling the frequency. Instead, the main purpose of tertiary control is to re-balance the dispatch of generation units so that the resources can provide sufficient primary and secondary control as defined in the Grid Code. Tertiary control starts to participate after the system frequency has been contained and return to the nominal range. During normal operation, tertiary control can also be utilised to balance the reserves of all generation units in preparation of any further events. Therefore, tertiary control will not be the key focus of this research.

2.3.4 Under Frequency Load shedding

Under frequency load shedding (UFLS) is a common technology [33], [41]–[43] as a last resort for a power system to prevent system collapse and blackout from significant under frequency events that may result in cascading events. Unlike the other frequency control discussed in the previous section, UFLS is an emergency service and is therefore only responsible for ensuring that frequency stability is preserved after severe contingencies. It should be noted that smaller frequency events that the other frequency control services could deal with should not trigger the UFLS scheme.

A typical UFLS scheme automatically disconnects load if the frequency behaviour violates certain thresholds and is usually executed in predefined stages rather than all at once. The thresholds for load shedding stages are determined based on many factors and parameters in the system, including the frequency, the RoCoF, or frequency with certain time delay, a relationship between RoCoF and frequency, or a combination of the above.

Voltage magnitude in the system and the status of key feeders are also considered by some proposed load shedding schemes [44] to adjust the amount and timing of the load shedding. UFLS schemes that use these sorts of additional inputs are usually referred to as Adaptive Under Frequency Load Shedding (AUFLS).

The load shedding usually starts to shed low-value loads or loads that have agreed to be used for this purpose at the first few stages. The loads shed can usually be separated into two categories; these are firm load and probabilistic load. A firm load has a dependable load profile. When a firm load is shed the actual reduction in load is reliable. A probabilistic load does not have such a dependable profile and therefore a large number of these loads are usually grouped to act as one aggregated load to be shed. This aggregation ensures a good (above 90 per cent) [40] chance of the desired amount of load being shed when the instruction is given, making probabilistic loads a useful part of under frequency load shedding.

2.4 The Performance of Existing Frequency Control

The existing preventative frequency control has allowed very few reportable frequency excursions to occur, e.g. one frequency excursion occurred in the power system of Great Britain between 2005 and 2010 [45]. However, the limited occurrence of large frequency

disturbance has contributed to several recent wide-area blackouts. For example, frequency conditions were normal prior to the 2003 blackout in the United States and Canada but the initial frequency swings that occurred played a significant role in allowing the initial disturbance to propagate through the system [46].

The success of current control measures is dependent on the consistent nature of existing power systems, i.e. the parameters of system models are relatively reliable. However, developments in the nature of power systems, discussed in Chapter 1 and the introduction of PE interfaced generators discussed in the next chapter, will erode this consistency, compromising the success of the existing preventative control. For example, it is vital to keep in mind that over shedding of UFLS scheme is always an issue because the total amount of load shedding is not usually controllable. Each UFLS relay operates based on its local frequency measurement without knowing the full situation of the system. As the penetration of renewable energy grows, the reduced inertia and the imposed higher RoCoF during the under-frequency event may increase the risk causing maloperation of existing UFLS schemes and other protections.

2.5 Chapter Summary

This chapter has introduced the principle of system frequency stability and control, and explained the relationship between frequency and active power balance in the system. Frequency stability is maintained using two mechanisms: Power balancing and frequency control. Power dispatch balancing uses a variety of mechanisms to ensure in the long term there is sufficient generation available to satisfy the forecasted demand during the planning period. The time frame used by power balancing means that it is not specifically relevant to the subject of this thesis.

On the other hand, frequency control is responsible for ensuring that the system can accommodate the constant changes in load as well as any large disturbances to the active power balance. The frequency deviations from the constant changes in load are accommodated using continuous services while large disturbances are contained using occasional services. Such frequency control services can be divided into the primary response which is fast and local, and the secondary response and the tertiary response which are slower and used to return the frequency to nominal and resort to a balanced system dispatch.

The time frame of the operation of the primary response is required within ten seconds according to the Grid Code. Any newly proposed frequency control method should also fit into this constraint and act within a shorter time.

As the penetration of renewable energy grows, the reduced inertia and the imposed higher RoCoF during a under-frequency event may increase the risk causing failure and maloperation of existing frequency control methods. Without the provision of sufficient ancillary services to support frequency control, a power system will be vulnerable to the cascading loss of generators and blackouts. Therefore, it is vital that any frequency control method should satisfy the dual requirements of security and dependability, especially for developing any new frequency control method.

Chapter 3

Power Electronics Interfaces of Renewable Energy Sources

This chapter provides a review of the fundamental theories of Power Electronics converter used by RES. Section 3.1 discusses the importance of understanding the principle of PE converter. The history and principle of PE are presented in Section 3.2, while Section 3.3 and Section 3.4 describes the practical modelling and implementation of a Voltage Source Converter (VSC) converter. Finally, Section 3.5 describes the design of the control strategy and the potential capability of frequency support.

3.1 Chapter Introduction

After a discussion of existing frequency control in modern power system and the emerging of RES, understanding the Power Electronics interfaces used by RES to connect the grid becomes vital important. The converter is the key element of RES which makes the RES distinguished from a conventional generator in terms of the frequency stability and control. So a detailed and high-fidelity model of PE converter is modelled and the control strategy, especially the active power control, is discussed in this chapter.

Nowadays, most renewable energy generation is based on the VSC converter. From the system perspective, the behaviour of that generation largely depends on the characteristic of the VSC converter and its associated control strategy. Because of the scope of this research, the emphasis of this chapter is the frequency control-related behaviour of the grid side converter, which shares the same topology and control logic with the grid side terminal

of a VSC HVDC transmission line. Therefore, the principle and modelling of a VSC HVDC terminal are presented and can be applied to the VSC based RES.

3.2 The Principle of Power Electronics in Power System

As quoted in [7], "Power electronic circuits are used to control the power conversion from one or more AC or DC sources to one or more AC or DC loads, and sometimes with bidirectional capabilities."

In power systems with power electronics, the process of power conversion can be accomplished by the controller module and the power module, which can be depicted in Figure 3-1. The power processor is the converter in charge of the power transfer from the input terminal to output terminal, or vice versa. It is constituted of power semiconductor devices acting as switches, sometimes with support from passive devices like inductors and capacitors. By measuring the signal at input and output terminal, the controller is able to control and operate the switches according to algorithms with designed objectives, e.g. voltage or current setpoints.

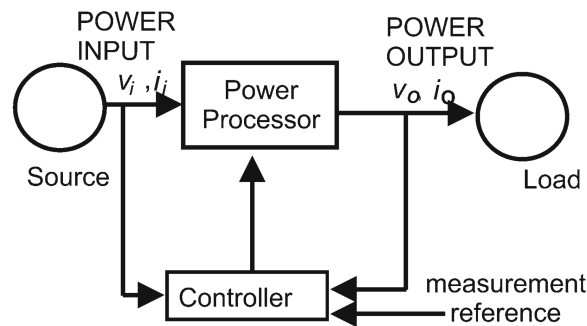


Figure 3-1: A general illustration of power electronics in power system, adapted from [7].

The modern power electronics era began in 1957 as first commercial thyristor was introduced to the market in that year and it rapidly replaced the mercury arc rectifiers, thyatron and ignitron invented decades ago [7].

Then more advanced power electronics switches were developed, including the bipolar junction transistor (BJT) with better turn-off capability compared to SCR. The BJT was used in applications from low to medium power. Invented in 1978, the Metal Oxide Semiconductor Field Effect Transistor (MOSFET) is used for low-power and high-frequency power electronic switching applications.

The gate turn-off thyristor (GTO), is used in applications from medium to high power and from low to medium frequencies. The insulated gate bipolar transistor (IGBT) is used in applications from low to medium power and frequency since 1987. The integrated gate commutated thyristor (IGCT) is invented in 1997 for medium to high power [7].

By using high switching technique, depending on the converter technologies used, PE converters can operate from a few watts to Gigawatts, with operating frequencies ranging from 100 Hz to 100 kHz [7]. PE can handle large amounts of power at a high power level cooperated with different types of equipment across the system.

Indeed, PE is now a key technology for the power system and has spread throughout the system in many applications: HVDC, reactive compensators and massive amount of interfaces for photovoltaic, wind, energy storage systems.

As the system develops, PE will continue to play an important role as an enabler for future power system applications, particularly new frequency control method. Additionally, new power devices and new PE technology will continue to be invented, providing higher capacities in term of power, frequency and lower losses.

3.3 Power Electronic Converter Topologies

The Voltage Source Converter (VSC) technology has been rapidly developed and widely used for HVDC transmission since the end of the 20th century. Unlike the line-commutated converters(LCC), which is widely used and well-proven, VSC is still a developing technology [47]. The VSCs typically use IGBTs in parallel with diodes, where IGBTs provide both controlled turn-on and turn-off capability which make a fixed DC voltage possible. Moreover, Both the magnitude and phase angle of the terminal AC voltage can be controlled independently at both ends.

Compared to an LCC HVDC link, VSC HVDC uses a fixed DC voltage with capability for the reversal of power flow. Most of the VSC application are offshore power transmission as we have introduced in the previous section. The drive of this system is due to insufficient strengths of the AC systems to support a stable LCC HVDC operation. LCC HVDC can only operate if the AC system strengths are strong enough since the thyristors rely on AC grid to turn off. In contrast, such limitation is not represented for a VSC HVDC link which makes it possible for the HVDC to work with weak systems and even offer black start capability [48].

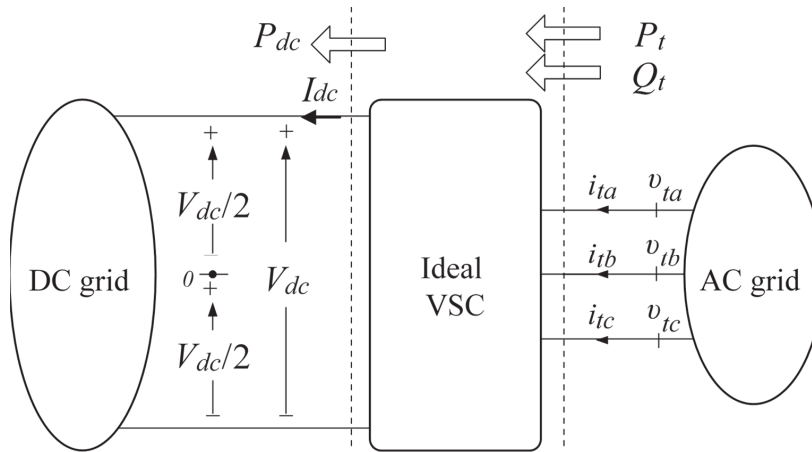


Figure 3-2: A ideal Voltage Source Converter.

3.3.1 Ideal Voltage Source Converter

Here the modelling of the VSC, including an ideal model and practical two level VSC model is presented. As shown in Figure 3-2, a VSC acts as an interface between a DC grid and an AC grid. In the diagram, the left side terminals of the VSC is referred to as DC side. DC voltage and current are V_{dc} and I_{dc} . The right side is referred to as the AC side and three phase voltages are v_{ta} , v_{tb} , and v_{tc} . Positive current direction is assumed from AC side to DC side. The following assumptions are made to the ideal VSC: The ideal VSC is passive and without any losses. Also, a fully controllable switch, diode, and transformer are all ideal.

The three-phase voltage can be expressed as

$$V_{ta} = V_t(t) \cos[\varepsilon(t)] \quad (3-1)$$

$$V_{tb} = V_t(t) \cos\left[\varepsilon(t) - \frac{2\pi}{3}\right] \quad (3-2)$$

$$V_{tc} = V_t(t) \cos\left[\varepsilon(t) - \frac{4\pi}{3}\right] \quad (3-3)$$

where $V_t(t)$ and $\varepsilon(t)$ are the magnitude and phase angle, respectively. $\varepsilon(t)$ is not directly used, but a function of the frequency, $\omega(t)$, as

$$\varepsilon(t) = \varepsilon_0 + \int_0^t \omega(\tau) d\tau \quad (3-4)$$

where ε_0 is the initial phase angle

If an AC grid is connected at the coupling point, to achieve a stable power flow the VSC need to synchronize with the AC grid, which means $\omega(t)$ is equal to the system frequency ω_s . A Phase Locking Loop is usually used to ensure it. Therefore, based on the above equations, the AC-side voltages are described as:

$$V_{ta} = V_t(t) \cos[\omega_s(t) + \varepsilon_0] \quad (3-5)$$

$$V_{ta} = V_t(t) \cos\left[\omega_s(t) + \varepsilon_0 - \frac{2\pi}{3}\right] \quad (3-6)$$

$$V_{ta} = V_t(t) \cos\left[\omega_s(t) + \varepsilon_0 - \frac{4\pi}{3}\right] \quad (3-7)$$

According to the assumption of the ideal converter, no power losses exists. The instantaneous power seen from the DC side, P_{dc} , is equal to the active power that AC system transfers, P_i :

$$V_{dc}I_{dc} = v_{ta}i_{ta} + v_{tb}i_{tb} + v_{tc}i_{tc} \quad (3-8)$$

which can be reordered as

$$I_{dc} = \frac{v_{ta}i_{ta} + v_{tb}i_{tb} + v_{tc}i_{tc}}{V_{dc}} \quad (3-9)$$

Based on the previous discussion, the principle of an ideal VSC operation can be described as that Magnitude V_t of a balanced three-phase AC voltage is proportional to the DC voltage V_{dc} . Therefore, to achieve stable operation, DC voltage V_{dc} is required to be as constant as possible. In another way to say, the DC grid should exhibit a small impedance to the VSC. On the other hand, since AC voltage is ideally independent to the AC currents, the AC grid needs to exhibit a large impedance to the converter. Overall, the VSC requires the DC grid acting like voltage source while the AC grid acting as a current source to achieve a stable operation.

3.3.2 Practical Voltage Source Converter

After the introduction of ideal VSC converter, this section will introduce the most typical circuit configurations of VSC converters. A simplified schematic diagram of the most widely used switched-mode circuits is shown in Figure 3-4.

The circuit, called two-level VSC, contains three half-bridge converters for three phases. Each half-bridge converter includes two IGBT switches as Figure 3-4 indicates. Accordingly, at every switching instant, the terminal voltage is switched from either of the two

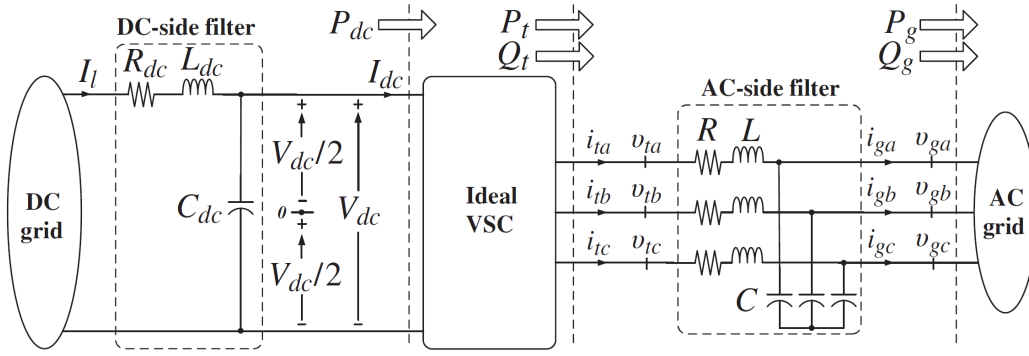


Figure 3-3: Ideal VSC equipped with DC-side and AC-side filters.

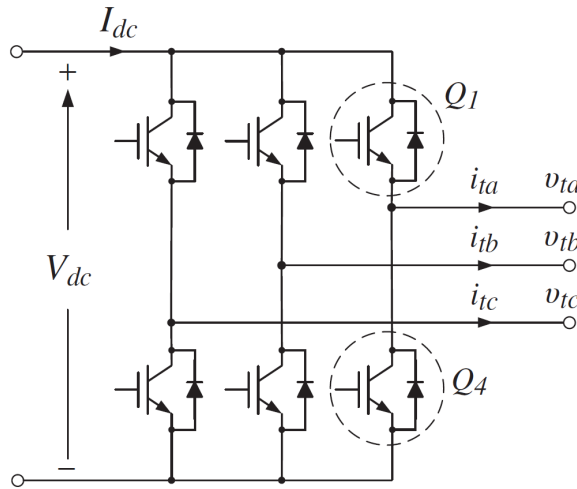


Figure 3-4: Simplified schematic diagram of the two-level VSC

available levels $-V_{dc}/2$ and $V_{dc}/2$. If the switching action is periodic, then the terminal voltage can be made to have the desired frequency ω , as

$$V_{ta} = V_i(t) \cos[\varepsilon(t)] \tag{3-10}$$

$$V_{ta} = V_i(t) \cos\left[\varepsilon(t) - \frac{2\pi}{3}\right] \tag{3-11}$$

$$V_{ta} = V_i(t) \cos\left[\varepsilon(t) - \frac{4\pi}{3}\right] \tag{3-12}$$

The AC voltage will have harmonic components because of switching actions, which are of odd orders if half-wave symmetry is used for the switching tech. The most widely used switching technique for two-level VSC is called carrier-based, pulse-width modulation (PWM) strategy. In Figure 3-5, it is shown that the switching instants is determined by a comparison of a modulating signal and a high-frequency triangular carrier signal.

Sinusoidal PWM (SPWM) is commonly preferred for VSC converter if PWM is used.

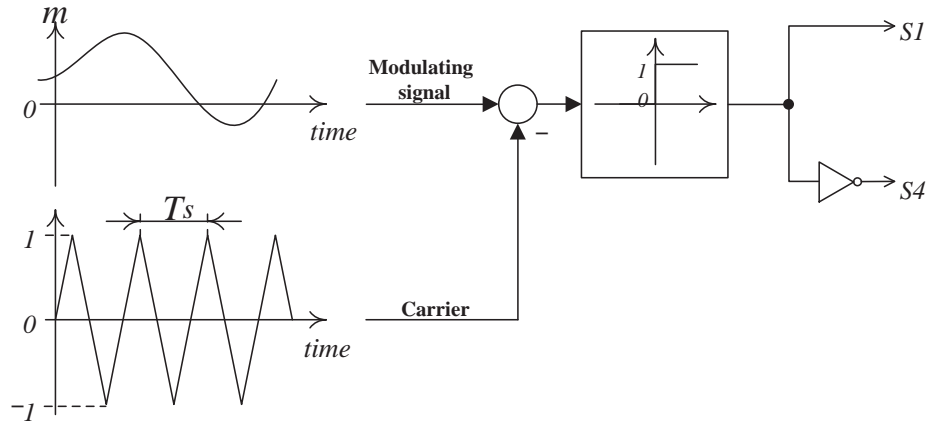


Figure 3-5: The pulse-width modulation (PWM) switching strategy.

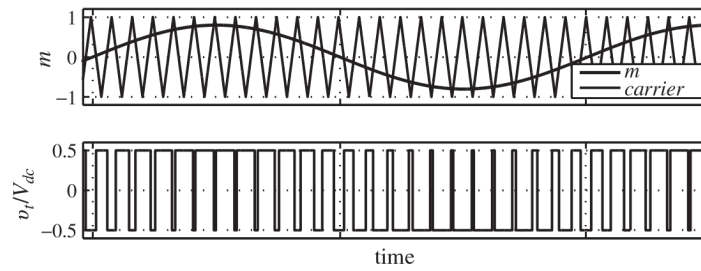


Figure 3-6: The modulating signal, carrier signal, and AC-side terminal voltage, based on the SPWM switching strategy [47].

Typical waveforms used by the SPWM method is shown below, each AC terminal voltage is proportional to the modulating signal and consequently the frequencies of harmonics are multiples of the frequency of the carrier signal which make itself easier to be mitigated by a smaller size filter.

The equations of the AC side voltages and modulating signals when using the SPWM strategy, are given as

$$V_{ta} = \frac{1}{2} V_{dc}(t) m_a(t) \quad (3-13)$$

$$V_{tb} = \frac{1}{2} V_{dc}(t) m_b(t) \quad (3-14)$$

$$V_{tc} = \frac{1}{2} V_{dc}(t) m_c(t) \quad (3-15)$$

Where $m_a(t)$, $m_b(t)$ and $m_c(t)$ are the modulating signals for three phases. By applying from (3-13) through (3-15), assuming that:

$M(t)$ is the magnitude of the modulating signals. Then the AC side voltages are,

$$V_{ta} = \frac{1}{2} V_{dc}(t) M(t) \cos[\epsilon(t)] \quad (3-16)$$

$$V_{tb} = \frac{1}{2} V_{dc}(t) M(t) \cos\left[\epsilon(t) - \frac{2\pi}{3}\right] \quad (3-17)$$

$$V_{tc} = \frac{1}{2} V_{dc}(t) M(t) \cos \left[\varepsilon(t) - \frac{4\pi}{3} \right] \quad (3-18)$$

If the modulating signal has constant magnitude and frequency. Then the AC side voltages are given as:

$$V_{ta} = \frac{1}{2} V_{dc} M \cos [\omega_s t + \varepsilon_0] \quad (3-19)$$

$$V_{tb} = \frac{1}{2} V_{dc} M \cos \left[\omega_s t + \varepsilon_0 - \frac{2\pi}{3} \right] \quad (3-20)$$

$$V_{tc} = \frac{1}{2} V_{dc} M \cos \left[\omega_s t + \varepsilon_0 - \frac{4\pi}{3} \right] \quad (3-21)$$

3.3.3 AC and DC Filters

In the real world, an AC filter needs to be inserted between the VSC terminal and the AC grid. Similarly, a DC capacitor is required to be installed at the DC terminal. There are reasons for these filters:

A practical VSC uses high-frequency switching techniques to generate AC voltage. Therefore, the AC terminal voltage is distorted by different orders of harmonics. If the AC grid is not strong, which means a small impedance, the harmonics voltage can result in large harmonics current, stressing the system and affecting the transmission efficiency. Therefore, impedance is inserted at the connecting point to suppress harmonics. In the same way, a large DC grid impedance may cause undesired DC voltage and disturb the operation of the VSC. To avoid this, a capacitor is installed at the DC terminal to support DC voltage by cancelling the DC impedance [47].

In the AC filter, the inductance, L , exhibits a large impedance to suppress harmonics, while the capacitance C acts as a short path to the ground so that high order harmonics are prevented from affecting the AC grid. The capacitance C can also support reactive power compensation to maintain the grid voltage at the coupling point. As the inductance L is connected in serial at each AC phase, it is also known as the tie reactor or phase reactor. Capacitor C is usually connected in parallel as LC parameter are tuned to certain cut off frequencies (usually the PWM switching frequency).

In the same way, the DC filter, capacitor C_{dc} , should provide a short path to the ground for DC harmonics. On the other hand, the capacitance also needs to be large enough to suppress double-frequency ripples which caused by unbalanced grid disturbances. So, in practice, the DC filter consists of both high-frequency and low-frequency capacitors.

3.4 Control of VSC HVDC converter

3.4.1 Overview

As AC side voltages are given, in this section, different controls strategy and modelling of the controllers are presented. Conclusions from this chapter are used to develop models in RTDS.

By controlling a three-phase VSC, we mean the way to control the real and reactive power. Real power may be directly controlled or to regulate the DC voltage of the VSC indirectly. In the same way, reactive power may be directly controlled or used to regulate the AC voltage. There are two kinds of control to achieve above goals: voltage control and current control [47] which will be discussed in the following part. In the voltage control mode, the terminal voltage magnitude and phase angle are directly controlled, relative to the grid voltage. If the phase reactor has a small $\frac{R}{L}$ ratio, then the AC-side terminal active and reactive power can be well controlled, proportional to the grid voltage magnitude and phase angle.

It is obvious that voltage control strategy is easier to implement. However, its shortcoming cannot be neglected. The VSC can be damaged due to AC grid disturbance like faults. For example, if a fault occurs in the AC grid and active, reactive power are suppressed, the VSC controller will try to increase the voltage magnitude and phase angle to maintain a setpoint of P_g and Q_g , resulting in a high current which can potentially damage the VSC and other equipment. Another issue is that voltage control strategy is more like a steady-state control as it uses phase angle and magnitude to achieve certain power flow. During the transient process, its performance can be entirely inadequate. Due to these issues, the current control mode is more preferred in practical implementation.

Using current control strategy, active and reactive power are regulated by the AC side current. Therefore, the VSC is protected against overcurrent issue since the terminal currents can be limited by properly designed control and constrained magnitude of the reference signal. This is the main reason for using the current control strategy.

Additionally, current control requires measurements of the grid voltage and current $i_{t,abc}$. On the other hand, the voltage control strategy only needs to measure the grid voltage. [49]–[51]

3.4.2 Design of Current Control for VSC

Space Phasors

The concept of space phasors can be very beneficial for analysing and controlling the AC side of VSC. Assuming f_a , f_b and f_c are three phase signals satisfying the relationship:

$$f_a + f_b + f_c \equiv 0 \quad (3-22)$$

the corresponding space phasor is shown as

$$\begin{aligned} \bar{F}(t) &= F_\alpha(t) + jF_\beta(t) \\ &= \frac{2}{3} \left[e^{j0} f_a(t) + e^{j\frac{2\pi}{3}} f_b(t) + e^{j\frac{4\pi}{3}} f_c(t) \right] \end{aligned} \quad (3-23)$$

where $F_\alpha(t)$ and $F_\beta(t)$ are the real and imaginary parts. To obtain real value signals, it can be written as

$$\begin{bmatrix} F_\alpha(t) \\ F_\beta(t) \end{bmatrix} = \frac{2}{3} C \begin{bmatrix} f_a(t) \\ f_b(t) \\ f_c(t) \end{bmatrix} \quad (3-24)$$

Where

$$C = \begin{bmatrix} 1 & -\frac{1}{2} & -\frac{1}{2} \\ 0 & \frac{\sqrt{3}}{2} & -\frac{\sqrt{3}}{2} \end{bmatrix} \quad (3-25)$$

Equally, the three signals can be retrieved if the space phasor is given. In terms of $F_\alpha(t)$ and $F_\beta(t)$, the constituting signals are given by

$$\begin{bmatrix} f_a(t) \\ f_b(t) \\ f_c(t) \end{bmatrix} = \begin{bmatrix} 1 & 0 \\ -\frac{1}{2} & \frac{\sqrt{3}}{2} \\ -\frac{1}{2} & -\frac{\sqrt{3}}{2} \end{bmatrix} \begin{bmatrix} F_\alpha(t) \\ F_\beta(t) \end{bmatrix} \quad (3-26)$$

Then if we apply above transformation to a balanced three-phase sinusoidal signal and amplitude and frequency of signal can be variable:

$$f_a(t) = F(t) \cos[\theta(t)] \quad (3-27)$$

$$f_b(t) = F(t) \cos\left[\theta(t) - \frac{2\pi}{3}\right] \quad (3-28)$$

$$f_c(t) = F(t) \cos\left[\theta(t) - \frac{4\pi}{3}\right] \quad (3-29)$$

where

$$\theta(t) = \theta_0 + \int_0^t \omega(\tau) d\tau \quad (3-30)$$

where $F(t)$, $\theta(t)$ and $\omega(t)$ are the magnitude, phase angle and frequency of the three-phase signal respectively. θ_0 is the initial phase angle. The space phasor of these signals is:

$$\bar{F}(t) = F(t) e^{-j\theta(t)} \quad (3-31)$$

Equation (3-31) can be represented graphically in the following complex plane

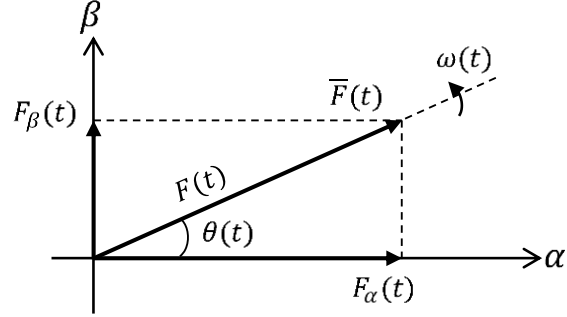


Figure 3-7: Space phasor in the stationary reference frame.

Using space phasors, we can derive the real power and reactive power equations. Consider the network shown in 3-2, the terminal voltages and currents are v_{abc} and i_{abc} . The instantaneous power flow can be described as

$$P(t) = v_a(t) i_a(t) + v_b(t) i_b(t) + v_c(t) i_c(t) \quad (3-32)$$

Equation (3-32) can be expressed using space phasors,

$$\begin{aligned} P(t) &= \text{Re} \{ \bar{V}(t) e^{j0} \} \text{Re} \{ \bar{I}(t) e^{j0} \} \\ &+ \text{Re} \{ \bar{V}(t) e^{-j\frac{2\pi}{3}} \} \text{Re} \{ \bar{I}(t) e^{-j\frac{2\pi}{3}} \} \\ &+ \text{Re} \{ \bar{V}(t) e^{-j\frac{4\pi}{3}} \} \text{Re} \{ \bar{I}(t) e^{-j\frac{4\pi}{3}} \} \end{aligned} \quad (3-33)$$

Using the identity $\text{Re} \{ \alpha \} \text{Re} \{ \beta \} = (\text{Re} \{ \alpha \beta \} + \text{Re} \{ \alpha \beta^* \}) / 2$ one can rewrite (3-33) as

$$\begin{aligned} P(t) &= \frac{\text{Re} \{ \bar{V}(t) \bar{I}(t) \} + \text{Re} \{ \bar{V}(t) \bar{I}^*(t) \}}{2} \\ &+ \frac{\text{Re} \{ \bar{V}(t) \bar{I}(t) e^{-j\frac{4\pi}{3}} \} + \text{Re} \{ \bar{V}(t) \bar{I}^* e^{-j\frac{4\pi}{3}} \}}{2} \\ &+ \frac{\text{Re} \{ \bar{V}(t) \bar{I}(t) e^{-j\frac{8\pi}{3}} \} + \text{Re} \{ \bar{V}(t) \bar{I}^* e^{-j\frac{8\pi}{3}} \}}{2} \end{aligned} \quad (3-34)$$

Since $e^{j0} + e^{-j\frac{4\pi}{3}} + e^{-j\frac{8\pi}{3}} = 0$, above equation can be simplified to

$$P(t) = \text{Re} \left\{ \frac{3}{2} \bar{V}(t) \bar{I}^*(t) \right\} \quad (3-35)$$

Reactive power can be also defined as

$$Q(t) = \text{Im} \left\{ \frac{3}{2} \bar{V}(t) \bar{I}^*(t) \right\} \quad (3-36)$$

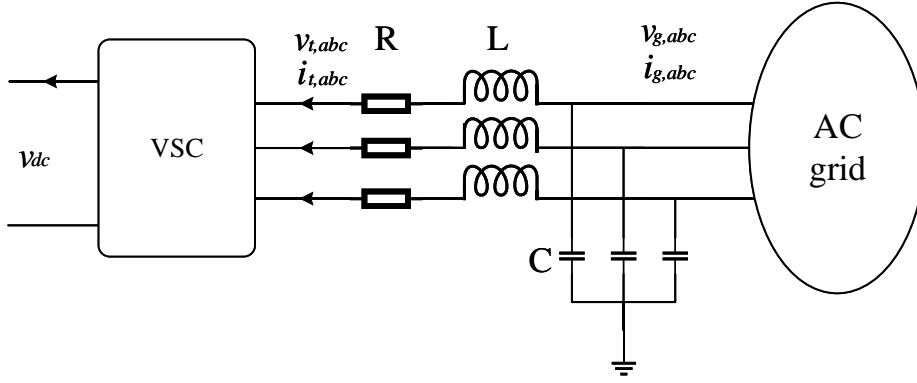


Figure 3-8: Practical VSC converter with filters.

3.4.3 Dynamic of the AC Side in Phasor Domain

Now consider the system contains filters where the AC side VSC follows dynamic equations:

$$L \frac{di_{ta}}{dt} = -Ri_{ta} - v_{ta} + v_{ga} \quad (3-37)$$

$$L \frac{di_{tb}}{dt} = -Ri_{tb} - v_{tb} + v_{gb} \quad (3-38)$$

$$L \frac{di_{tc}}{dt} = -Ri_{tc} - v_{tc} + v_{gc} \quad (3-39)$$

In the space phase,

$$L \frac{d\bar{I}_t}{dt} = -R\bar{I}_t - \bar{V}_t + \bar{V}_g \quad (3-40)$$

From (3-40) it is realised that the space phasor can be used for controlling VSC. For example, if the VSC is controlled to deliver zero real power but only reactive power, it is required to make its terminal voltage phasor aligned with voltage phasor of the grid, which means the grid voltage phasor and terminal current phasor are perpendicular to each other. This voltage phasor is achieved by generating proper current phasor by the current controller. Then the voltage phasor will be transformed into three phase voltages using the switching technique.

3.4.4 Current Control in $\alpha\beta$ Frame

Expressing (3-40) in the α -axis and β -axis components, one finds

$$L \frac{di_{t\alpha}}{dt} = -Ri_{t\alpha} - v_{t\alpha} + v_{g\alpha} \quad (3-41)$$

$$L \frac{di_{t\beta}}{dt} = -Ri_{t\beta} - v_{t\beta} + v_{g\beta} \quad (3-42)$$

It is desired to split the control of the VSC into two parts, and those two parts can be decoupled if the grid voltage components $v_{g\alpha}$ and $v_{g\beta}$ are independent. Then two control loops can be used independently to determine the desired terminal voltage. Then if we use $\bar{V}_g = V_g\alpha + jV_g\beta$ and $\bar{I}_g = I_g\alpha + jI_g\beta$,

$$P_g(t) = \frac{3}{2} (V_{g\alpha}I_{t\alpha} + V_{g\beta}I_{t\beta}) \quad (3-43)$$

$$Q_g(t) = \frac{3}{2} (-V_{g\alpha}I_{t\beta} + V_{g\beta}I_{t\alpha}) + Q_c(t) \quad (3-44)$$

where $Q_c(t)$ is the reactive power from filter capacitors as shown in Figure 3-8. In general, by knowing the grid voltage, P_g and Q_g can be controlled using decoupled AC current.

In the power system, the α - and β -axis components are sinusoids, a time-varying signal as equation (3-31) indicates. To minimise errors and to improve performance, the control scheme must be designed to have sufficient gain crossover frequencies, which implies a wide closed-loop bandwidth. So the controller design is typically very challenging [47]. It would make the control design much simpler if control uses DC signals instead of time-varying sinusoidal signals. It can be achieved by using the orthogonal rotating frame with a grid angular velocity. [52]

Current Control in a Rotating Frame

Assume a balanced three-phase grid voltage with variable-amplitude and variable-frequency as

$$v_{ga}(t) = V_g(t) \cos[\theta_g(t)] \quad (3-45)$$

$$v_{gb}(t) = V_g(t) \cos\left[\theta_g(t) - \frac{2\pi}{3}\right] \quad (3-46)$$

$$v_{gc}(t) = V_g(t) \cos\left[\theta_g(t) - \frac{4\pi}{3}\right] \quad (3-47)$$

Where

$$\theta_g(t) = \theta_{g0} + \int_0^t \omega_g(\tau) d\tau \quad (3-48)$$

It can be transformed into space phasor,

$$\bar{V}_g(t) = V_g e^{j\theta_g(t)} \quad (3-49)$$

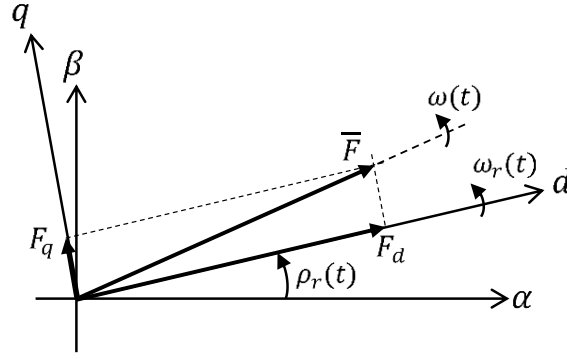


Figure 3-9: Space phasor with the rotating frame.

It can be seen as a phasor rotating with angular velocity ω_g , as shown in Figure 3-9. If we assume a new frame, dq frame, whose d -axis rotates at speed of

$$\omega_g(t) = \frac{d\rho}{dt} \quad (3-50)$$

If the dq -frame rotates at the same speed of V_g , the d - and q -axis components V_{gd} and V_{gq} become time invariant. Then we can obtain the transformation from $\alpha\beta$ to dq -frame,

$$\begin{bmatrix} F_d \\ F_q \end{bmatrix} = \begin{bmatrix} \cos \rho(t) & \sin \rho(t) \\ -\sin \rho(t) & \cos \rho(t) \end{bmatrix} \begin{bmatrix} F_\alpha \\ F_\beta \end{bmatrix} \quad (3-51)$$

The system of Figure 3-8 can now be rewritten in dq -frame, giving new equations as

$$L \frac{di_{td}}{dt} = -Ri_{td} + L\omega I_{tq} - v_{td} + v_{gd} \quad (3-52)$$

$$L \frac{di_{tq}}{dt} = -Ri_{tq} - L\omega I_{td} - v_{tq} + v_{gq} \quad (3-53)$$

Then for the power flow,

$$P_g(t) = \frac{3}{2} (V_{gd}I_{td} + V_{gq}I_{tq}) \quad (3-54)$$

$$Q_g(t) = \frac{3}{2} (-V_{gd}I_{tq} + V_{gq}I_{td}) + Q_c(t) \quad (3-55)$$

If the grid voltage components V_{gd} and V_{gq} are known, P_g and Q_g can be controlled by AC side current I_{td} and I_{tq} .

Based on SPWM, V_{td} and V_{tq} are proportional to dq components of the modulating signal m_d and m_q . In practice, harmonic distortion or unbalanced terminal voltage can add time-varying components to the ideal DC signal. These components will be passed to the

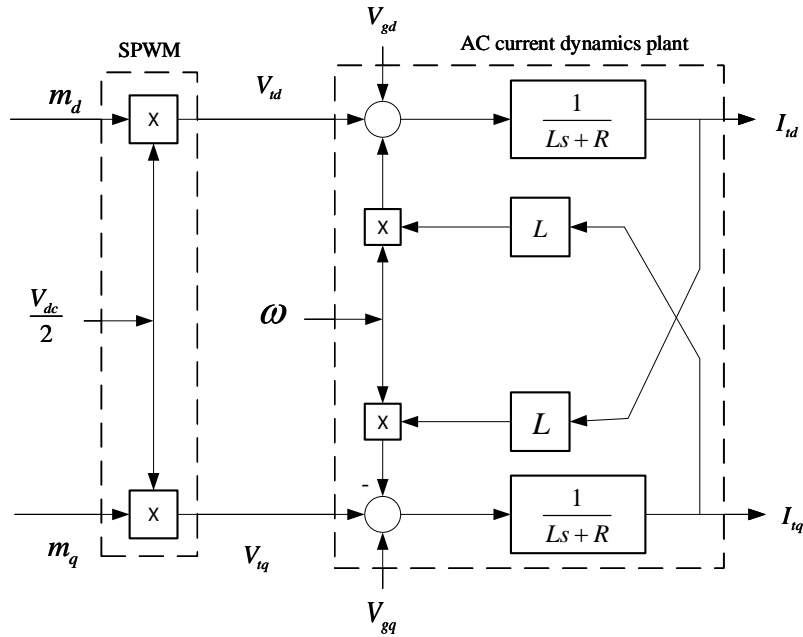


Figure 3-10: The dynamics of the AC side current in dq frame.

converter and produce harmonic distortion at the AC side. Hence, to minimize the harmonic distortion of $V_{t,abc}$, the harmonic order needs to be increased by the SPWM strategy or using multi-level converter techniques [53], [54].

For the above control system, the objective is to regulate I_{td} and I_{tq} at their setpoints I_{td}^* and I_{tq}^* . However, the control is not straightforward because I_{td} and I_{tq} are coupled by the components $\omega L I_{td}$ and $\omega L I_{tq}$. Moreover, the grid voltage $V_{g,abc}$ is also related to the current of the VSC, $I_{t,abc}$ and the AC grid impedance.

Figure 3-11 shows a control scheme which can overcome those issues we discussed above with the system in Figure 3-8. Therefore, it is possible to say that two independent control loop can be used for controlling VSC which can be called as dq controllers. If we use d axis control loop as an example, a compensator $K_i(s)$ is used for the error signal e_d and providing signal u_d . Then, the d-axis AC terminal voltage reference V_{td}^* is determined by considering the other two signals, $\omega L I_{td}$ which decouples I_{td} from I_{tq} and grid voltage. Similarly, the q -axis controller decouples I_{tq} from I_{td} . Lastly, the modulating signal, m_d and m_q , are calculated by dividing gain $V_{dc}/2$. It is noted that the feedback and feedforward signals in Figure 3-11 are measures of the actual variables in the system. However, we use the same symbol for both a variable and its measure because we assume that the measurement is fast enough so that we can neglect the dynamics. In the other way, we assume the voltage and current measurement devices offer responses with sufficient bandwidth so that they are

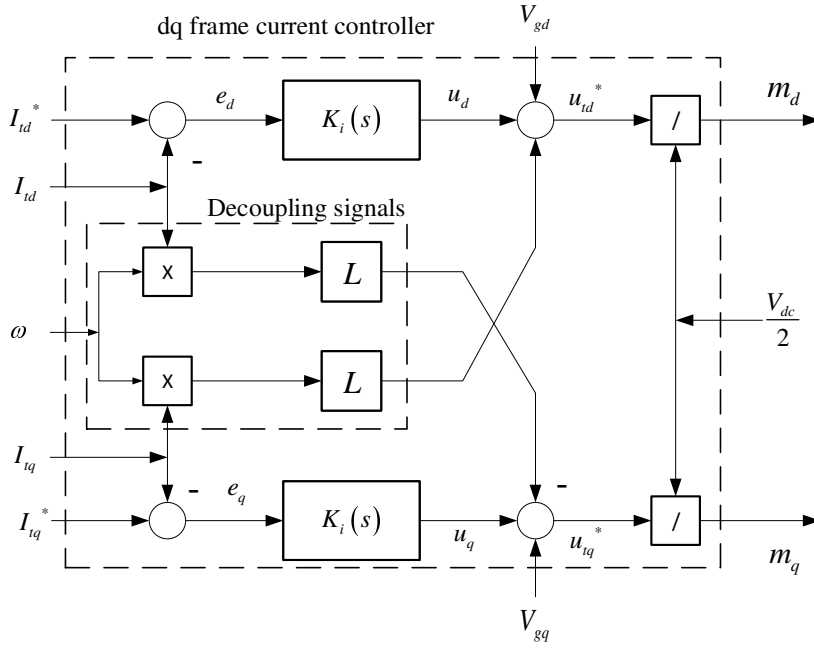


Figure 3-11: A block diagram of the current controller for the system.

likely equal.

The whole current control process is illustrated in Figure 3-12, including the control scheme in Figure 3-11 and control plant in Figure 3-10. The control is combined with two decoupled and independent control loops. One loop regulates I_{td} using reference I_{td}^* , and the other loop regulates I_{tq} by reference I_{tq}^* . It is worth noting that both control loops have identical transfer function, therefore same compensator $K_i(s)$ is used.

For implication, d axis is used for the following discussion. The conclusion also applies to q axis. The control plant shown in Figure 3-13 has a first-order transfer function, the simplest way to ensure zero error at steady state is to use a PI controller [55].

$$K_i(s) = \frac{k_p s + k_i}{s} \quad (3-56)$$

where k_p is proportional gain and k_i is the integral gain. If we set parameters as

$$k_p = \frac{L}{\tau_i} \quad (3-57)$$

$$k_i = \frac{R}{\tau_i} \quad (3-58)$$

Therefore, the closed-loop transfer function has the following first-order forms

$$\frac{I_{td}(s)}{I_{td}^*(s)} = \frac{1}{\tau_i s + 1} \quad (3-59)$$

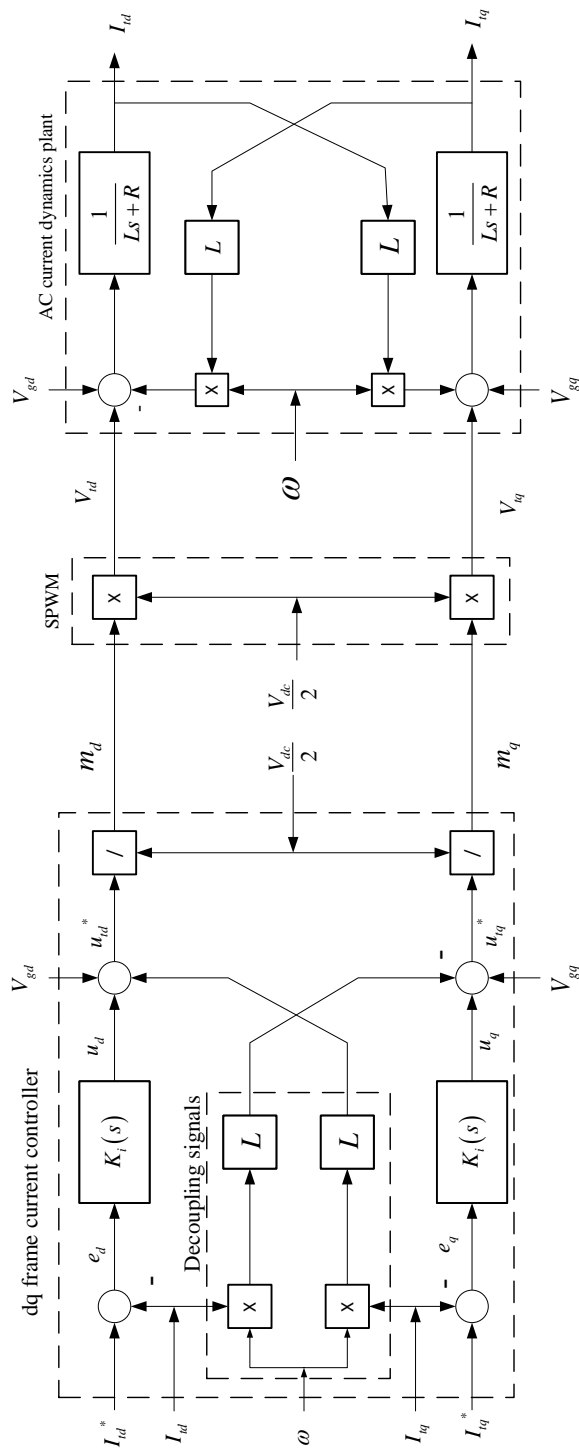


Figure 3-12: The Whole block diagram including current controller and control plant in dq-frame.

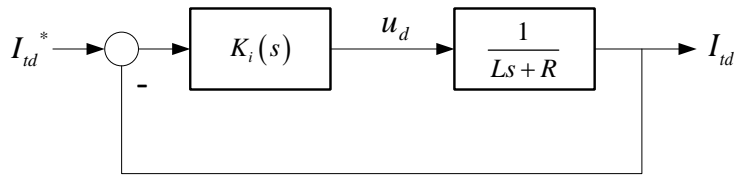


Figure 3-13: The decoupled control loop for d -axis.

where τ_i is the desired time-constant of the closed-loop response. The choice of parameters based on (3-57) and (3-58) can cancel the plant pole, $-R/L$, reducing system order to a first-order closed-loop transfer function (3-59). As the first-order closed-loop transfer function can be designed to show no overshoots, for the VSC protection, as long as reference signal I_{td}^* and I_{tq}^* are properly limited, overloading can be avoided easily. In the other hand, because R is a parameter sensitive to temperature and therefore varying constantly, the pole cancellation cannot be perfect.

3.4.5 Active and Reactive Power Control of VSC

With the complete design of inner current control loop, the active and reactive power controllers can, therefore, be readily designed by providing I_d^* and I_q^* set values to specify the injected active and reactive powers by the VSC in steady-state condition as shown in Figure 3-14 and 3-15.

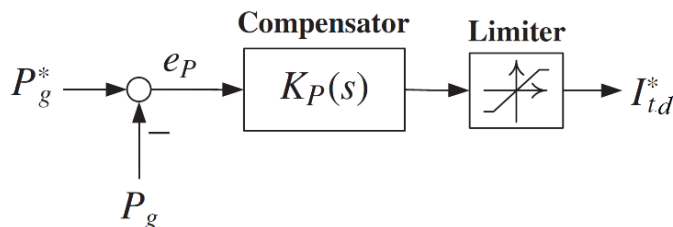


Figure 3-14: A block diagram of active power regulator.

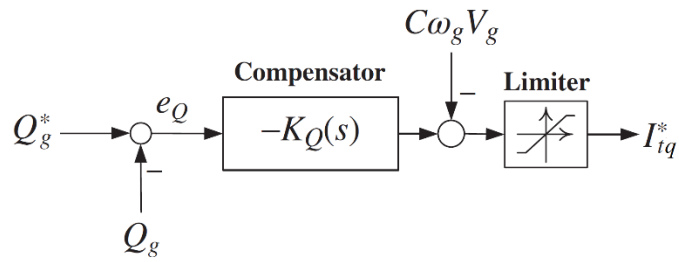


Figure 3-15: A block diagram of reactive power regulator.

3.5 Simulation of Power Response of a VSC Converter on RTDS

As discussed in previous sections, the nature of the control strategy of the VSC converter is not coupled with system frequency. To investigate the performance of modelled converter for frequency control, the DC side of the converter is connected with a constant DC source and its AC side is connected to a simplified power source. In Figure 3-16, a step change of system frequency is initiated at 0.4 s. The output in terms of active power and reactive power is recorded, as shown in the figure. It can be noticed that despite an initial transient within a few hundred milliseconds of the step change, both active power and reactive power bound to their set points. This has validated that the control strategy of outer loop controller which is designed to not responsive to system frequency changes.

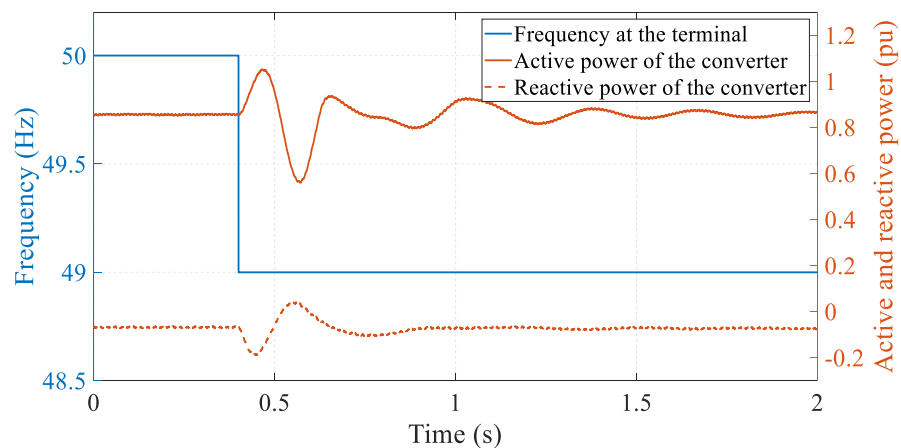


Figure 3-16: Frequency step responses of the converter plant.

Additionally, Figure 3-17 shows the step responses of active power and reactive power controls of a VSC converter. In the left figure, a step change of voltage set point is initiated at 0.125 second and the AC voltage reached the set point within 300 milliseconds. In the

other figure, the active power set point is change from 0 to 0.5 pu at 0.125 second. The active power output reached the set point within 200 milliseconds. It should be noted that the difference of the response time is because the terminal voltage is subject to both reactive power output of the converter and external grid characteristic. Figure 3-17 demonstrates

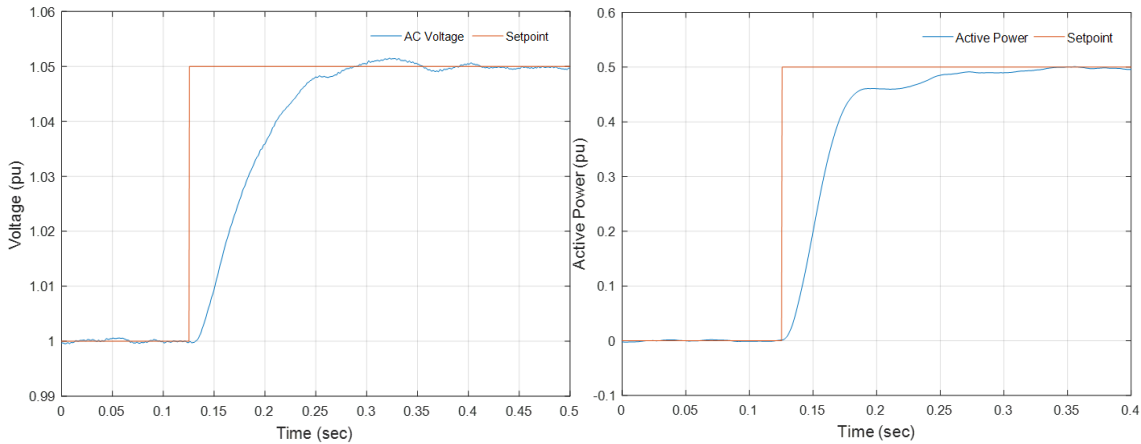


Figure 3-17: Step responses of the AC voltage regulator and active power regulator.

the step response of the AC voltage regulator and active power regulator. The response time of the VSC converter is less than 100 ms for achieving 80% of the setpoint. The DC side of the converter is connected to an external grid through HVDC link to be able to deliver such requested active power. It is evident that such fast response time could be utilised to support the frequency control in the power system.

3.6 Chapter Summary

This chapter has introduced the principle of the VSC converter used by the majority of the RES. The concept of the current control strategy provides the converter with a reliable method to control the active and reactive power at the AC and DC side of the converter independently. The presented converter is modelled in RTDS as an HVDC transmission system. The results of the active and reactive power response of the modelled converters have proved the potential capability of frequency control by PE interfaced RES.

Chapter 4

Analysis of Frequency Control in Low-Inertia System

This chapter describes the development of the system and how inertia evolves as the development. The impacts of the change of system inertia on the frequency control and containment are discussed. Section 4.1 discusses the importance of analysing frequency response before attempting to improve it. The definition of inertia, as well as the trend of inertia changes, are discussed in Section 4.3, while Section 4.5 describes the fast active power injection and the issues with RoCoF. Finally, Section 4.6 simulation results are presented to demonstrate the challenge of lower system inertia and frequency control. Section 4.7 provides a summary of the chapter.

4.1 Chapter Introduction

In this chapter, we focus on the primary control, which starts to act within 10 seconds after a frequency disturbance and to take effect over the following minute. Besides the primary control, between 60 seconds to 10 minutes, secondary control is activated to provide the ability for the system frequency to return to steady-state.

4.2 Definition of Inertia in Power System

For a single rotating machine, the inertia is a measure of the rotational energy, E , stored in a rotating mass and is defined as follows

$$E = \frac{1}{2} J \omega_m^2 \quad [\text{MVAs}] \quad (4-1)$$

Where J is the moment of inertia of the rotating mass (kgm^2) and ω_m is the rotational speed of the rotating mass (rad/s). Moment of inertia is namely the rotational inertia, and it appears in the relationships for the dynamics of rotational motion.

For a point mass the moment of inertia equals the mass times the square of the perpendicular distance to the rotation axis, $J = mr^2$. This point mass becomes the basis for all other moments of inertia as any object can be built from a point mass cumulatively. The moment of inertia is a quantity that determines the torque needed for a desired angular acceleration about a rotational axis.

When calculating the inertia of a machine that consists of multiple rotating masses that are connected it is necessary to consider the moment of inertia for all the connected masses to calculate the total inertia accurately.

By this definition, it can be seen that the rotational energy varies with the rotational speed. It is more convenient to convert this variable definition of energy into inertia constant, or H constant [56], as defined in (4-2). This definition is based on the assumption that the speed of the machines connected to a power system will usually be approximately equal to the synchronous speed of that system ω_{sm} . Furthermore, this definition of H is normalised using a power base, S_b . This normalisation of H means that it now defines the time for which the energy stored within the rotating mass could supply the power equal to S_b .

$$H = \frac{1}{2} \frac{J \omega_m^2}{S_b} \quad [\text{s}] \quad (4-2)$$

The H constant of a machine is usually normalised using the rating of the machine. Therefore, before the H constants of different machines can be combined into an equivalent H constant for the system, a base transformation must be applied so that they all appear on the new system base.

The most common examples of rotating masses in a power system are the prime movers and shafts of generators and motors; these are collectively referred to as machines in the remainder of this chapter. Therefore, the H constant of a power system can be defined as

the sum of the H constants of the M motors and N generators that are directly connected, i.e. not connected over PE converters or an HVDC link, to the system. When the necessary base conversion to the power system base, $S_{b,sys}$, is included, the system inertia constant, H_{sys} , can be calculated using 4-3.

$$H_{sys} = \sum_{i=1}^N \frac{1}{2} \frac{J_i \omega_{sm,i}^2}{S_{b,sys}} S_{b,i} + \sum_{j=1}^M \frac{1}{2} \frac{J_j \omega_{sm,j}^2}{S_{b,sys}} S_{b,j} \quad [s] \quad (4-3)$$

The term ‘system inertia’ is used as a convenient way to describe the quantity of kinetic energy stored in the rotating parts of the machines. The system inertia is expressed in GVA.s, equals to the system inertia constant multiplying total system capacity. By this definition, the system inertia is a convenient way to assess the system’s capability of regulating a sudden frequency disturbance. It should be noted that the energy expressed by system inertia cannot be fully utilised for frequency regulation as the system frequency is restricted within a certain range as discussed in chapter 2. Therefore, approximately 2% of the total inertia can be transferred to the system before frequency breaches the statutory limit [57].

4.3 Transition to Low-Inertia Systems

As discussed in the Section 1.2.2 and 1.2.3, the penetration level of non-synchronous generation has been increasingly deployed in the modern power system. The reduced inertia starts to become the major challenge for the existing frequency control methods. For example, according to the report from National Grid [57], currently system operator does not allow the system inertia going below 130 GVA.s after an active power disturbance assuming no emergency tripping of inflexible generators. This is due to the restriction on post-event rate of change of frequency imposed by RoCoF based loss of mains protection relays commonly used by Distributed Generation. It is also noted that when an disturbance is caused due to disconnection of machines, the inertia loss of those machines can be as much as 8 GVA.s which takes a considerable portion of the total system inertia (6.15 per cent of a 130 GVA.s system) and should be considered when designing frequency control methods.

When the system demand is not high, attempts to maintain inertia would require instructions to conventional generators to remain online and running, even if they are out of economic merit [57]. New frequency response solutions need to be developed if the system operator would like to allow the drop in inertia and to tolerate more significant generation

or demand lost risk.

4.3.1 Inertia and Frequency response

When generators and other rotating machines in the system increase speed, energy is transferred from the grid into kinetic energy of the rotating mass. As shown by (4-1), a machine with higher rotational inertia means more energy stored which can therefore contribute more power and energy to the active power disturbance.

In the case of a loss of generation, the energy is transferred from the kinetic energy stored in the rotating mass of generators to the power system. The synchronous machines slow down and consequently electrical frequency of the power system declines.

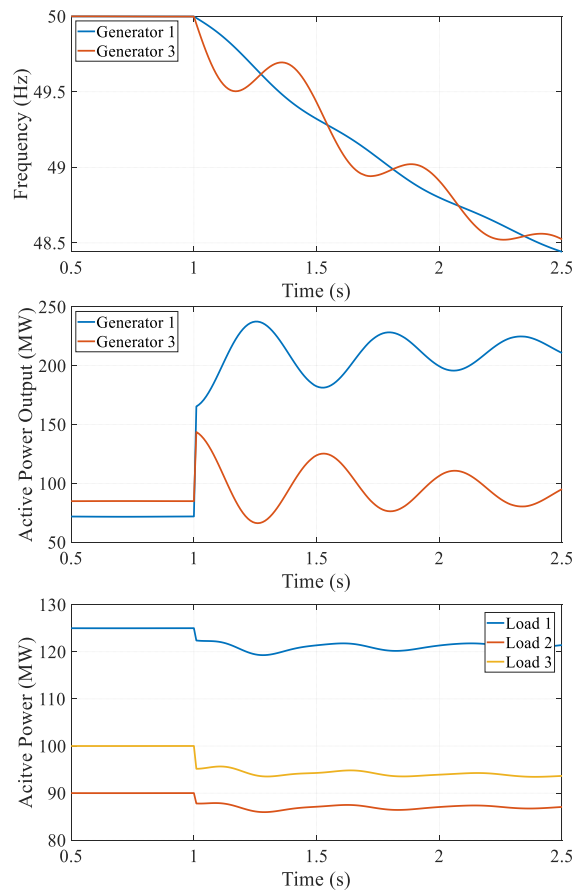


Figure 4-1: Inertia response for loss of 163 MW generation in IEEE 9-bus system.

Figure 4-1 shows an illustrative case of the inertia and frequency response to a typical generator tripping event in the IEEE 9-bus power system. The frequency response in the first 1.5 seconds after Generator 2 (163 MW) disconnected at 1s is shown. The detailed information of the IEEE 9-bus test system is given in the Appendix. After the disconnection of the

generator, the imbalance of active power is 163 MW in deficit. The synchronous machines in the system start to slow down as the kinetic energy being transferred to the power system with an immediate additional electrical demand at 153 MW. The rest 10 MW is compensated by the loads as a result of voltage depression caused by the loss of reactive power from the disconnected generator. The sum of the power from the remaining generators and the reduction in demand is always equal to the initial active power deficit. It is also noted that the setpoints of remaining generators are also increased as the governor of the generators has detected the deviation of frequency and raised the setpoint accordingly. However, due to the nature of the governor explained in the section 2.3, the response speed of the governor is considerably slower.

For a GB system with 200 GVA.s inertia, this level of inertia equates to approximately 4 seconds for a typical imbalance of 1 GW to violate 49.5 Hz statutory limit, which is rather a short period of time compared to the time frame of primary frequency control. Following the explanation of the traditional frequency control methods, if the system inertia continues to reduce, the ability of the system to regulate frequency will be further stressed as the conventional frequency methods will be challenged both in terms of capacity and response time.

4.3.2 Inertia Trends and Directions

As mentioned in the Section 1.2.2, the penetration level of PE interfaced non-synchronous generation is increasing. In Europe, the ENTSOE has published a report [4], pointing out that the system inertia time constant H will reduce from 5-7 seconds at different areas to a level of 0-2 seconds in the future. In the UK, National Grid has also produced a series of predictions of the future inertia in the system [57]. Figure 4-2 shows how the system inertia could evolve across the decades with different loading conditions. The peak of the inertia of the GB system is currently above 250 GVA.s in a heavy loading scenario and the minimum is just under 200 GVA.s.

However, in the next decade, it can be seen that the system is running down to a much lower level of inertia with a minimum number of conventional units. This inertia level will constantly stay below 100 GVA.s even at highest demand.

One way [57] to maintain minimum acceptable inertia is that part-loaded conventional generators could be kept running for this purpose, instead of replaced by non-synchronous

resources. However, this solution will inevitably result in excessive cost as those generators are not operating at the economic setpoint. On the other hand, as the number of conventional synchronous units reduces, the variation of the system inertia becomes more severe as the total amount of inertia is smaller than before.

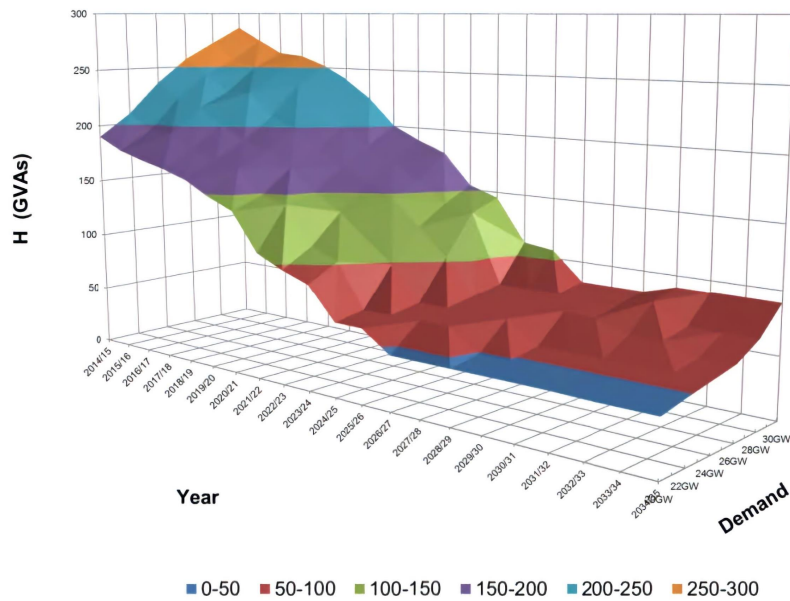


Figure 4-2: System inertia forecast in the GB system [57].

4.3.3 The Rate of Change of Frequency

Another challenge caused by falling system inertia is the increased the likelihood that distributed generation could unwittingly be disconnected due to loss of main protection based on the Rate of Change of Frequency (RoCoF). In GB system, there are over 6 GW DGs might be associated with this risk [57]. This is because of the RoCoF relay which will disconnect the DGs when the distribution network is isolated by fault clearing or loss of main event to protect the DG and the system.

RoCoF based islanding detection uses relatively high inertia to determine the original RoCoF settings of the loss of mains protection devices. As the system inertia drops, higher RoCoF levels resulting from frequency disturbances could exceed the threshold of RoCoF relay of DGs which would result in unnecessary disconnection of DGs. A significant loss of generation in the system could immediately trigger a widespread disconnection of distributed generation, resulting in a much-enlarged imbalance across the system.

Since RoCoF is a function of imbalance and system inertia, as shown in the equation (4-4) and in Figure 4-3, the RoCoF can be limited by either increasing the system inertia or reducing the size of the largest possible active power disturbance.

$$2H \frac{df}{dt} = P_m - P_e = \Delta P \text{ [p.u.]} \quad (4-4)$$

To increase inertia by keeping more synchronising generating units in the system is con-

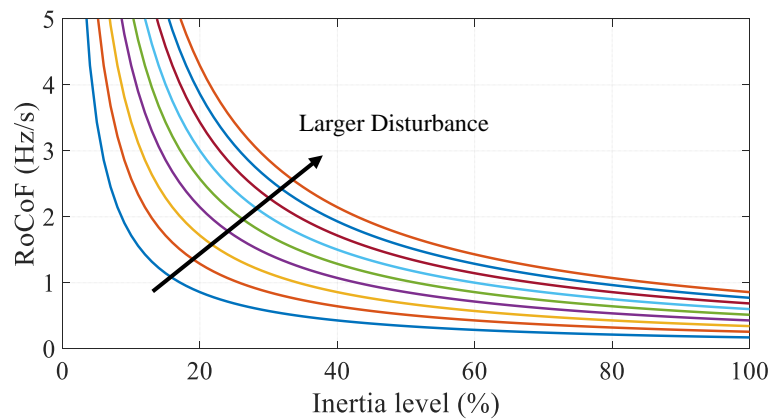


Figure 4-3: Instantaneous absolute RoCoF, a relationship between absolute loss size and inertia.

siderably more expensive than to reduce the size of the largest possible loss of generation. It is sensible for the system operator to reduce the size of the largest potential loss of generation or demand first to limit the RoCoF until it becomes economical incentive to spin more units to increase system inertia. This typically involves re-dispatching the power flow of interconnectors and large generators. Pumped storage units can also act as synchronous compensators by spinning in the air, which has both effect of increasing inertia and frequency response.

In the UK [57], these actions are taken to minimise the risk of a RoCoF of 0.125Hz/s because the system inertia is still maintained at a high level. There are ongoing programmes and working groups to replace or update the relevant protection systems, including RoCoF protection in the UK and Europe [57], [58].

4.4 Frequency Containment with Reduced System Inertia

4.4.1 Enhanced Frequency Control

As discussed in the previous sections, the penetration of renewable energy grows, the reduced inertia and the imposed higher RoCoF during the under-frequency event may increase the risk causing failure and maloperation of existing frequency control methods. There is a need for new ancillary services to support frequency control to maintain a power system's frequency stability.

The two key consequences of lower system inertia are faster frequency declining and shortage of power reserve in the initial stages before traditional services could start. Therefore, the new enhanced frequency response should be a fast service with a short duration. Figure 4-4 shows the concept of new and traditional frequency services, and the red zone presents the new frequency service. However, it became apparent that such a service would not be compatible with the existing services because there was not a facility to manage the transition between one service and another. The 'Enhanced Frequency Control Capability' Network Innovation Project [59] has researched an improved Monitoring and Control Scheme (MCS) for this purpose, and the design and validation of the proposed EFCC scheme are presented in Chapter 8.

So it is preferable to extend response delivery from ten seconds to a longer period, i.e. 15 minutes, as shown in the Figure, due to the challenge of handover between different types of frequency response. This extended time period will allow enough time for system operator to instruct further command and to avoid interactions between different types of response services.

4.4.2 Fast Frequency Response

As discussed in chapter 3, even though the PE-interfaced generation can not naturally respond to a frequency event like the traditional inertia response and the frequency control, it is possible for those PE-interfaced devices to actively compensate active power imbalance within a short time after the disturbance [20]. This is usually referred to as Fast Active Power Response or Fast Frequency Response (FFR). This becomes possible due to the capability of the commonly used VSC interface which provides fast control response within a

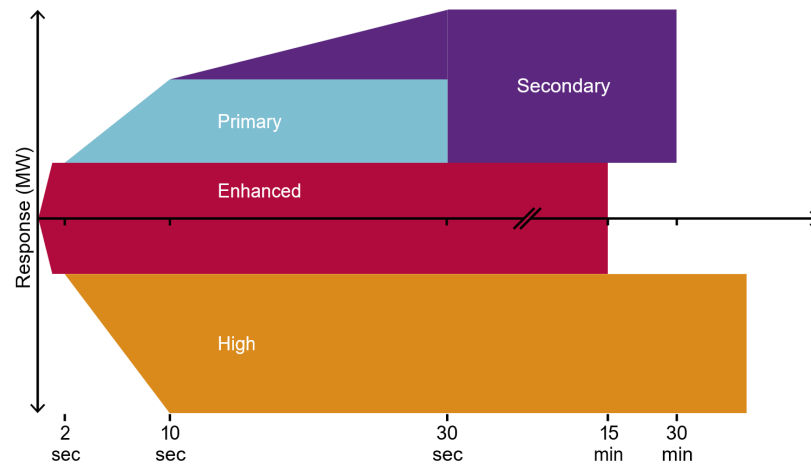


Figure 4-4: Concept for enhanced response service [57].

few hundred milliseconds.

FFR has been widely discussed and developed in the recent years. In [60], [61], the use of VSC-HVDC systems to provide fast frequency support is studied, where control methods have been developed to make use of rotating kinetic energy of the wind turbines and energy stored in DC links for fast frequency support. In [62], [63], demand side response used for providing FFR is reported. The authors in [62] developed a decentralized control scheme that allows the aggregation of refrigerators to provide FFR. In [63] the work takes advantage of collective contributions of different types of smart loads to provide FFR. In [64], control methods are proposed to enable DFIG-based wind turbines to provide fast active power support during frequency disturbances. In [65], new control strategies that allow PV farms for frequency regulation are investigated.

These researches and studies have demonstrated the importance of FFR in future power systems and the feasibility for FFR to be achieved using a range of technologies. However, only a specific technology or type of energy source is used without the consideration of the optimised coordination of a variety of resources available in the system, which usually have distinctive characteristics and capabilities in terms of their active power support. Furthermore, The regional factor has not been properly addressed in those studies. In [65], the regional impact of frequency events was considered, only PV is considered in this study and the coordination with other frequency service providers is not included.

In addition, the research reported in [66], [67] focuses on the optimal scheduling of resources for providing FFR. In [66], the authors present a method for allocating the commitment of energy storage to provide frequency support. In [67], the authors use a stochastic

approach to schedule FFR based on the system inertia level. However, these studies did not consider the coordination of a range of different resources and the focus is mainly on the strategy for dispatching FFRs without detailed consideration of power system's dynamic behaviours. In [68], the authors attempted to dispatch PE-interfaced resources assisted by communications to achieve FFR. However, the characteristics of resource (e.g., initiation time and ramping rate of active power response) are not considered. Therefore, the dispatched resources are not fully optimised to collectively provide fast and long-duration response.

It can be seen from the literature review that, while the need for FFR in systems with low inertia has been widely recognised, the following issues still remain unresolved:

- The locational impact of FFR has not been fully considered, rotor angle stability and the risks of accelerating frequency control using local measurements has not been recognised;
- The coordination of responses from different resources has not been fully investigated when deploying the FFR from different resources with different characteristics and capability. The overall response has not been optimised;
- The need for consider the changing behaviour of resources when the resource could have different capability depending on the dispatch and wind/solar availability. This could potentially lead to a mismatch between the expected response and the actual power delivered by renewable generation. Therefore, there is risk of over/under delivering frequency support.

Nevertheless, for such a fast active power response, it usually requires the real time measurements of frequency, RoCoF and other key variables in the power system. Therefore, time delay caused by the communication system needs to be introduced to the overall response time of the fast active power response, which needs to be addressed in any design of such control schemes.

As system inertia is running into lower levels, there is great interest in new approaches to address the challenge of low inertia in the system. The following section will explore the behaviours of system with low inertia and the potential benefit of fast active power response.

So far a practical solution for fast frequency response is yet to be demonstrated. Following a frequency disturbance, the inertia can immediately respond to the change of frequency while it would require at least a few hundred milliseconds time delay for the fast frequency

response to start to act. While measurement and processing time could be reduced, it is also vital to consider both the security and dependency of the solution to ensure not to be triggered by undesired transient signals. While the development of fast sources of active power is attracting great interest both in research and industry, fast active power response cannot directly replace the principle of system inertia [57].

4.5 Frequency Response of Low-Inertia Systems

In this section, the IEEE 39-bus test system is modified to have three scenarios of inertia level, which is 100 %, 75 % and 50 % of the original inertia value. The original data of the test system can be found in the Appendix. All the frequency responses presented in this section are based on the following event: A generator of 500 MW is tripped at 1 s at bus 18. This event implies a loss of about 7.94 % of the total generation. For this event, a study on how different system scenarios and the characteristic of the fast frequency control affect the frequency response of the system is presented.

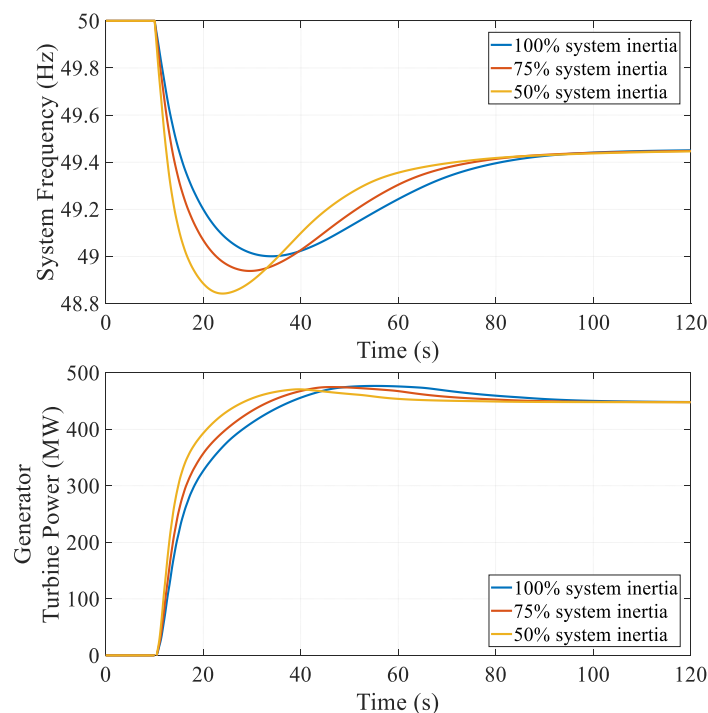


Figure 4-5: Simulation of a 500 MW loss of generation in IEEE 39-bus system.

Figure 4-5 shows the different frequency response with system inertia level at 100 %, 75 % and 50 % of the original inertia value. As recorded in Table 4-1, the overall response

requirement remains the same for simulation with three scenarios. However, if we focus on the first ten seconds which lies in the primary control section, the latter of which results show a greater requirement of the amount from primary response. In contrast, with low inertia level, the primary response is inevitably smaller than the current status due to the reduced unit number and higher operating points of those conventional units.

Table 4-1: Frequency response requirements for the example.

System inertia (%)	Generation loss (500 MW)	
	Overall requirement	Requirement within 10s
	Response requirement (MW)	
100	485	325
75	485	350
50	485	400

Then a Fast Frequency Response (FFR) source is modelled in the test system, and the results of frequency are presented below. The characteristic of the modelled resource is configured to act as immediate load disconnection and sources ramping within 1, 2 and 3 seconds respectively. The 50% inertia scenario is used as it mostly reflect the future low-inertia condition. Figure 4-6 shows how the loss of generation disturbances can be contained with and without additional enhanced frequency response besides the conventional primary frequency control. The available response from the resource is 300 MW with variety ramping time. It is assumed the fast frequency response can be quickly triggered within 1 s after the disturbance.

It is evident that the faster the source responses, the better the frequency response the system will experience in terms of the frequency nadir and recovery time. Additionally, due to the contribution of the additional active power, the requirement from the reserve of conventional units are much reduced by 300 MW, equal to the amount of enhanced active power injection from the resource.

In Figure 4-7, the amount of enhanced frequency control is assessed compared to the base case. The active power contributed by the fast frequency control are 300, 200 and 100 MW respectively. The size of tripped generator remains unchanged, which is 500 MW. Compared to Figure 4-8, the impact of the amount of fast frequency control to the frequency is more significant. The nadir of frequency is improved from 48.82 Hz in case of no fast frequency control to 49.21, 49.5 and 49.69 Hz in three cases with active power injection.

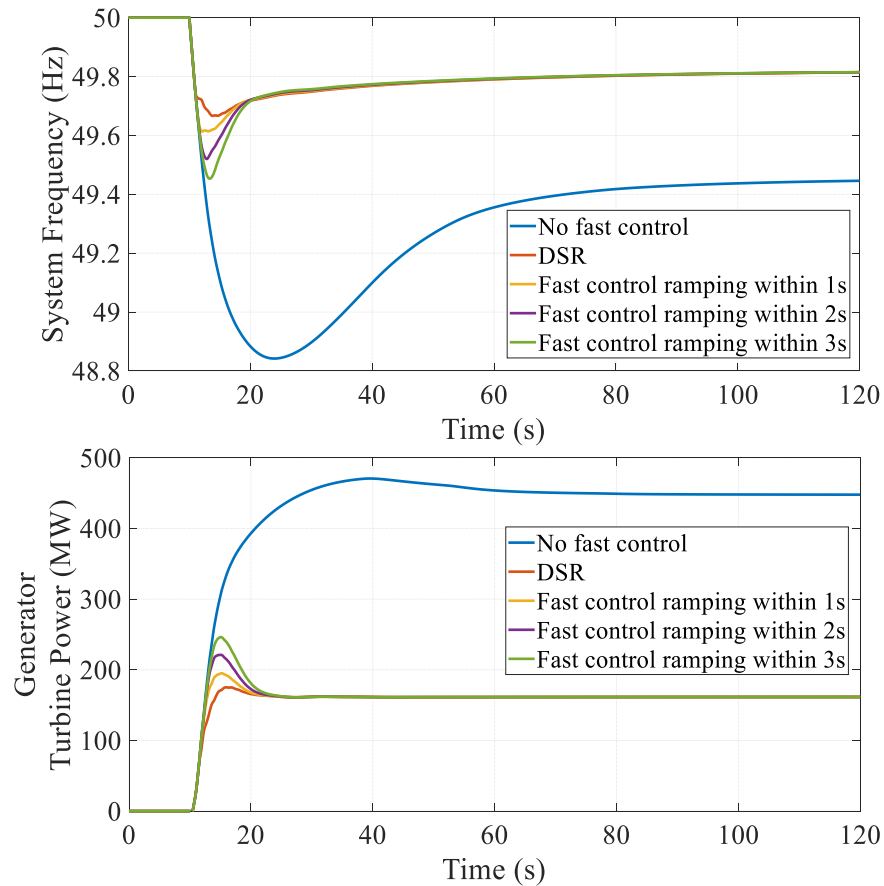


Figure 4-6: Simulation of a 500 MW generation loss in IEEE 39-bus test system with FFR.

Even though there is obvious gap between nadirs, the nadir is effectively improved with 0.35Hz even with minimum 100 MW fast response.

Figure 4-8 demonstrates the benefit offered by fast frequency response when the delay is 1 to 3 seconds after the disturbance. The result is comparable to the study of the ramping speeds shown in Figure 4-5. It can be concluded and confirmed that to overcome the challenge of low system inertia, fast and sufficient active power response is required, which contributes better nadirs and less required primary reserves of conventional units.

4.6 The Impact of High RoCoF on Distributed Generation Operation

In this section, the impact of higher RoCoF on the normal operation of DGs within the distribution networks is presented to understand the effects of low inertia on frequency control and emergency active power balancing. As introduced in the previous section, the Loss

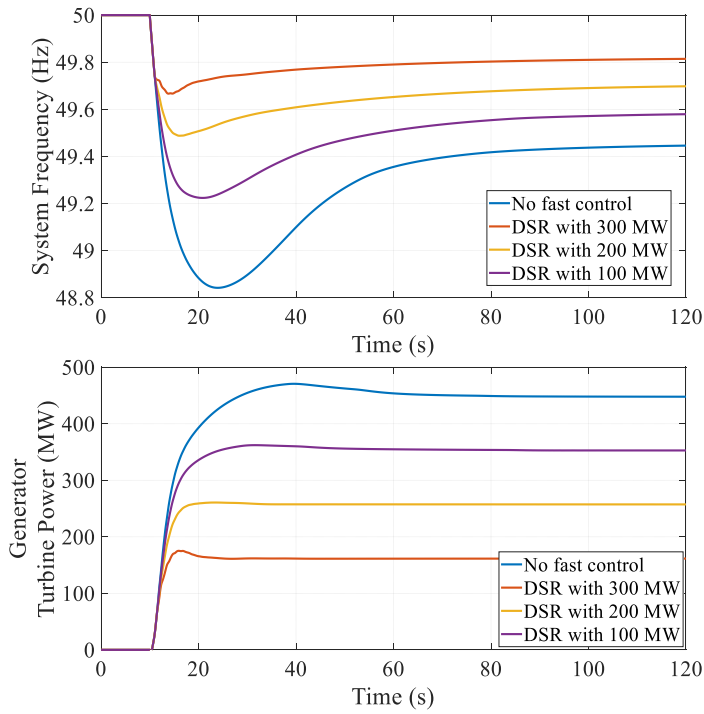


Figure 4-7: Simulation of a 500 MW generation loss in IEEE 39-bus test system with varying amounts of FFR.

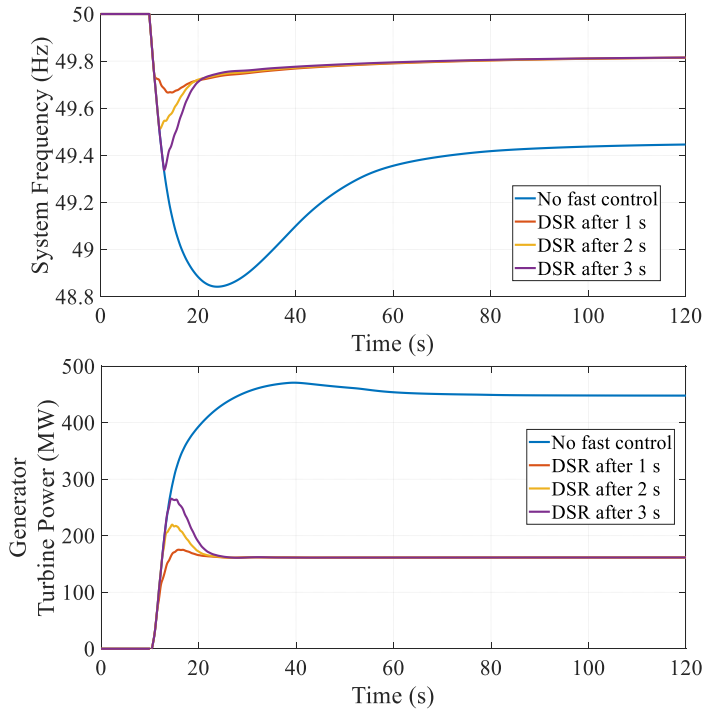


Figure 4-8: Simulation of a 500 MW generation loss in IEEE 39-bus test system with different time delays of FFR.

of Main (LoM) relay of the DG is used to protect the DG in case of an islanding event of the distribution network. RoCoF based LoM relay is therefore studied to understand its

operation under high PE penetration.

In this study, a reduced 36 zone model of the GB transmission system with dynamic models is used. The distribution network is represented via a ‘single node’ system connected to the appropriate zone in the model.

Dynamic transient simulation is performed to study the impact of distribution networks immediately after a major disturbance. Full dynamic studies concentrate on temporal frequency change after a major disturbance; The impact of distribution network resources is examined in more detail.

4.6.1 Reduced 36-Zone GB System Model

Figure 4-9 shows the GB electricity system modelled in DIgSILENT PowerFactory. There are 36 zones while each zone is represented as a double busbar substation. Several types of generators are connected to the busbar, including Gas, Hydro, Nuclear, Bio, etc with dynamic models of generator controllers implemented. Distribution systems are modelled as equivalent PQ loads.

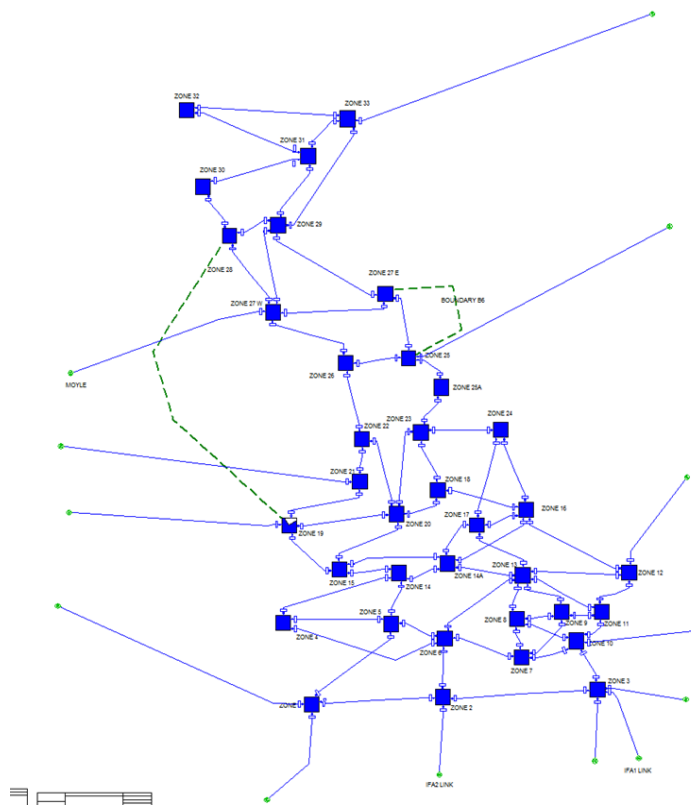


Figure 4-9: Reduced GB 36-zone model in DIgSILENT PowerFactory.

4.6.2 Modelling of Distributed Generation

There are five types of DG for each zone considered. They were Wind (DFIG and Fully converted wind generator), Solar (small and big size) and CHP (Combined Heat and Power) units.

Solar DG are modelled using static generators. The active power generation of them calculated based on the spreadsheet provided by NG. The active power generation of large solar units were considered to be 80 % of the solar generation in each zone and the remainder (20 %) is for small units. For each wind generator, half of the capacity was considered to be DFIG and the other half in full converter. The full converter wind generators have been modelled using static generators. A DSL controller can adjust their output up/down to $\pm 10\%$, based on the change in the system frequency. The CHP generation of each zone has been modelled using a synchronous generator.

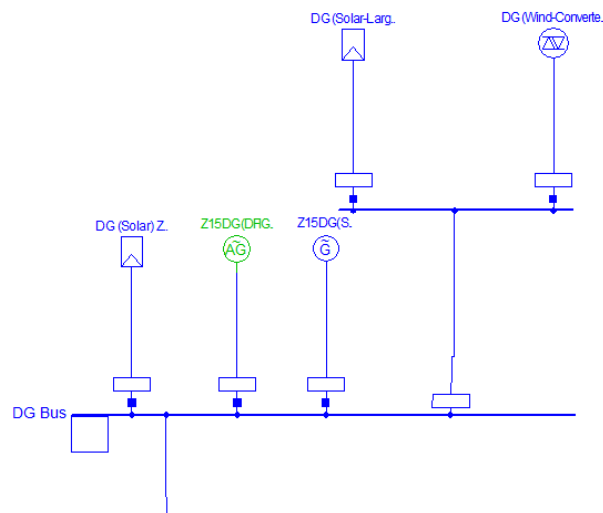


Figure 4-10: Modelling of Distribution Generators in GB 36-zone system.

4.6.3 Modelling of RoCoF Relay and Simulation results

To investigate the impact of the high RoCoF on the RoCoF relay in the distribution network, a RoCoF relay is modelled in the PowerFactory. Several recent research on the design of RoCoF LoM relay has indicated that one of the key challenge is that unsatisfied power quality of three-phase waveforms could cause distortion in the calculated frequency and the RoCoF [69], [70]. Multiple research has put effort improving the quality of the RoCoF

estimation. [71] has utilized an adaptive Kalman which improve the frequency and RoCoF estimation. In [72], a hybrid method to calculate two signals in parallel with accurate measurements for both of steady state signals and fast signal changes after events.

Since the main motivation of this section is to study the impact of inertia reduction on the DG and its RoCoF relay. A typical RoCoF relay design [71] as shown in Figure 4-11 with the schematic diagram of the relay. The frequency is first calculated using three-phase voltage waveforms measured at the relay terminal. Then the RoCoF can be determined by applying a moving window of a few cycles. The resulting raw RoCoF signal is further filtered by a first-order low-pass filter $1/(T_a s + 1)$, which is used to eliminate high-frequency transients.

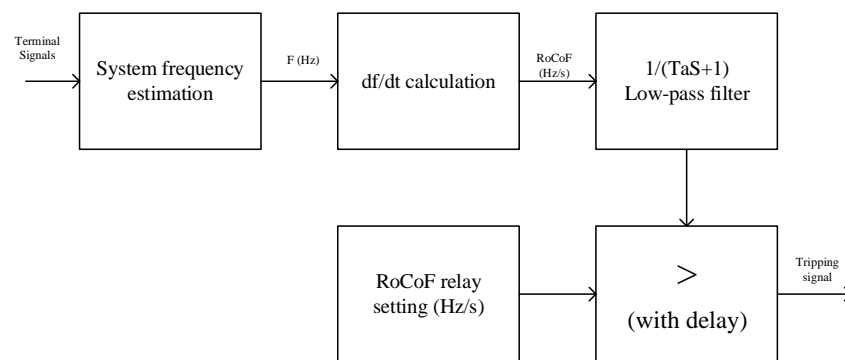


Figure 4-11: Block diagram of the designed RoCoF relay.

Each DG with less than 50 MVA capacity is equipped with a RoCoF relay, which will monitor the frequency of the connected busbar and operate based on calculation results of RoCoF. The RoCoF relay is configured with a 125 mHz/s threshold with 200 ms time delay based on the existing grid code.

The largest single frequency event in the UK is simulated in this section, which is the tripping of a 1.8 GW nuclear power plant. The total system demand is 25 GW in a light loading condition. The total system inertia level is 150 GVA.s. The case shown in Figure 4-12 is under the condition that all RoCoF relays are activated. The left side figure shows the result without RoCoF relay, while the right figure gives the result with RoCoF relay activated. The effect of the governor of synchronous DG is also assessed in this case with the blue curves in which the governor of CHP is activated. When the measured RoCoF violated the pre-defined threshold, the corresponding DG trip out. Both scenarios with RoCoF relay have shown a lower frequency compared to the left case because DG has been disconnected

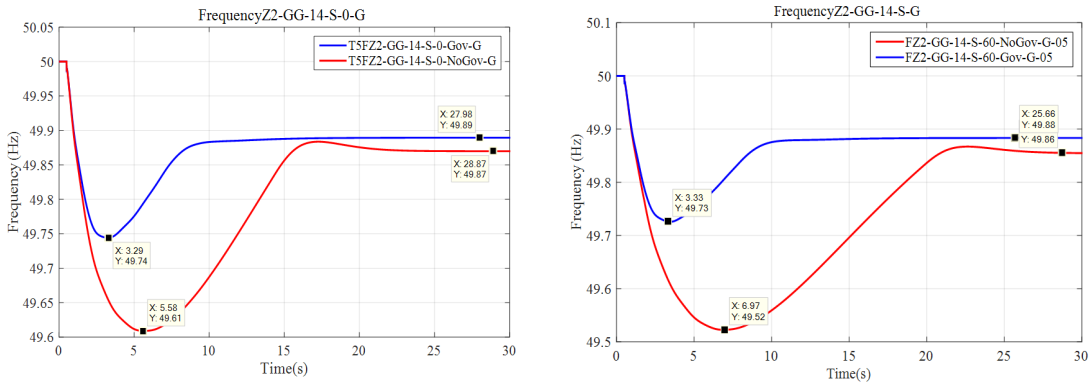


Figure 4-12: Impact of RoCoF relay on frequency response.

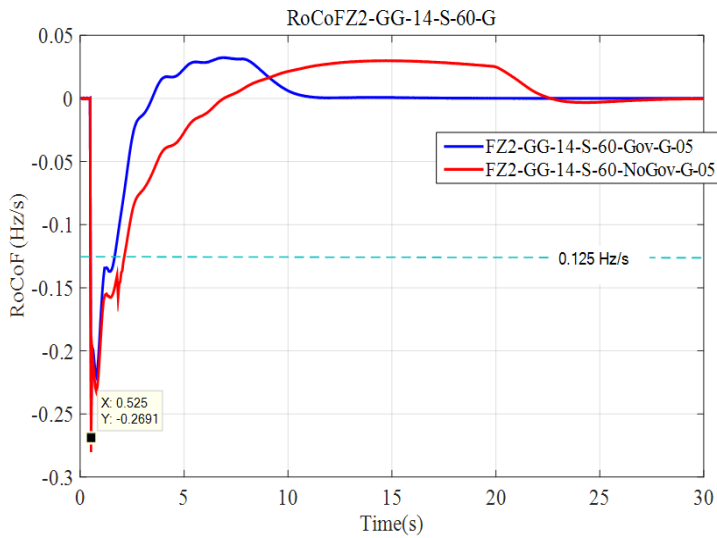


Figure 4-13: Impact of RoCoF relay on system RoCoF.

from the system because of the higher than expected RoCoF, and the active power mismatch is worsened in the case of DG tripping after the initial event. Even though the relay is used to protect the DG from islanding, it leads a further imbalance between power generation and demand. As a result, the increased power imbalance causes worse frequency nadir and longer recovery time.

The RoCoF measured by the RoCoF relay is shown in Figure 4-13, initial RoCoF of both cases dropped to a similar value at the beginning of the event while the case with governor shows a faster frequency recovery speed than the scenario without the governor. It is clearly shown that the RoCoF has violated the 0.125 Hz/s threshold immediately after the event.

4.7 Chapter Summary

The penetration level of non-synchronous generation is increasing. In the UK, National Grid has made prediction of the future inertia showing that the system inertia will migrate from above 250 GVA.s in current heavy loading scenario below 100 GVA.s even at highest demand in the next decade.

Currently part-loaded conventional synchronous generators could be kept online for inertia supporting, instead of being decommissioned. However, this solution will inevitably be replaced due to the excessive cost as those generators will not be able to run at their optimal set point. On the other hand, as the number of conventional synchronous units reduces, the variation of the system inertia becomes more severe as the total amount of inertia is smaller than before.

Simulation testing of existing and emerging frequency control methods on IEEE 39-bus test system under different inertia levels are performed. The results have proved that the reduced inertia is the major challenge for the existing frequency control methods. And there is increasing need for enhanced frequency response and new technologies to overcome challenge brought by low-inertia system.

Chapter 5

Estimation of the Inertia of a Power System

This chapter describes the creation of a novel algorithm for accurate and reliable estimation of system inertia based on wide area measurements of frequency and active power. The importance of inertia and the reason to estimate it are discussed in Section 5.1. In Section 5.2, the inertia calculation application is presented. Section 5.3 presents a robust method to estimate the rate of change of frequency. Section 5.4 provides the results of thorough testing of the new method using computer simulations. Finally, Section 5.5 gives a summary of the chapter.

5.1 Chapter Introduction

As discussed previously, the system's inertia is a critical factor in determining the frequency behaviour following a disturbance of the system's active power balance [40]. The introduction of large quantities of RES, like wind power that is intermittent and cannot produce electricity on demand, will undermine the availability of generation reserves and frequency control services. More importantly, much of the generation capacity provided by RES will offer little or no inertia to the system, as the majority of these energy resources will be connected to the system via converters, causing the total system inertia to be dramatically reduced [19], [73], [74].

In the meantime, The GPS facilitated Synchronized Measurement Technology (SMT)

[31], [75] is introduced to allow system-wide measurements to be used for real-time protection and control actions through Wide Area Monitoring, Protection and Control (WAMPAC) applications. Many of the anticipated developments in power systems will significantly affect the response of the system frequency to a disturbance. The intermittent nature of these technologies will mean that their effects will also be intermittent; causing the frequency response to vary significantly throughout the day. The combination of these factors will cause the inertia of a power system to vary significantly, both with time and location, as referred to chapter 4.

Power systems are protected from dangerous under frequency conditions by deterministic Low Frequency Demand Shedding [10], commonly known as under frequency load shedding (UFLS). Existing UFLS schemes have each stage of shedding deterministically designed in advance, based on thorough system studies. Therefore, this deterministically designed frequency control may prove to be unsuitable, or even incapable, of offering efficient and secure protection in a future where the frequency response of a system will be highly variable.

These challenges will mean that the existing deterministic under frequency protection may need to be significantly changed by using the next generation of Information and Communication Technology (ICT) and Synchronized Measurement Technology to provide novel and adaptive solutions.

The current trend toward the increasing use of wide area measurement devices [32], [75] means that system data with reliable time stamps and a high sampling rate (each 20 ms) will be available to control centres in real time from across the entire system.

The focus of this chapter is to present a new Inertia Calculation Application (ICA) supported by synchronised wide area frequency and active power measurements recorded from across the entire system. The ICA is intended to calculate the generator inertia available in individual system locations, to produce a profile of the inertia available in the system as a whole, after a disturbance has occurred using a methodology based on the swing equation. Knowledge of the different levels of inertia that are across the system could allow under frequency protection to be adjusted online to accommodate the random and uncontrolled variations in a systems frequency response that may occur in the future. The ICA can be classified as a novel WAMPAC application. It can be used as an enabler of other advanced WAMPAC applications, particularly those related to Wide Area Protection and Control, e.g.

Adaptive UFLS, or Smart Frequency Control (frequency control in low inertia systems) [43].

The calculation of a single inertia value for the entire system is acceptable in a strong transmission system with relatively consistent inertia, where consequently the system frequency demonstrates limited variation between locations, like those in contemporary operation. However, this approach fails to accommodate the significant variations in system inertia that are anticipated in future power systems.

The approaches presented in [76], [77] use a calculation method that is based on the swing equation, similar to that used in the ICA. However, there is one significant difference. This is that this previous work was performed before the advent of SMT and as such the estimates were made off-line and used the known size of the disturbance that had occurred to serve as the power imbalance in the equation. This practice will cause a consistent over estimation of the generator inertia, which will increase as the load on the system increases. This is because not all of the power imbalance created by the disturbance will appear at the terminals of the generators, as small quantities of the power imbalance will be absorbed by the other power system components with energy stored within them, such as motors. This causes the size of the imbalance experienced by the generators in the system to be smaller than the imbalance originally created by the disturbance.

Instead of the known size of the disturbance, the ICA uses the measured power imbalance from across the system to allow the generator inertia available in the different parts of the system to be accurately calculated. In this chapter, a new application for the calculation of power system inertia is presented. It is based on synchronised wide area measurements of the frequency and active power.

5.2 Defining the Inertia Constant

As previously defined in chapter 4, the inertia is a measure of the rotational energy, E , stored in a rotating mass as follows

$$E = \frac{1}{2}J\omega_m^2 \quad (5-1)$$

where J is the moment of inertia of the rotating mass (kgm^2) and ω_m is the rotational speed of the rotating mass (rad/s).

In this chapter, the definition of H is then normalised with a single power base, S_b . This normalisation of H means that it now represents the time that the rotating mass could supply

the power equal to S_b with the energy stored.

$$H = \frac{1}{2} \frac{J\omega_m^2}{S_b} \quad (5-2)$$

The H constant of a machine is usually normalised using the rating of the machine. Therefore, before the H constants of different machines can be combined into an equivalent H constant for the system, a base transformation must be applied so that they all appear on the new system base.

The novel method presented in this chapter can estimate the H constant of an entire system or sub-system to serve as an input to the frequency control methods. However, much of the work presented deals with estimating the inertia of a single generator. This is because the H constant of a generator is a known nameplate parameter and as such these single generator estimates can be used to validate the method. This is in contrast to the H constant of a system, the exact value of which has a high degree of uncertainty included in it due to the inclusion of loads in the definition and the unknown properties and connection status of distributed generation.

5.3 Estimating inertia constant using the Swing Equation

From the definition in Section 5.2, it has been established that the H constant of a machine is an accurate measure of the stored energy within the rotating mass of a machine. It is the behaviour of this stored energy during a disturbance that causes the inertia to be of critical importance when attempting to understand and predict the initial frequency behaviour of a system.

When an imbalance occurs in the torques applied over the air gap of a machine this stored energy will act in an attempt to correct the imbalance. This action consists of releasing energy, and decelerating, if there is an excess of electromagnetic torque (for example after a loss of generation in the system) or absorbing energy, and accelerating, if there is an excess of mechanical torque (for example after a loss of load in the system or when the generator becomes islanded from the system). This relationship between the air gap torques and the machine speed is defined using the swing equation (5-4) and is the origin of the frequency deviation that occurs immediately after a disturbance to the active power balance of a system.

5.3.1 Deriving a Suitable form of the Swing Equation

This section details the derivation of a suitable discrete form of the swing equation that can be used to perform the online estimation of the H constant based on wide area measurements of frequency and active power. The swing equation defines the oscillations in the shaft speed that will occur if the shaft is exposed to an unbalanced torque. The basic form of this swing equation is given in (5-3),

$$J \frac{d\omega_m}{dt} = T_m - T_e - D\Delta\omega_m \quad (5-3)$$

where J is the moment of inertia T_m and T_e are the mechanical and electromagnetic air gap torques, respectively. And D is the damping factor of the machine.

As we are mostly interested in the early periods following a frequency event, at which frequency deviation term, i.e., $D\Delta\omega_m$ is much smaller than the other term on the left side of the equation, this term can be safely neglected [17]. Accordingly, equation (5-3) can be simplified to

$$J \frac{d\omega_m}{dt} = T_m - T_e \quad (5-4)$$

However, it is customary to use (5-7), which expresses the swing equation in terms of electrical frequency and active power, when applying the swing equation in power systems.

Therefore, if we multiply both sides of the equation by the synchronous speed ω_{sm} , and assuming that in the period of interest immediately after the disturbance $\omega_{sm} \approx \omega_m$. We can have following expression:

$$J\omega_{sm} \frac{d\omega_m}{dt} = P_m - P_e \quad (5-5)$$

Substitution (5-2) into (5-5)

$$2H \frac{S_b}{\omega_{sm}} \frac{d\omega_m}{dt} = P_m - P_e \quad (5-6)$$

If we convert (5-5) into its per unit format with S_b and ω_{sm} as base value.

$$2H \frac{df}{dt} = P_m - P_e = \Delta P \quad (5-7)$$

where f is the per unit frequency, P_m and P_e are the per unit mechanical power and electrical load applied to the shaft, respectively, and ΔP is the power imbalance at the measurement location.

The inclusion of mechanical power in (5-7) is inconvenient as it not possible to directly measure the mechanical power from the electrical side of the system. This can be overcome by recognising that the variation of the mechanical power will be much slower than the variation of the electrical power because it is governed by mechanisms with larger time constants, e.g. boiler dynamics. This means that when the estimation process is supported by measurements with sufficient reporting rate, e.g. the one per cycle reporting rates offered by modern PMUs [31], then the mechanical power immediately after the disturbance can be assumed to be equal to the electrical power prior to the disturbance. If the reporting rate of the measurements results in a delay of t between each set of measurements then (5-7) can be expressed without the mechanical power term in a discrete form:

$$2H \frac{df}{dt} = P_e(t - \Delta t) - P_e(t) = \Delta P(t) \quad (5-8)$$

This approximation is valid provided that the measurements used are recorded immediately after the disturbance. It is important to recognise the significance of the inclusion of prior to the derivative of frequency term in (5-8). This is included as it denotes the fact the H constant determines the relationship between a change in power and a change in the derivative of frequency. This relationship arises because of the rotational reference frame that is used during the derivation of the swing equation, see Appendix A. In a practical power system the derivative of frequency will never truly be zero due to the constant changes in load and generation that occur. Therefore, when estimating H it is vital that only the change in the derivative of frequency is considered, i.e. any pre-existing value of the derivative of frequency is accommodated in the expression used for estimating H . This can be achieved by modifying (5-8) to form (5-9)

$$\bar{H} = -\frac{1}{2} \frac{P_e(t - \Delta t) - P_e(t)}{\frac{df(t - \Delta t)}{dt} - \frac{df(t)}{dt}} \quad (5-9)$$

where \bar{H} is a close approximation of H and (5-9) forms the basis of the H estimation research presented in this chapter.

The novel estimation process presented in this chapter is based on this discrete approximate swing equation (5-9). Therefore, to produce an estimate, measurement data representing the generator's response to a disturbance in the system's active power balance is

necessary. The required data consists of the active power measurements and the rate of change of frequency for a generator. These measurements should be recorded during a disturbance in the system. Data of this nature will become increasingly available because of the growing deployment of synchronized measurement technology in power systems [31].

5.3.2 Existing H Estimation Methods

Previous work regarding the estimation of system inertia is limited to only a few papers. In 1997 Inoue et al. [78] used a swing equation-based method to estimate the inertia of the 60 Hz system in Japan. The focus of this work was modelling the frequency response of the spinning reserve. This work dealt with M , the coefficient of inertia [40] or mechanical starting time [10], where $M = 2H$ and H is treated as the inertia constant here. The estimation procedure used was based on the known size (in MW) of ten disturbances and the frequency transients measured at a single location in the power system.

In 2005 Chassin et al. [77] attempted to identify a link between the system inertia, estimated using the swing equation, and the system load. Estimates of M were made using post-mortem data regarding the disturbance size, and the frequency during the disturbance measured at a single location.

The work presented in [76], [77] was performed off-line and used data recorded from only a single location to calculate the inertia of the entire system. This differs from the ICA quite significantly, this is because the intent of the ICA is to allow a profile of the inertia available across the system to be calculated immediately after a disturbance has occurred, rather than calculate a single value that represents the total inertia of the system.

The existing work that describes the estimation of H did not have the benefit of access to SMT and WAMPAC. This meant that the method had to be implemented offline during post-mortem analysis, as the lack of accurate time stamps meant the data had to be aligned properly before use. Furthermore, only measurements of frequency were available in this previous work. The lack of active power measurements meant that the known size of the disturbance (P_d) was used to serve as the power imbalance, so (5-9) is replaced with the following expression:

$$2H \frac{df(t_d)}{dt} = P_d \quad (5-10)$$

where t_d denotes the time at which the disturbance was deemed to have begun to influence the frequency response.

The use of only a single measurement of the derivative of frequency leaves this process vulnerable to noise, particularly as the derivative process serves as a noise amplifier, as any error in the derivative of frequency value will be directly included in the H estimate. For the purposes of the discussion presented in this chapter, this approach is referred to as the single value method.

Due to the lack of active power measurements, the single value method assumes a known disturbance size (P_d) to serve as an approximation of the power imbalance. It is important to recognise that in a real power system estimates made using (5-10) will differ somewhat from estimates based on (5-9) and active power measurements, like those proposed here. These differences occur because not all of the active power imbalance created by the disturbance will appear across the air gaps of the machines in the system, instead, some of this imbalance will be accommodated by the other elements of the system e.g. voltage and frequency dependent non-rotating loads. This will mean that H estimates made using P_d will include this response and as such, they will usually be larger than H estimates based on active power measurements. This inclusion of the response of other system elements into the estimate will mean that the H estimate may vary significantly with the type and location of the disturbance, whereas estimates based on active power measurements will not.

5.4 Inertia Calculation Application

In this section, the Inertia Calculation Application (ICA) will be presented. The method is based on simultaneously measuring the frequency and active power after a disturbance. Here, disturbance refers to any event that creates a large and sudden mismatch between the generated and consumed active power.

A suitable approach for recording the necessary simultaneous measurements is a Wide Area Monitoring System (WAMS) based on SMT. The main building blocks of SMT are Phasor Measurement Units (PMUs), Data Concentrator(s) (DCs) and the communication infrastructure necessary for transferring data from the PMUs to the DCs [75]. A WAMS of this nature would have the generic architecture shown in Figure 5-1 and s_i denotes the vector of necessary information transferred from every installed PMU to the central DC, in

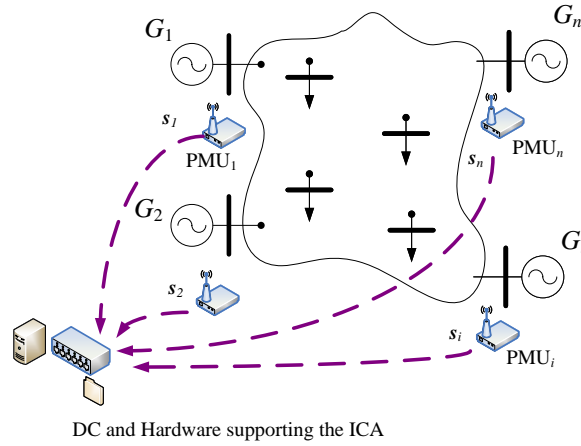


Figure 5-1: A generic WAMS architecture that could support the ICA.

which the ICA is computationally executed. Each of these vectors s_i ($i = 1, \dots, N$, where N is the number of generators connected to the system) contains time-stamped frequency and active power measurements from the PMU installed at the terminals of the i -th generator. The purpose of the data contained in the vector s_i will be explained in detail in the method definition.

5.4.1 ICA Execution

The ICA must be initialised immediately after detecting a disturbance. Two consecutive sets of N measurement vectors, s_i , serve as the input for the ICA.

The starting point for the development of the ICA is the generator swing equation (5-11), which defines the relationship between the power imbalance, Δp_i , and electrical frequency, f_i , at the terminals of a single generator, i , immediately after a disturbance.

$$\frac{2H_i}{f_n} \frac{df_i}{dt} = p_{m,i} - p_{e,i} = \Delta p_i \quad (5-11)$$

where H_i is the inertia constant of that generator in seconds, df_i/dt is the rate of change of the electrical frequency at the terminals of the i -th generator in Hz/s, f_n is the system nominal frequency in Hz, $p_{m,i}$ is the mechanical power generated by the i -th generator in p.u., $p_{e,i}$ is the electrical load at the terminals of the i -th generator in p.u. and δp_i is the power imbalance at the terminals of the i -th generator in p.u.

If the instant of the disturbance is known, and the size of the power imbalance and rate of frequency change associated with the disturbance are available, the unknown inertia

constant can be directly determined from (5-11) as below

$$H_i = \Delta p_i f_n \left/ 2 \frac{df_i}{dt} \right. \quad (5-12)$$

Equation (5-12) is only valid immediately after a disturbance, a time referred to as $t = 0^+$. After this time other factors, not accounted for in equation (5-11) (e.g. generation unit controls, load response, series compensation, storage, spinning reserve, HVDC, AGC, LFC), begin to affect the dynamic behaviour of the system. The rate of frequency change used in (5-11) can be determined using two consecutive frequencies measurements:

$$\frac{df_i}{dt} = \frac{f_i(t^+) - f_i(t^-)}{t_i^+ - t_i^-} \quad (5-13)$$

where $f_i(t^+)$ is the frequency in Hz sampled after the disturbance; $f_i(t^-)$ is the frequency in Hz sampled before the disturbance; t^- and t^+ represent the times of the measurements before and after the disturbance, respectively. All of these values refer to the i -th generator. In order to achieve an accurate measurement of the rate of frequency change, the measurements must be made at a sufficiently high sampling frequency. In our approach, introduced in the next section, we concluded that the acquisition of frequency measurements once every cycle, e.g. a sampling frequency of 50 Hz for a 50Hz system, would satisfy the accuracy requirements for the ICA. A sampling frequency of this size is well within the capabilities of modern PMUs based on multiprocessor hardware platforms.

The power imbalance, Δp_i , used in (5-12) is defined in terms of mechanical and electrical power. However, the power imbalance can be redefined solely in terms of electrical power considering the following properties of a power system:

- Mechanical power changes slowly when compared to electrical power and
- Frequency control balances the mechanical and electrical power within the generator so they are approximately equal before a disturbance.

These properties allow the electrical power measurements made before the disturbance to be used instead of mechanical power in the power imbalance definition (i.e. $p_{mi} \approx p_{ei}(t^-)$). In conclusion, the power imbalance for the i -th generator, δp_i , in (5-12) can be determined by using the following formula:

$$\Delta p_i \approx p_{ei}(t^-) - p_{ei}(t^+) \quad (5-14)$$

where $p_{ei}(t+)$ is the electrical power measured after the disturbance in p.u. and $p_{ei}(t-)$ is the electrical power measured before the disturbance in p.u.

Equations ((5-12))-((5-14)) allow the inertia constant of the N generators in the system to be calculated using only the data contained in the two sets of N measurement vectors, s_i , provided by the supporting SMT.

If a generator is disconnected from the system it is important that it is excluded from the ICA, as it no longer forms part of the system response. The exclusion of measurements from a disconnected generator can be achieved by defining a binary variable o_i . This variable is set to 1 if a generator is connected and 0 if it is not. This variable does not necessarily need any additional information from the system as the existing measurements could be used to determine the status of the generator.

The system, H_{sys} , can now be calculated as a sum of the individual inertia constants, H_i , of all the generators connected to the system:

$$H_{sys} = \sum_{i=1}^N o_i H_i \quad (5-15)$$

where o_i is a binary variable that is 1 if the i -th generator is connected to the system and 0 if it is not. The inertia of each of the N individual generators, H_i , is estimated using (5-12).

The N generators referred to in this discussion could include every generator in the system, or only the generators in the specified areas the ICA is executed for.

5.5 Estimation of the Rate of Frequency Change

To estimate the unknown rate of change of frequency (RoCoF), the following linear frequency model was assumed:

$$z(t) = x_1 + x_2 t + \xi(t) \quad (5-16)$$

where x_1 is the average frequency, x_2 is the unknown rate of frequency change and $\xi(t)$ is the random noise. Assuming that the input signal is uniformly sampled with the sampling frequency f_s and the sampling period $T_s = 1/f_s$, the value of t at a discrete time index is given by $t_k = kT_s$ and the following discrete representation of the signal model should be used:

$$z_k = x_1 + x_2 t_k + \xi_k, \quad k = 1, \dots, p \quad (5-17)$$

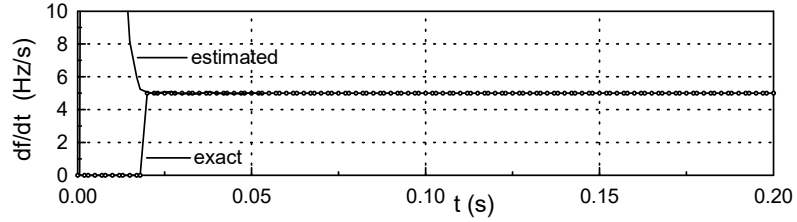


Figure 5-2: Estimated test signal rate of frequency change.

where all unknown parameters in (5-17) now have the subscript k . The following matrix equation for all samples, belonging to the data window, can be established:

$$\begin{bmatrix} z_1 \\ \vdots \\ z_p \end{bmatrix} = \begin{bmatrix} 1 & T \\ \vdots & \vdots \\ 1 & pT \end{bmatrix} \begin{bmatrix} x_1 \\ x_2 \end{bmatrix} + \begin{bmatrix} \xi_1 \\ \vdots \\ \xi_p \end{bmatrix} \quad (5-18)$$

The system of linear equations (5-18) can be now presented as follows:

$$\mathbf{z} = \mathbf{H}\mathbf{x} + \boldsymbol{\xi} \quad (5-19)$$

By this, an overdetermined system of linear equation is obtained. It can be solved using the traditional Least Squares Method, which minimises the sum of error squares:

$$\hat{\mathbf{x}} = (\mathbf{H}^T \mathbf{H})^{-1} \mathbf{H}^T \mathbf{z} = \mathbf{H}^\# \mathbf{z} \quad (5-20)$$

For $p = 2$, one directly obtains:

$$x_2 = \frac{\Delta f}{\Delta t} = \frac{z_2 - z_1}{T} \quad (5-21)$$

To demonstrate the above numerical algorithm for estimation of the unknown rate of frequency change, let us assume a sinusoidal test signal with an artificial frequency step change from 50 Hz to 55 Hz at 0.02 s and further constant frequency change 5 Hz/s. Let us also assume that the frequency has been measured using one of the existing algorithms, e.g. [79], [80]. By setting data window size for the rate of frequency estimation to 20 ms, the rate of frequency change presented in Figure 5-2 is obtained. It is obvious that the method is suitable for processing of signals with even faster frequency changes compared to those encountered in real power systems.

From the perspective of practical application of any numerical algorithm for measurement of the RoCoF, one has to consider a very high sensitivity to the quality of frequency

measurement. The actual power system frequency varies in a very narrow range, for example ± 0.5 Hz, which is the statutory limit in GB power system. Consequently, the RoCoF measurement is quite a challenging task, particularly if the measured frequency contains noise. Using larger data window sizes, the accuracy of RoCoF measurement can be improved but causing this unacceptably long delay in any application relying on RoCoF. That is why the quality of frequency measurement must be as better as possible, so that the data window size can be shortened, allowing the application to respond faster.

5.6 ICA Testing and Validation Through Computer Simulated Tests

The behaviour of the ICA presented in this chapter can be investigated through computer-based dynamic simulations of power systems of different complexity. For this purpose, two test systems were used:

The first test system consists of a single synchronous generator connected directly to a static constant power load. This test system is used to demonstrate the proper behaviour of the method in the simplest case of inertia estimation. Disturbances are created using load step changes, representing both load increases and decreases.

The second test system consists of an IEEE 9-bus 3-machine test system. This test system is used to test the behaviour of the ICA in a multi-machine system, for different types and size of disturbances. Simulations performed using this system will give some indication of the influence of various system properties on the reliability of the ICA.

The frequency response of both test systems was simulated using DIGSILENT PowerFactory. The ICA execution was implemented in MATLAB.

5.6.1 Single-machine Test System Case

The single-machine test system consists of a gas turbine generation unit connected directly to a single static load. The unit is rated as a 210 MVA, 50 Hz synchronous generator with inertia constant of 7.334 s on a 210 MVA base. The load has a constant power consumption of 100 MW and 50 MVar. The active power demand was step changed by ± 25 ± 50 ± 75 ± 100 MW to provoke system frequency changes. Note that negative values denote a

reduction in load. Figure 5-3 and 5-4 show the frequency response and the derivative of this frequency for these load changes in the single-machine test system.

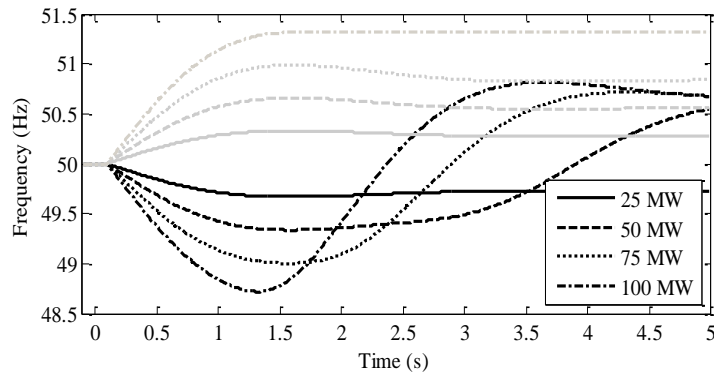


Figure 5-3: Frequencies for a single-machine test system; the black and grey lines denote a load increase and decrease respectively.

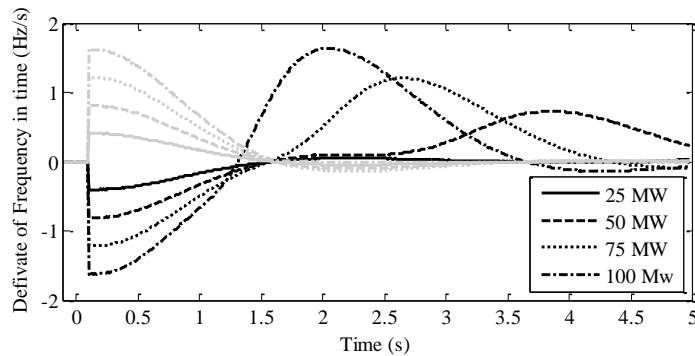


Figure 5-4: Frequency derivatives for a single-machine test system, the black and grey lines denote a load increase and decrease respectively.

The shapes of the frequency response curves are different for a step increase and decrease in the load. This is due to the characteristics of the generator controller and its growing influence over the frequency response within a few seconds of the disturbance occurring. This difference in frequency behaviour will not influence on the behaviour of the ICA as the frequency measurements used are taken before this controller action occurs.

The curves of the derivative of frequency are shown in Figure 5-4. It is evident that larger load changes produce larger excursions in the rate of change of frequency.

Table 5-1 shows the calculated inertia H_{est} , produced by the ICA for different load step changes and relative errors. The relative errors are calculated by,

$$Error = \frac{H_{est} - H_{sys}}{H_{sys}} \cdot 100\% \quad (5-22)$$

where H_{est} is the estimated inertia and H_{sys} is the system inertia.

Table 5-1: Inertia calculation errors for the single-machine test system.

Dp (MW)	df/dt (Hz/s)	Hest (s)	Error (%)
-100	-1.62	7.34861	0.05
-75	-1.208	7.3912	0.64
-50	-0.8121	7.32961	-1.96
-25	-0.4059	7.33232	-0.16
25	0.4059	7.33232	-0.16
50	0.8121	7.32961	-1.96
75	1.208	7.3912	0.64
100	1.62	7.34861	0.05

It is noticeable in Table 5-1 that the derivative of the frequency at $t = 0^+$ is of the same magnitude for a load increase and decrease of the same size, with the only difference in the two data values being that the signs are inverted. The errors obtained are negligible from a practical viewpoint. The maximum error in the inertia estimation is for load changes of $\pm 50\%$ (the estimates produced for both a load increase and decrease were the same).

These results demonstrate two properties of the ICA: 1) The error in the estimate of the inertia is the same for load changes of the same size, regardless of whether changes represent a load increase or decrease; 2) The estimation method is generally reliable despite the variation in the disturbance size.

5.6.2 Multi-machine Test System Case

The multi-machine test system (see Figure 5-5 and for a detailed description [81]) simulations were performed to determine if the properties identified in the single bus case held true for a more complex system, and to investigate the impact of network properties on the performance of the ICA.

The simulations performed consisted of load step changes at each load bus, using 25% steps like those used in the single bus case. In addition to these load change simulations, the inclusion of multiple generators allowed the simulation of sudden generator disconnection disturbances to be included. It is important to note, the systems net load of 320.2 MW, is used as the base, SB, for the inertia estimates. A base conversion, from the individual generators ratings to the system base, gives the inertia of G1, G2, and G3 as 7.38 s, 2.00 s and 0.94 s, respectively.

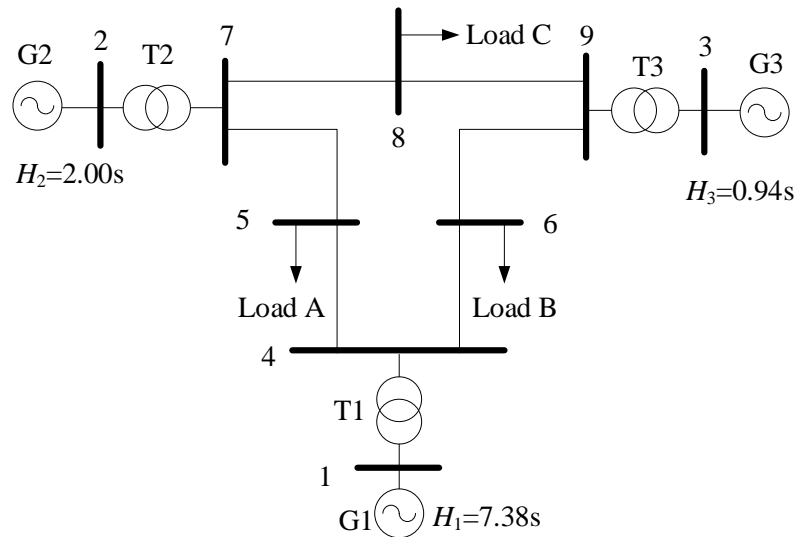


Figure 5-5: Three-machine, 60 Hz test power system.

Figure 5-6 shows the equivalent system frequency, calculated using the frequency of the centre of inertia method, and its rate of change data for a single case of each disturbance considered (changes at Load A, B and C and outages of G1, G2 and G3). Note that the frequency of COI is calculated as an inertia weighted sum of the frequency of each generator in the system, as described in [10], and represents the equivalent frequency behaviour of the system. In Figure 5-6 it is noticeable that the system frequency for an outage of G1 is unstable, demonstrated by a second frequency decline at approximately 2.5 s. However, based on the comparison of the estimate errors seen in Table 5-2 the system's instability has not compromised the performance of the estimation method. This is not surprising given the fact that the instability occurs after the disturbance and, therefore, after the moment the data used by the ICA was collected but it is a vital property of the ICA as it will allow the inertia estimates to contribute to adaptive actions that could prevent this instability.

Table 5-2: Results of the estimated inertia of the 3-machine test system.

Event	Δp (MW)	H_{actual} (s)	df_c/dt (Hz/s)	$H_{estimated}$ (s)	Error (%)
Gen 1 out	-71.64	2.9873	-1.07025	2.97238	0.49952
Gen 2 out	-163	8.45426	-1.67206	8.55272	-1.1647
Gen 3 out	-85	9.53044	-0.8339	9.39125	1.46055
Load A	80		0.68824	10.55725	-0.67951
Load B	40	10.486	0.25385	10.4673	0.17829
Load C	30		0.33891	10.75954	-2.60867

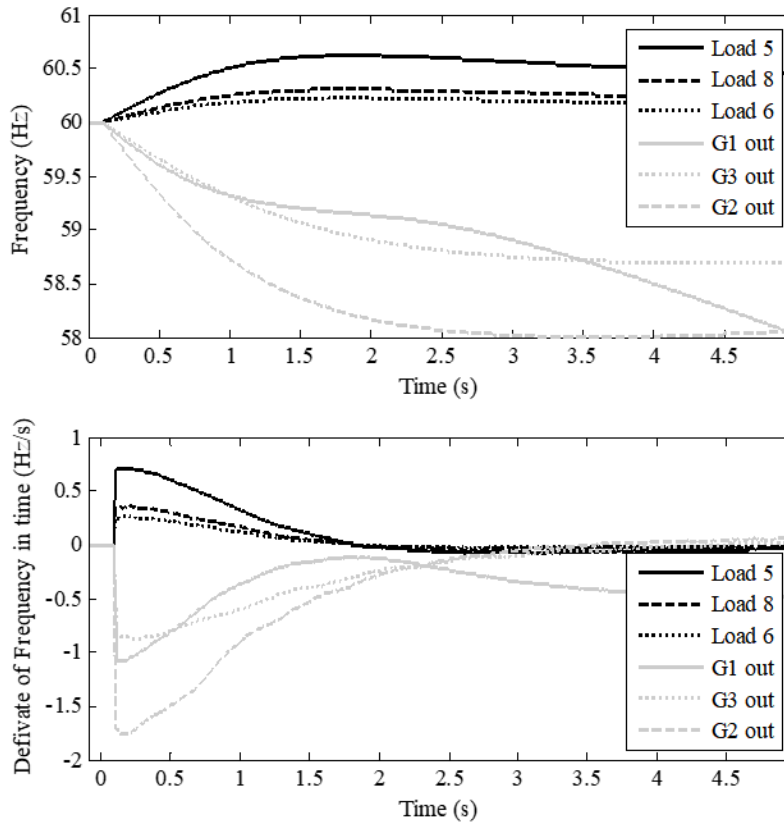


Figure 5-6: Frequency response of COI for tests with the 3-machine tests system.

The results in Table 5-2 show that the ICA can be used to produce reliable estimates of system inertia regardless of the magnitude of the system inertia. This can be stated Table 5-2 based on because the disconnection of a generator changes the system's inertia, at the moment of its disconnection, so the system inertia for the data collected at $t = 0^+$ is only dependent upon the remaining, connected, generators. The new system inertia for each generator disconnection is given in Table 5-2. It is clear that the errors obtained do not vary in an extreme way for the four different values of system inertia seen in the table.

Taking the current and forecast system inertia condition of the GB power system, presented in Chapter 4, we are typically looking at a range of 100 - 200 GVA.s in the next 5 - 10 years. If we take proposed method and apply in the GB system, assuming a similar performance in the real with a good quality of the input signal, the error level observed will be 3 GVA.s maximumly, which give an accurate estimation of the inertia with a resolution to distinguish a typical 300 - 500 MW power plant switching on and off.

5.7 Chapter Summary

This chapter presents a novel algorithm of Inertia Calculation Application (ICA), based on wide area measurements, that can be used to accurately calculate the system inertia online.

The algorithm takes wide area measurements of frequency and electrical power output from the terminal of each generator in the system. Then swing equation is used to estimate the individual inertia of each generator. The sum of all estimated individual inertia will be the overall system inertia.

From the results presented in section 5.6, it is evident that the accuracy of the power system inertia estimates is independent of the type, size, and location of the disturbance during which the necessary data is gathered.

The computer simulated testing of the ICA has shown that it is accurate and reliable. This system inertia information would be useful for system operators working in an environment where changes to the nature of large power systems (e.g. a high penetration of RES) had caused the system inertia to become quite variable and potentially reduced to a level where system security may be compromised. The ICA is also capable of producing accurate estimates of the inertia of individual generators, or parts of the system as long as the power imbalance of the device or region of system can be accurately monitored. This research has also made a fundamental stone for applications based on the estimated inertia of the method, which are represented in chapters 7 and 8.

Chapter 6

Development of an RTDS

Hardware-In-the-Loop Testbed

This chapter describes the construction of a novel RTDS based testbed providing high-fidelity real-time simulation capability. The necessity and benefit of conducting real-time closed-loop testing are discussed in Section 6.1. Section 6.2 introduces the simulator and associated types of equipment of the testbed. Section 6.3 discusses different methodologies of conducting real-time testing. Section 6.4 summarises the chapter.

6.1 Chapter Introduction

The previous chapters assessed the significance of inertia estimation. As mentioned above, renewable resources connected to a system has a great impact on the system and new frequency control methods are required to be developed. However, it is difficult to quantify the effectiveness of proposed methods especially for WAMPAC applications due to the variation and complexity in the real-world power system, and more importantly there is no such WAMPAC which the proposed algorithm can use.

Even there is a such WAMPAC, a number of reasons will prove this is not practical. No utility would permit such a scheme to be tested on a critical system for which they are responsible. The best alternative is to construct a high-fidelity real-time model of a real power system and test algorithms on it, which is the real-time simulation. To facilitate WAMPAC application testing, a Real Time Digital Simulator testbed is developed associated with a number types of equipment(e.g, Time clock, network switch).

6.2 Real Time Digital Simulation

The Nyquist Criterion indicates that the sampling frequency (F_s) must be at least twice the frequency under study [82]. This is because aliasing occurs in the frequency domain at frequencies above F_s , so that the frequency spectrum is mirrored about this frequency. The Real Time Digital Simulator (RTDS), however, is a dedicated hardware unit capable of solving arbitrary system topologies in a time step of $50\mu s$, which is fast enough to perform most simulation cases.

In the case of the RTDS, the small time step is achieved in real time through advanced parallel processing techniques. Several processors mounted on racks solve individual models and communicate with each other sub-time step so that the entire network solution can be solved in a base frame rate of $50\mu s$. The user is able to draft power systems of arbitrary complexity, the size of which is limited only by the amount of processing power available. These can then be run in real time, with the user interacting through control actions, and observing the response of the power system [83].

RTDS processor cards are mounted in card cages, known as racks, which are housed in cubicles along with input/output cards, power entry components, power supplies, and other necessary components. The I/O cards can permit the RTDS hardware to be interfaced with external equipment such as controllers, protective relays or amplifiers.

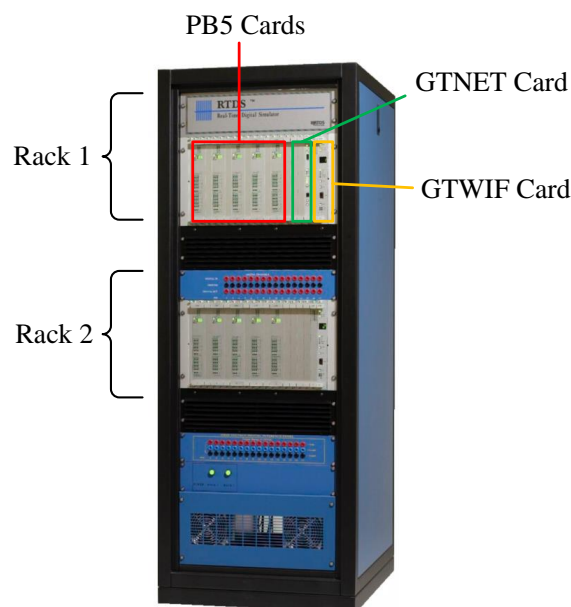


Figure 6-1: RTDS cubicle and its key components.

It is of course vitally important in the RTDS simulation that the base time-step of $50\mu s$

is adhered to for the duration. Communication between cards is achieved via the RTDS's backplane, a bus coordinated by the workstation interface card (WIC). This ensures that all relevant information is passed between processors sub-time step. The WIC card also handles LAN based user communications between the RTDS and the workstation. This allows user interaction in runtime and updates real-time displays such as plots and meters. Further information regarding RTDS hardware can be found in [84].

6.3 Hardware and Software Integration

This section describes all key internal hardware RTDS and external equipments of the testbed. Software used to facilitate the hardware is also presented. The whole architecture is given in Figure 6-2.

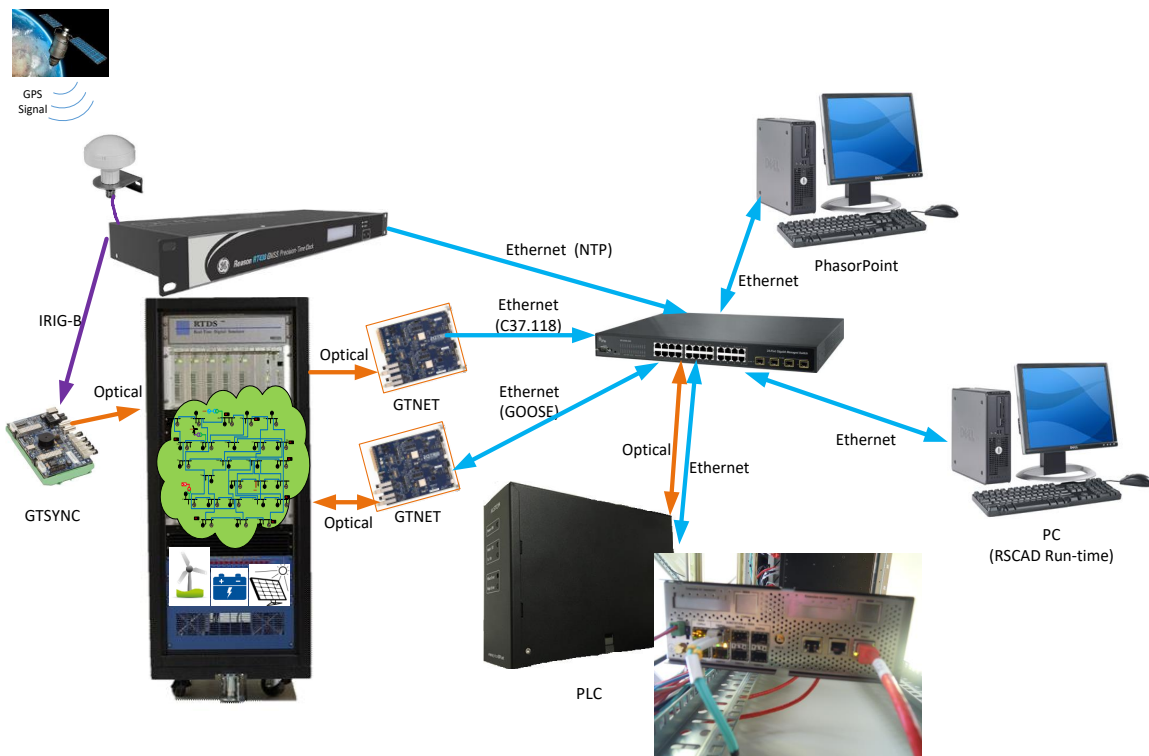


Figure 6-2: RTDS testbed architecture and communication infrastructure.

6.3.1 Hardware

To perform real-time digital simulation for WAMPAC applications, following RTDS components and equipments are implemented and configured:

RTDS PB5 card

The PB5 processor card is one of the latest generation of processor card developed for the RTDS simulator. The PB5 is a powerful computational unit which is used for solving the overall network solution and auxiliary components, such as transmission lines, generators and Power Electronic Converters. Each PB5 card contains two Freescale MC7448 RISC processors operating at 1.7 GHz.

Using PB5 cards based racks, it is possible to run one or two network solutions components on one rack. Each network solution component can support a maximum of 90 single-phase nodes or 30 three-phase busbars. Therefore, 2 subsystems with 90 nodes each can be included on one rack. The rest of PB5 processors can be used to solve simulated network component models.

Each PB5 card also includes 24 non-isolated 12-bit digital to analogue converters. Eight optical ports that can be used for connecting to high resolution digital and analogue I/O cards or for direct communication between PB5/GPC processor cards are supported as well.

RTDS GTWIF card

The Giga Transceiver Workstation InterFace card, GTWIF, is a PPC405 based processor card [84]. The GTWIF's primary function is to manage communication between the RTDS and the workstation of the host computer using Ethernet TCP/IP based communications. The GTWIF card provides the following functions:

- Loading, starting and stopping cases
- Timestep generation
- Internal synchronisation between racks with the Global Bus Hub (GBH)
- Manage all backplane transfers during simulation
- Diagnostics of the hardware
- Communication with RSCAD software

RTDS GTSYNC card

The GTSYNC card takes an external time reference (e.g. GPS clock) and use it to synchronise the RTDS simulation timestep. The GTSYNC card supports 1 Pulse Per Second (1PPS) over BNC coax or ST type fibre connectors, IRIG-B over BNC coax connector, as well as IEEE 1588 over RJ45 or ST fibre connectors which support various devices under test.

Synchronisation of the simulation timestep to an external time reference is essential for any PMU testing, WAMPC applications and IEC 61850 automation. The GTSYNC connects through a GT port on the GTWIF.

RTDS GTNET card

The Giga-Transceiver Network Communication Card, provides a real-time communication interfaces to and from the simulator via Ethernet. Different protocols are used with the GTNET depending on the applications. The different protocols include TCP/UDP socket communication, IEEE C37.118 data output streams, IEC 61850 GSE binary messaging, IEC 61850-9-2 sampled values, DNP3 communication, IEC 60870-5-104 protocol and playback of large data files stored on a PC storage.

In the cases of validation of wide area based frequency control, the GTNET card can run PMU protocol to generate IEEE c37.118 data stream to external controllers and Data Concentrators. IEC 61850 protocol can also be activated by an additional GTNET card to receive command in GOOSE message from external controllers.

Time Synchronisation Equipment

The demand for accurate time synchronisation available 24/7 increases with the growth of critical substation applications, such as phasor measurement, merging units, travelling-wave fault location and current differential protection operating. For WAMPAC study, the time clock signal is needed to be feed to the physical and virtual PMUs in the testbed. In this setup, a Reason RT430 GNSS Grandmaster Clock is used, providing a clock reference from GPS and GLONASS satellites.

The time clock transmits clock signal through I-RIGB and NTP protocol, which are adopted by different devices of the testbed.

Ethernet Switch

Ethernet is one of the commonly used communication protocol due to its simplicity and reliability. Ethernet communication has the advantages of higher transfer speeds, full duplex and collision-free operation, fibre optic interface, remote monitoring and diagnostic support which make it viable for power system operation and control [85]. A 100 Mbps Ethernet network is used in this testbed with a Reason S20 Managed Ethernet Switch providing copper and fibre optic interfaces as well as network management.

Programmable Logic Controller

A Programmable Logic Controller (PLC) is a standalone system which is capable of continuously executing calculation and making decisions through the embedded program, taking real world analog and digital signals as inputs. In this testbed, a GE phasor controller is used.

Workstation

A number of PCs are implemented to perform modelling and control of RTDS and to operate as a data recorder for PMU streams and simulation results.

6.3.2 Software

RSCAD

RSCAD is a user-friendly software to interface with RTDS. It allows the user to perform all of the necessary steps to prepare and run simulations, and to analyse simulation results – all without the use of third-party products, which can be challenging to maintain and troubleshoot.

RSCAD also provides sophisticated PMU model and IEC 61850 configuration functions, which can be efficiently utilised to interact with external devices in the WAMPAC study.

Data Concentrator

The primary function of a DC is to receive data from PMUs and DCs that are lower in the data hierarchy, perform some form of bad data rejection and then align this data into

a coherent record that can be used. The coherent data record can then be transmitted to applications or other DC. In this testbed, a workstation running PhasorPoint [85] software operates as the DC of the testbed. An alternative open-sourced DC software OpenPDC [86] is also implemented. Both software is capable for collection and visualisation of PMU data.

PLC Programming Software

To develop a proper programme in the PLC, Straton software [87] is an integrated development tool based on IEC 61131-3 programming languages offering a wide selection of features and communication protocols. Straton Runtime is independent and can easily be used on the PLC controller (e.g., GE Phasor Controller) of the testbed.

6.3.3 Power System Model

A number of widely used power system benchmark model are modelled and modified to be implemented with RES, including Kundur's two area system, IEEE 9-bus test system, IEEE 39-bus test system and a customised GB test system. A brief description is given in the following section and the detailed topology and data of the network can be found in the Appendix.

Kundur's Two-Area System

The two-area system used is example 12.6 at page 813 in [10], comprises two similar areas connected by a weak tie line in the middle. As a test case, it is outstanding for the study of inter-area oscillation and frequency stability and control. Due to smaller scale of the network which consume less computing power of RTDS, detailed high-fidelity models of wind and HVDC can be implemented into the system to create scenarios with high penetration of RES.

IEEE 9-bus Test System

The IEEE 9 bus power system represents a reduced equivalent of the Western System Coordinating Council (WSCC) system. The base voltage levels are 230 kV, 18 kV, 16.5 kV, and 13.8 kV. The WSCC 9-bus test system has relatively smaller numbers of generators,

lines and loads and it is easy to control for initial testing and validation. Similarly, detailed high-fidelity RES model is implemented.

IEEE 39-bus Test System

This IEEE 39 bus system is well-known as 10-machine New-England Power System. Generator 1 represents the aggregation of the external system. To implement RES model into the standard IEEE 39-bus system, it is not feasible to have detailed model at every RES location as it would require significant amount of RTDS hardware resources. To obtain high efficiencies at the rated VSC power, the switching times of the PWM pulses should ideally be low ($< 1\mu s$). Typically, the switching frequencies of VSCs are at least ten times higher than the nominal AC grid frequency. To capture the high switching frequency VSC dynamics in real-time, the RTDS small time step capability is used to simulate the converter circuit. The small time step simulation uses dedicated hardware resources. The required computation resources increase with the number of VSC interfaced sources in the simulation.

Therefore, with limited RTDS resources, it is not feasible and necessary to include detailed RES model in a large system as the focus of the study in this thesis is the impact of RES on system frequency control. Thus, a simplified PQ power source model that represents the steady-state and transient behaviour of VSCs without requiring small time step models is used, as shown in Figure 6-3. The dynamic of the model is achieved by modelling the outer loop of VSC controls and power system circuit which significantly reduces the time and computation resources required for detailed modelling of VSC sources.

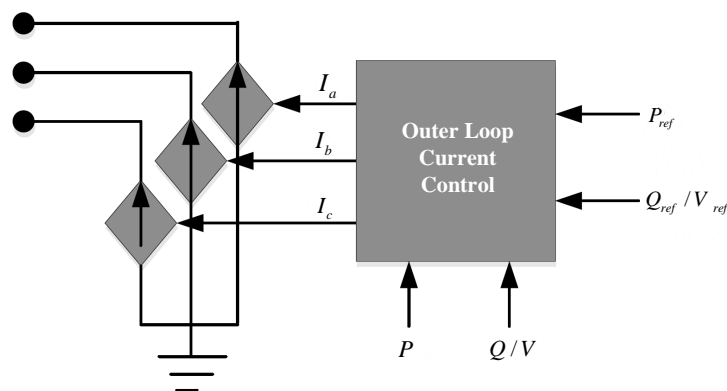


Figure 6-3: PQ power source model in phase reference.

GB Test System

The GB test system consists of an onshore transmission network covering England, Wales and Scotland. It is owned and maintained by three regional transmission companies, National Grid, Scottish Power and Scottish Hydro. While the whole system is operated by System Operator (SO), National Grid.

A number of system scenarios with high penetration of PE are created using National Grid's forecast of future system inertia, representing various system inertia condition in 2020 and 2025. For the same reason, the PE-interfaced RES is modelled as simplified PQ power sources.

6.4 Hardware-In-the-Loop Testing Techniques

With all setups and configuration discussed so far, it is then important to discuss several methodologies which can be used to conduct the testing and validation using the testbed. HIL simulation is used to connect hardware systems and software models, and to place together them into a single closed-loop simulation. The benefit of HIL simulation techniques is they provide the rapid development of any part of a closed-loop system with a platform, whether based in hardware, or software.

For example, in an earlier work [88], A PV inverter controller as external hardware is tested using HIL for fast developing. In that case, a hardware controller was interfaced to the RTDS with power system simulated to form a closed loop. The obvious advantage is that we have been able to develop a hardware-implemented controller, while not having to be tested on physical inverter hardware. Of course, we can also have a PV controller simulated in Real Time Simulator (RTS) and interfaced with an actual inverter.

HIL technique is most employed to connect a hardware system, while no more preferred model exists, to a software model with well-known system. In the context of the smart grid, this could be a piece of newly developed equipment with advanced functionalities, and it is connected to a simulated local power system through a power amplifier interface. The hardware is utilised as it is not well-known, being newly established, while the power system is simulated as various good models of systems exist. This arrangement will allow the evaluation on the newly developed devices with the same conditions, that it would see if connected to the actual power system, while avoiding the risk of testing of an unknown

system.

As described, HIL simulation techniques can be leveraged in various different configurations for the development of many parts of a closed-loop system; Thus, the term HIL is used frequently for a wide variety of implementations, leading to more difficult to understand exactly how and if, HIL techniques are being used in a particular study. In this condition, this section will help clarify the issue by discussing the four most frequently used methods of employing HIL techniques, using common terminology.

6.4.1 RTS-based Simulation Only

Before conducting any HIL simulation, it is always the first step to simulate a model in real-time using the real time simulator even though it can not be formally called HIL as no external hardware is involved. However, the simulation performed is in real time instead of typical off-line computer based simulation.

While RTS based simulation could be just the first step of following HIL testing, it is sometimes used for fast validation of complication modeller which will take much more time if simulated on PCs. In this thesis, the RTS-based simulation is also referred to as CIL simulation or testing as the proposed Adaptive UFLS relays are modelled in RTDS and validated within the software loop. In [88] RTS simulation methods is used to purely accelerate the simulation speed as the authors developed a real-time model that approximates the electrical system on the Hawaiian island of Lanai in conjunction with a model of a large PV system.

6.4.2 Controller Hardware-In-the-Loop (CHIL)

Controller Hardware-in-the-Loop testing is usually conducted by interfacing an external hardware with controller under test implemented. The actual device being controlled is the model running on the RTS. This is the key advantage of the CHIL testing as new algorithms or physical controller can be evaluated using a simulated system or model running on the RTS without the requirement to interface real system.

The key advantages can be summarised as:

1. Algorithms or controllers can be developed, tested, and tuned in a very fast manner without the risk of damaging test system.

2. The simulated system or model can be readily modified and adjusted to the need of testing. For example, the future scenarios of GB test system is modelled in RTDS and it can be adjusted to test the proposed algorithm at different inertia level and loading conditions.

Another very common use of CHIL techniques is to test the response of digital power system protection relays with different abnormal system conditions simulated in RTS [89].

6.4.3 Power Hardware-In-the-Loop (PHIL)

PHIL simulation is a more recent technique that is to connect a software model to a hardware system that is operated at high power level. In PHIL testing, the RTS interfaces to the electrical output of the external devices via a power amplifier instead of low-voltage signal connections. The measured electrical output of the device under test is used as an input to the RTS model to close the loop.

The PHIL simulation technique is handy for device manufacturers as the product's performance can be readily tested to a wide variety of test system and configuration, allowing faster development of robust control algorithms.

6.5 Chapter Summary

This chapter has described the construction of a novel RTDS based testbed for proposed frequency control method providing high-fidelity simulation capability.

The necessity and benefit of conducting real-time closed-loop testing are discussed while the simulator and associated equipments of the testbed are briefly described.

Different methodologies of conducting real-time testing has been explained and suitable testing method will be used for the testing of the proposed method for UFLS and WAMPAC based fast frequency control method.

Chapter 7

Decentralised Adaptive Under Frequency Load Shedding Scheme

This chapter describes the creation of a novel algorithm for the accurate and reliable estimation of frequency and RoCoF of the CoI based on local measurements of frequency. With the input of the system inertia, an adaptive UFLS is designed. Section 7.2 defines the mathematical concept of estimation of CoI's RoCoF, while the design of corresponding UFLS is presented in Section 7.3. Section 7.4 describes the research performed to validate this method. The relative success of this algorithm is discussed in Section 7.5 as well as possible improvements.

7.1 Introduction

Modern electrical power systems are protected from large generator disconnection or system separation by Low Frequency Demand Shedding, commonly known as under frequency load shedding (UFLS) [10], [90]. Existing UFLS schemes have several predefined stages triggered by certain frequency thresholds, where each stage of shedding is deterministically designed in advance based on thorough system studies [19]. As the system inertia continues to drop and vary in the future [5], [74], [91], deterministically designed frequency control proves to be unsuitable, or even incapable, of offering efficient and secure protection in a future where an over shedding or breaching statutory frequency limit will be highly possible. To overcome this issue, many studies have focused on adaptively changing the amount of load shedding by using swing equation to calculate active power mismatch [19], [90].

Although, the electrical frequency is a global signal in steady state, when the system faces a severe frequency disturbance, frequency in the system will show individual behaviour. The difference of frequency depends on the local inertia and the electrical distance between the disturbance and the location where the frequency is measured [25], [92], [93]. Therefore, the Rate of Change of Frequency (RoCoF) seen at different locations varies, resulting in high deviation of RoCoF and estimated Loss of Generation (LoG).

A well-established communication infrastructure across the system, i.e. installing PMUs at every terminal of the generators can calculate the frequency of Center of Inertia (CoI) and its RoCoF in a control centre where the rotating speed and inertia of all generators are available through communication [41]–[43], [94]–[97]. In such a way, accurate LoG can be calculated. However, two reasons lead us not to go further with this approach. First, maintaining the reliability of communication is always a challenge. Secondly, a sophisticated communication system usually means that the LoG of the system can be directly obtained by knowing the disconnection of the generator and its power output before the event. UFLS action can then be taken based on this information instead of estimating it using RoCoF and inertia. For protection schemes such as UFLS, to achieving the most reliability, non-communication required solutions are preferred.

In this chapter, a method which estimates RoCoF of the CoI locally and a decentralised UFLS scheme using this technique are proposed. To estimate RoCoF of the CoI locally, an innovative algorithm referred as Inflection Point Detector (IPD) is used. The inflection point is defined as the points of the frequency where the second derivative of frequency crosses zero. By connecting those inflection points, the inter-area oscillation part of the locally measured frequency can be therefore cancelled. With two consecutive inflection points, an approximate RoCoF of the CoI can be calculated. To accomplish a UFLS strategy based on proposed IPD, it is necessary to have system inertia available. This is achievable as inertia estimation methods have been proposed by a number of researchers and paper [78], [98]–[100]. The requirement for the corresponding communication infrastructure to broadcast system inertia information is practically not difficult as there is no need for fast communication speed and the inertia information can be updated on a minute basis. With the available RoCoF of the CoI and system inertia, an adaptive UFLS strategy is then proposed which provides faster and more accurate response compared to conventional methods.

7.2 Principles and Challenges of Applying The Swing Equation To LoG Event Size Estimation

Knowing the size of an LoG event would be quite beneficial to improving frequency behaviour and preserving system stability. This enables UFLS relays to swiftly shed an appropriate amount of load to help retain active power balance. In this context, obtaining an approximate estimate of the event size immediately after its inception will be more helpful than an accurate estimation of the disturbance size after an unacceptably long delay. The sooner this size is estimated, the sooner an appropriate amount of load can be shed in order to arrest frequency decline.

According to (5-4), the per-unit swing equation of a synchronous generator on its own apparent power base is:

$$2H_i \frac{d\Delta f_i}{dt} = \Delta P_i \quad (7-1)$$

where H_i and Δf_i denote the inertia time constant and frequency deviation of the rotor of the generator i , respectively. ΔP_i is the difference between the mechanical and electrical power of the generator i . To come up with one swing equation describing system dynamics, the frequency of CoI is defined as below

$$f_{CoI} = \frac{\sum_{i=1}^N H_i f_i}{\sum_{i=1}^N H_i} \quad (7-2)$$

With some mathematical manipulations, one can derive the following swing equation

$$2H_{CoI} \frac{d\Delta f_{CoI}}{dt} = \Delta P_{CoI} \quad (7-3)$$

where

$$H_{CoI} = \frac{\sum_{i=1}^N H_i S_i}{\sum_{i=1}^N S_i}, \Delta P_{CoI} = \frac{\sum_{i=1}^N \Delta P_i S_i}{\sum_{i=1}^N S_i} \quad (7-4)$$

The above equation is commonly referred to as the CoI swing equation in per-units and proved advantageous in many different areas of power system studies. As already mentioned in section 5.3.1, we are neglecting the damping since we are only interested in the immediate moment after the event where the effect of damping can be safely disregarded. This equation relates the active power mismatch to the RoCoF right after an LoG event.

CoI frequency is essentially defined as a weighted average of the rotor speeds of generators, not frequencies measured at generator terminals. Therefore, to accurately estimate the CoI frequency, the internal voltage of each generator should be calculated. This may not be straightforward and introduces some errors due to the inaccuracy of generator parameters and their time-dependence. Alternatively, special metering equipment might be installed at each generator to directly measure the rotor speed, which might be demanding. Therefore, system operators prefer to measure the frequency of some pilot buses in the system instead of estimating the frequency of the CoI [19], [101]. Nonetheless, it is obvious that the frequency response of a pilot bus cannot represent the weighted average frequency of the whole system, but only the average frequency of synchronous machines in the near vicinity.

Theoretically, the CoI swing equation can be used to estimate the size of an LoG event. This can form a UFLS scheme followed by sending trip signals to some load blocks to compensate for the active power mismatch in the system. Practically speaking, there are two main challenges to adopt such a communication-based UFLS scheme. Firstly, if all generator terminals are equipped with PMUs, the tripped generators and the resulting active power mismatch can be directly determined without resorting to the CoI frequency. Secondly, basing system stability countermeasures fully on the communication network is not acceptable as a system-wide communication network is prone to latency and even total failure. A UFLS scheme based on such an approach may fail to determine the event size and operate in a timely manner.

7.3 Local Estimation of CoI RoCoF and LoG Event Size

Owing to the technical challenges described in the previous section, the calculation of the CoI frequency using communication infrastructure might not be a viable option. An innovative technique is presented here for estimating the CoI RoCoF using locally measured frequency, only. The provision of the CoI RoCoF makes it possible to develop an adaptive UFLS scheme for power systems with volatile inertia. This can effectively prevent frequency from declining to unacceptably low nadirs following large LoG events.

7.3.1 Local Estimation of the CoI RoCoF

Following an LoG event in the system, the frequency at different locations of the system starts declining. Frequency decays will not be uniform across the system, despite demonstrating a relatively similar trend and eventually converging to the same value after several seconds. Following an LoG event, frequencies at different locations oscillate around the CoI frequency, and the differences between them vanish over time.

Simulations show that when the second derivative of frequency with regard to time is positive, i.e. the frequency curve showing upward concaveness, its magnitude is smaller than the CoI frequency. On the contrary, when the second derivative of frequency with regard to time is negative, i.e., the frequency curve showing downward concaveness, its magnitude becomes larger than the CoI frequency. Between upward and downward concaved sections lie inflection points where the second derivative of frequency with regard to time changes sign. This forms the basis of Inflection Point Detector (IPD), which is used in this paper to pinpoint inflection points in real time. It can be inferred that the frequency curve at each location intersects the CoI frequency curve at around each inflection point. An approximate curve of the CoI frequency can be obtained by connecting these inflection points, and the CoI RoCoF can be calculated accordingly.

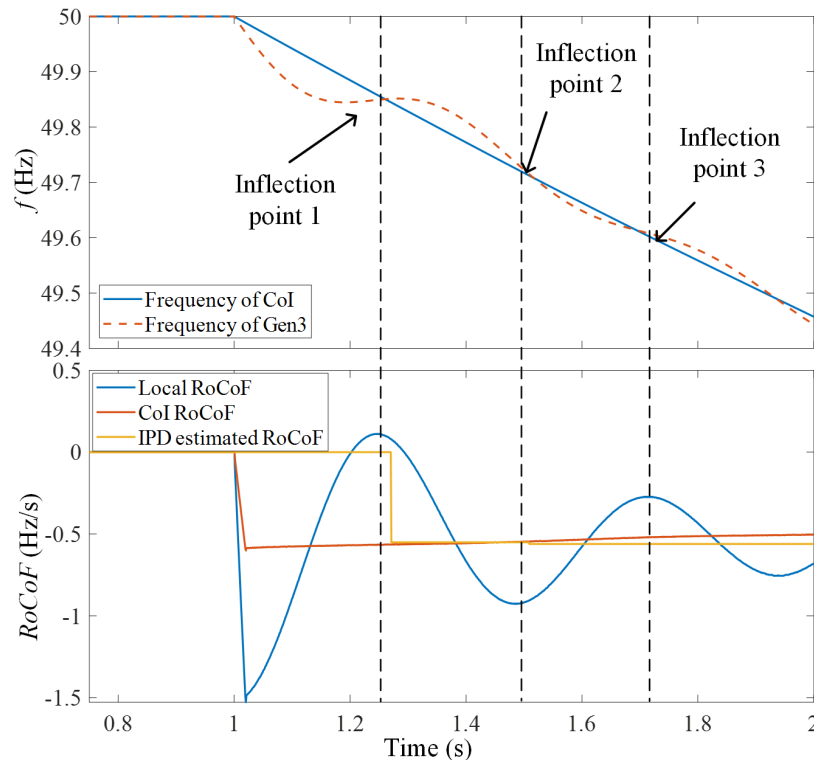


Figure 7-1: Frequency responses and inflection points.

To demonstrate the principles of the proposed IPD, an LoG event is simulated on the IEEE 39-bus system, and results are shown in Figure 7-1. Figure 7-1(a) illustrates the calculated CoI frequency and a locally measured frequency oscillating around the CoI frequency. The RoCoF of local frequency, the CoI RoCoF and the one estimated by using the proposed IPD method are shown in Figure 7-1(b). As can be seen, the estimation can be considered a good approximation of the CoI RoCoF after the first inflection point is detected. It can be observed that the local frequency curve intersects with the CoI frequency curve almost once the second derivative of local frequency with regard to time crosses zero. Let f_n and t_n denote the frequency and time instant of the n -th inflection point on the local frequency curve. Besides, f_0 and t_0 refer to the coordinates of the LoG inception instant. The IPD estimates the CoI RoCoF by

$$\frac{df_{CoI}}{dt} = \frac{f_n - f_{n-1}}{t_n - t_{n-1}} \quad (7-5)$$

For the first RoCoF, f_{N-1} is the pre-event steady state frequency and t_{N-1} is the time when under frequency event is detected.

Figure 7-2 shows the block diagram of the IPD technique used for estimating the CoI RoCoF using local frequency measurements, only.

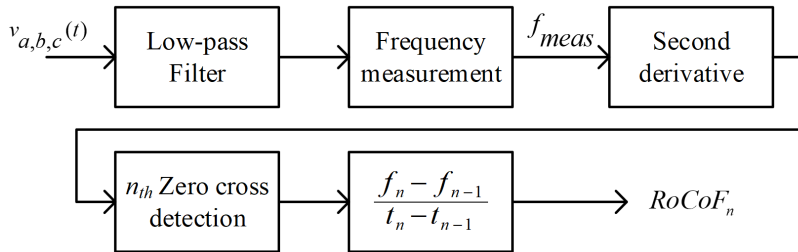


Figure 7-2: Diagram of Inflection Point Detector.

7.3.2 Proposed UFLS Scheme

Having calculated the CoI RoCoF as described, the LoG event size can be estimated using the swing equation provided that the system inertia is known. The question arising here is whether it is possible to conduct UFLS with no need of real-time communication between the control center and UFLS relays. To do so, a non-communication approach is needed to ensure the sum of load shed by different relays does amount to the active power deficit in the system. Let us assume that N substations are equipped with proposed UFLS relays. Let m_i^f denote the locally estimated CoI RoCoF at the location i . Let m_i^f also represent the slope

of the straight line between the point on the frequency curve at $t = 0^-$ and the first inflection point found on this curve. With the assumption that locally estimated CoI RoCoFs are good approximate of the true CoI RoCoF, one can write

$$m_1^f \simeq m_2^f \simeq \dots \simeq m_i^f \simeq m_{CoI}^f = \left. \frac{d\Delta f_{CoI}}{dt} \right|_{t=0^+} \quad (7-6)$$

As mentioned in section 7.1, system inertia is assumed to be available to the UFLS relay and is updated regularly enough, e.g., on a minute-by-minute basis. This means each relay can individually estimate the size of active power deficit as below

$$\Delta P_i^{est} = 2HS_{CoI}m_i^f \quad (7-7)$$

The superscript “est” in ΔP_i^{est} implies that this variable is the estimation of the active power loss by the relay at substation i . Each relay is set to shed the amount of load below

$$\Delta P_i = 2HS_{CoI}m_i^f \frac{P_{L,i}}{\Delta P_{total}} \quad (7-8)$$

where $P_{L,i}$ is the maximum amount of load allocated for load shedding at the location i and ΔP_{total} is the size of the largest credible contingency in the system. It can be easily confirmed that the sum of δP_i from all UFLS-enabled locations will amount to the estimated size of the LoG event.

It should be noted that due to the governor response of synchronous generators and the frequency dependency of load, it is not necessary to shed the exact amount of load as the LoG event size to retain a balance between generation and consumption. This can be considered by applying an adjustment factor β to the amount obtained in (7-7). Then (7-8) can be rewritten as

$$\Delta P_i = 2\beta HS_{CoI}m_i^f \frac{P_{L,i}}{\Delta P_{total}} \quad (7-9)$$

In this way, the required amount of load to be shed at each UFLS relay-equipped substation can be obtained.

It is assumed in (7-7) that the system inertia remains unchanged after the LoG event. This assumption holds true if the power mismatch is caused by the disconnection of HVDC interconnectors or PE-interfaced RES with negligible inertia contribution. However, if the LoG is caused by the trip of a synchronous generator, relying on the constant inertia assumption would lead to the overestimation of the LoG size [102]. To account for this and make the estimation more accurate, (7-7) can be rewritten as

$$\Delta P_i^{est} = 2HS_{post}m_i^{est,f} \quad (7-10)$$

Where $2HS_{post}$ denotes the post-event system inertia excluding the inertia of tripped generator

$$2HS_{pre} = 2HS_{post} + 2H_t S_t \quad (7-11)$$

Where H_t is the inertia constant of the tripped generator, S_t is the capacity of the tripped generator. Considering the power factor of tripped generator

$$S_t = P_t / PF \quad (7-12)$$

where P_t and PF are the active power output and power factor of tripped generator. Combining above equations

$$2HS_{pre} = 2HS_{post} + 2H_t P_t / PF \quad (7-13)$$

Then

$$2HS_{pre} = 2HS_{post} - 2H_t 2HS_{post} m_i^{est,f} / PF \quad (7-14)$$

Then (7-8) can be rewritten by replacing $H_{Col}S_{pre}$ by $H_{Col}S_{post}$, we can have

$$\Delta P_i^{est} = \frac{2HS_{pre}}{1 - 2H_t m_i^{est,f} / PF} m_i^{est,f} \quad (7-15)$$

It should be noted that in the case of an LoG event without inertia contribution, applying the proposed inertia compensation would cause underestimation of the LoG size. However, the advantage of applying the above inertia compensation outweighs this disadvantage as overshedding by the UFLS relays will be avoided in this way. Figure 7-3 compares the error between the true and estimated LoG size without applying inertia compensation. The inertia of the tripped generators, denoted by H_t , is varied between 0 to 6 seconds while its active power output is maintained constant. If the LoG size is relatively small compared to the whole generation of the system, the effect can be neglected. The estimation error increases as the disturbance size increases. The error of the estimated LoG size reaches 68.75 % when the disturbance size is 40 % of the whole system generation, and the inertia constant of the tripped generator is 6 sec. In all of the simulations carried out in the next section, a inertia of 3 sec has been assumed for the lost generation. This is to make a tradeoff between over- and under-estimation of the LoG size.

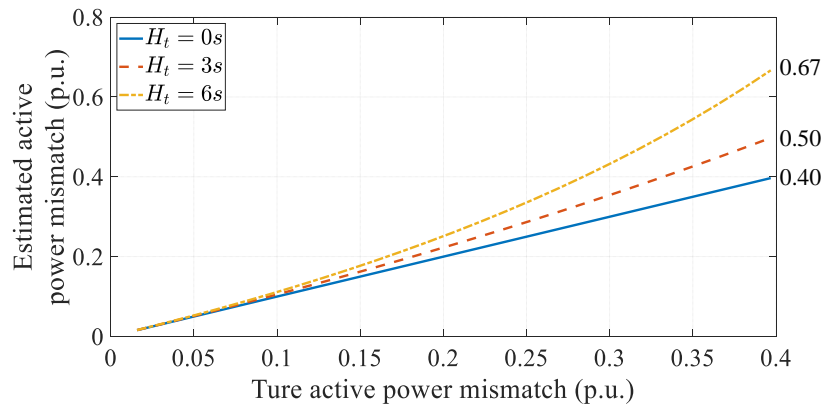


Figure 7-3: Comparison of estimated LoG for different inertia levels of the tripped generator.

7.4 Performance Evaluation

To study the performance of the proposed adaptive UFLS schemes, a number of simulations are carried out on the IEEE 39-bus system, also well known as 10-machine New-England Power System equipped with the proposed UFLS scheme. In this section, the performance of the proposed UFLS scheme is evaluated. Real Time Digital Simulator (RTDS) is used to conduct an extensive number of simulations. A diagram of IEEE 39-bus system is given in Figure 7-4. The test systems are modelled using RSCAD and then loaded on RTDS, which runs at real time with $65\mu s$ time-step. UFLS relays are modelled using RSCAD and loaded on another RTDS rack. The test system and relay racks are connected to each other with internal communication links, providing the relays with three-phase voltage waveforms of the load terminal, and connecting the relays to the associated load of the test system.

Non-synchronous power generators are implemented and placed at every generator terminal and replace the portion of the synchronous generators uniformly. By doing so, scenarios of different inertia level of the system are formed, and the system frequency response in different test scenarios can then be obtained and analysed. The obtained results are used to evaluate the effectiveness of the proposed UFLS scheme and compare it with that of the conventional scheme. The frequency of CoI is used to represent the average frequency response of the entire system. It should be noted that since this study only focuses on the primary frequency control, the final frequency after load shedding does not return to 50 Hz.

A four-step conventional UFLS scheme is set based on the systematic approach presented in [103]. The conventional scheme involves four steps, which conforms to the typical number of steps for many countries, as noted in the grid codes [104].

Table 7-1: Specifications of the IEEE 39-bus system in different scenarios.

Scenario	System inertia		System capacity (MVA)
	MVA.s	Sec	
Base case	78000	12.4	6300
25% PE case	58500	9.26	6300
50% PE case	39000	6.20	6300
75% PE case	19500	3.10	6300

An important point to note here is that FFR is not modelled and considered in this study. Even though FFR has been attracting a lot of attention in the recent power system research, it is vital to point out that the method presented in this chapter is focusing on an improved UFLS scheme which has a different operation principle and triggered at a lower frequency threshold. Therefore, FFR is not considered to be included in this study.

7.4.1 Test System and Relays Settings

The IEEE 39-bus system with a total load capacity of 6087 MW and 2781 MVA_r is used to test the performance of the proposed and conventional UFLS schemes in terms of system frequency response following LoG events. The nominal frequency of this system is modified to be 50 Hz. A dynamic PQ source model is used to represent large PE-interfaced RESs. These RESs are added to all generator buses, and the RES penetration level is varied by replacing different portions of the conventional generation with the same size of dynamic PQ sources. To create under frequency conditions for testing the UFLS schemes, generators of different sizes are tripped.

Four versions of the IEEE 39-bus system in RTDS are used to represent the system in future scenarios with different inertia and RES penetration levels. Table 7-1 lists the information of each scenario in terms of system capacity and inertia. The test systems corresponding to these scenarios are called base-case, 25 % RES case, 50 % RES case and 75 % RES case, respectively. The base-case scenario represents the default scenario with the most substantial inertia, i.e., 12.4 sec. The UFLS relays are placed at one-third of the load buses.

The proposed UFLS relays are set to operate and shed an appropriate amount of load once local frequency measured by them falls below 49.5 Hz. A four-stage conventional

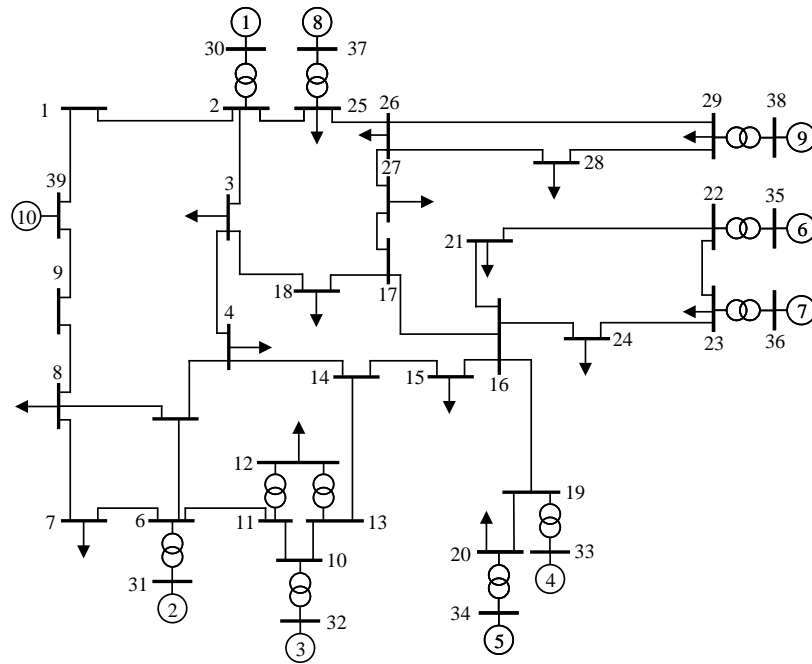


Figure 7-4: IEEE 39-bus test system.

UFLS is implemented in this section which will disconnect 7.5 % system demand at 49.2, 48.8, 48.6 and 48.4 Hz respectively. A 150 ms delay is added representing the operation delay of circuit breaker. This enables us to compare the performances of the proposed and conventional UFLS schemes following similar LoG events. The settings of the conventional scheme are obtained based on existing grid code guidelines and common practice [103], [104]. Thanks to the early estimation of LoG size, the proposed scheme is able to quickly activate the UFLS process compared to the conventional scheme, without risking reliability. Therefore, the single frequency threshold of the proposed scheme is set higher than all frequency thresholds of the conventional UFLS scheme.

It is well established that frequency might become distorted over a transient period following LoG events. This makes it quite challenging to reliably identify the inflection points of the frequency curve. Therefore, a blocking period of 500 ms is applied here before seeking the first inflection point. Simulations conducted show that the performance of the proposed scheme is improved accordingly with no risk of violating statutory frequency limits. System inertia is assumed to be estimated with respect to the committed synchronous generators in the system and fed to the UFLS relays regularly enough via non-real-time communication media. The scheme is expected to counteract active power deficit through this single stage of load shedding. From a practical point of view, however, it would be helpful to still maintain the conventional UFLS scheme in service. This might help to account for

large LoG events or cascading failures following which the proposed UFLS scheme might not act effectively/fast enough.

Table 7-2: Specifications of conventional UFLS settings.

Stages	Category	Threshold	Size
1	Conventional	49.2	7.5%
2	Conventional	48.8	7.5%
3	Conventional	48.6	7.5%
4	Conventional	48.2	7.5%

7.4.2 Accuracy of Local RoCoF Estimation

To study the accuracy of the technique put forward for estimating the CoI RoCoF by local frequency measurements, all 29 non-generator buses are equipped with the proposed UFLS relay. A total of 105 LoG events are simulated at different locations with sizes ranging from 250 MW to 1250 MW in 50 MW steps. In total, 3045 RoCoF estimations are acquired and presented in Figure 7-5 with a normal distribution fitting curve. 88.2 % of all RoCoF estimated are within 5 % deviation of the CoI RoCoF, which proved the robustness of the proposed IPD technique. It should also be noted that the mean of all RoCoF errors is -1.94 %, and the standard deviation is 3.01 %.

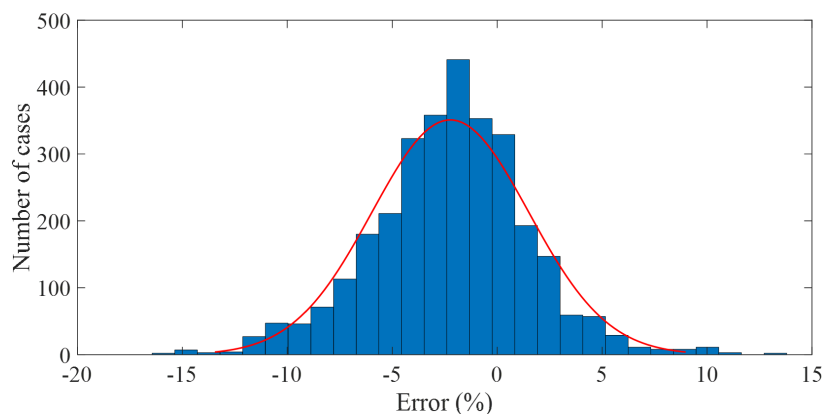


Figure 7-5: The distribution of the RoCoF estimation error.

7.4.3 General Evaluation of the Proposed UFLS Scheme

The general performance of the proposed UFLS scheme is studied in this subsection for a wide range of LoG events in different system scenarios. A heavy loading scenario is

assumed with a 1500 MW load increase. Additional generating units with a total generation of 1500 MW output are placed at bus 18. The outage of generating units below 600 MW at this bus will not activate the UFLS scheme as frequency deviation will not violate the 49.5 Hz threshold. Four larger outage cases, corresponding to 600, 800, 1000 and 1200 MW, makes frequency violate the 49.5 Hz frequency threshold. To demonstrate the performance of the UFLS scheme following these four LoG events, the CoI frequency following each event is calculated using (7-2) and shown in Figure 7-6. It is observed that the UFLS scheme is triggered, and the frequency deviation is arrested in all cases. The first inflection point is detected around 600 ms after the LoG inception in all cases. The frequency nadir remains slightly below 49.5 Hz as the whole generation deficit is compensated for at once as soon as the threshold is violated.

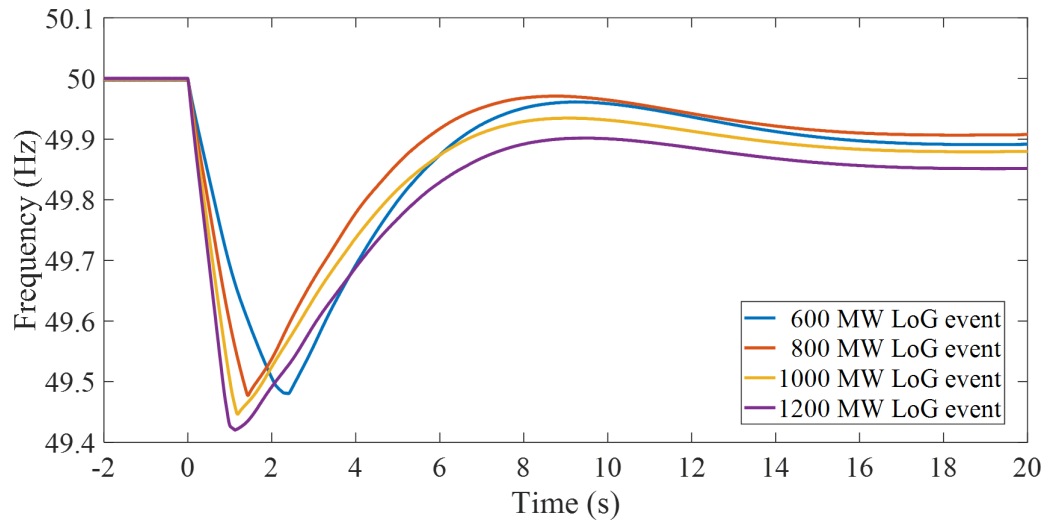


Figure 7-6: The frequency response of the proposed UFLS scheme following LoG events of different size.

The average relative errors of the estimated RoCoF in each simulated case is calculated as below

$$\text{Average Relative error} = \frac{1}{N} \sum_{i=1}^N \frac{|RoCoF_{CoI} - m_i^f|}{RoCoF_{CoI}} \quad (7-16)$$

where the $RoCoF_{CoI}$ stands for the true RoCoF of the CoI and m_i^f is the estimated RoCoF by the relay i and N is the number of UFLS relays in the system. Table 7-3 summarizes the true and estimated LoG size and CoI RoCoF in each case. As can be seen, the estimations are quite acceptable from a practical point of view with marginal errors. The estimation error for CoI RoCoF in all cases are less than 2%. It is also noted that the estimated LoG size is smaller than the true size. This mismatch is related to the inertial response of generators and

Table 7-3: Performance of the proposed UFLS scheme.

LoG Size (MW)		Load Shed (MW)	RoCoF (Hz/s)		RoCoF Est. Error (%)
True	Estimated		True	Estimated	
600	498.8	-416.5	-0.316	-0.319	0.97%
800	644.5	-642.2	-0.415	-0.412	-0.72%
1000	790.4	-787.7	-0.512	-0.505	-1.39%
1200	936.2	-933.0	-0.604	-0.598	-1.02%

also the effect of voltage depression immediately after the event. In fact, the estimated LoG size is accurately reflecting the true active power deficit. Table 7-4 shows the time instants at which the UFLS relays accomplish their duty and disconnect the corresponding load. In the case of 600-MW LoG, it is seen that not all relays perform load shedding as the relays operate in a distributed mode and will not trigger if the load shedding of other relays makes frequency recover.

Table 7-4: UFLS triggering instants by different relays.

LoG Size	600 MW	800 MW	1000 MW	1200 MW
Relay 1	2.36 s	1.38 s	1.14 s	0.95 s
Relay 2	2.37 s	1.38 s	1.13 s	0.95 s
Relay 3	2.23 s	1.38 s	1.13 s	0.94 s
Relay 4	2.38 s	1.39 s	1.14 s	0.97 s
Relay 5	0.00 s	1.38 s	1.15 s	1.09 s
Relay 6	2.05 s	1.40 s	1.02 s	0.84 s

7.4.4 Sensitivity to Various Factors

The sensitivity of the proposed UFLS scheme to penetration level is investigated in this subsection. The performances of the proposed and conventional UFLS schemes are compared for all simulated cases carried out on the modified IEEE 39-bus system. To evaluate the UFLS performance from different perspectives, a wide range of contingency sizes is considered by disconnecting a set of generators whose total active power output amounts to 5 % to 25 % of the total generation in the system. For each specific contingency size, multiple possible cases are studied to ensure the obtained results are valid.

Figure 7-7 demonstrates the frequency response following a 1000-MW LoG event. The solid and dashed lines represent the results obtained with the proposed and the conventional UFLS schemes, respectively. As can be seen, the proposed adaptive UFLS scheme would

more effectively contain the frequency nadir close to nominal frequency thanks to its ability to estimate the true LoG size, fast and accurately. Table IV summarizes the results of RoCoF estimation for different RES penetration levels. It can be observed that the average relative error does not exceed nine percent in different penetration levels, confirming that the accuracy of the proposed technique is quite promising from a practical point of view.

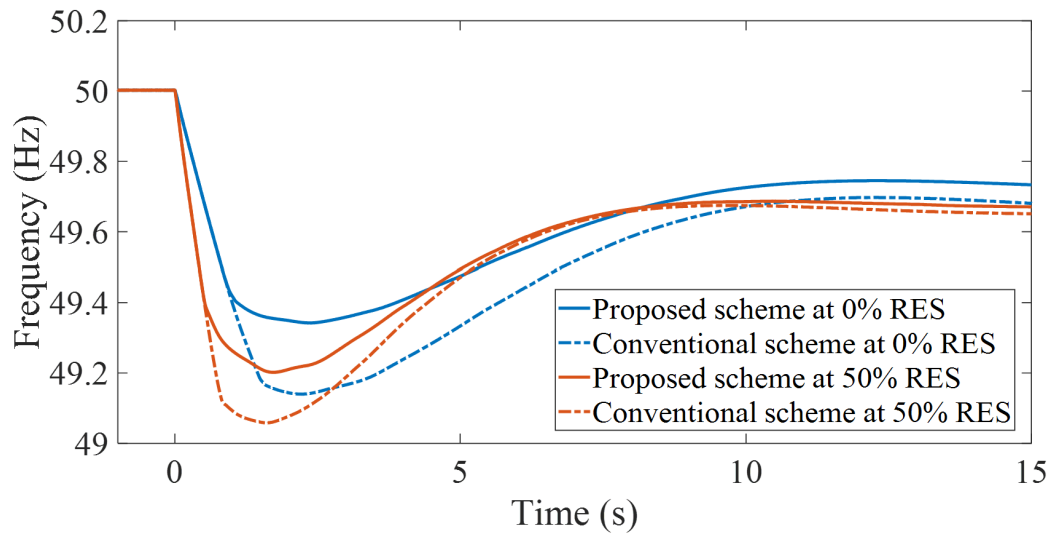


Figure 7-7: The frequency response of the proposed UFLS scheme following LoG events of different size.

Table 7-5 provides frequency nadirs for LoG events of size ranging from 1000 MW to 1800 MW. As can be seen, the nadir by the proposed scheme does not fall as much as that by the conventional UFLS scheme irrespective of the RES penetration level. This is because of the quick estimation of the event size and implementation of the UFLS at once by the former. On the other hand, the amounts of load shed by the proposed UFLS scheme remains constant regardless of the RES penetration level and the system inertia. However, simulation results show that the conventional UFLS scheme tends to shed more load following an LoG event of a fixed size if the system inertia decreases. This emanates from the fixed margins between the frequency thresholds of the conventional UFLS scheme. Indeed, for larger RES penetration levels, frequency drops much faster and is likely to violate a greater number of frequency thresholds. This will result in more load shedding and even overshedding in systems with highly reduced inertia.

Table 7-5: Frequency nadirs for different RES penetration levels.

LoG Event Size (MW)	Base-Case		25% RES		50% RES		75% RES	
	Prop.	Conv.	Prop.	Conv.	Prop.	Conv.	Prop.	Conv.
	Frequency Nadir (Hz)							
1000	49.42	49.17	49.39	49.18	49.31	49.16	49.21	49.10
1200	49.34	49.14	49.29	49.11	49.20	49.06	49.11	48.95
1400	49.26	48.97	49.20	48.90	49.09	48.81	49.03	48.81
1600	49.18	48.79	49.08	48.76	49.01	48.77	48.97	48.72
1800	49.06	48.76	48.92	48.75	48.85	48.68	48.79	48.55

7.4.5 An Adjustment Coefficient to Optimize UFLS Performance

The flexibility offered by the fast estimation of the LoG size using the proposed UFLS scheme is studied in this subsection. The amount of load shed by the conventional UFLS scheme is generally smaller than the LoG size. This essentially results from the multiple load shedding steps used by the conventional UFLS scheme. If frequency violates a frequency threshold but does not reach the next threshold, only the amount attributed to the violated threshold will be shed from the system. However, the proposed scheme is able to accurately estimate the size of the LoG event. This enables system operators to decide what portion of the lost active power needs to be compensated for by load shedding.

In practice, it might be desirable to limit the load shedding amount to a less-than-unity fraction of the LoG size. Many studies [42], [44] on adaptive UFLS have also deliberately reduced a certain portion of the estimated power mismatch to achieve a less amount of load to be shed. This can be easily realized in the proposed UFLS relays by multiplying the estimated LoG size by an adjustment coefficient. Special care should be taken to determine the adjustment coefficient as shedding less amount of load will certainly result in lower frequency nadir and final system frequency.

The performances of the proposed UFLS scheme with different adjustment coefficients and the conventional UFLS scheme are compared here. This comparison is made in terms of frequency nadir reached and the total amount of load shed. To this end, the IEEE 39-bus system with 50 % RES penetration is chosen as the test system. The sizes of LoG events are varied from 1000 MW to 1800 MW, and the frequency behavior is recorded for adjustment coefficients ranging from 0 to 1 pu. Figure 7-8 provides the average of important behavioral indices of simulation results obtained. As can be seen, without any adjustment ($\beta=1$) the frequency nadir by the proposed scheme will be located 0.25 Hz higher than that with the

conventional scheme. This is achieved by shedding the same amount of load as the LoG event size.

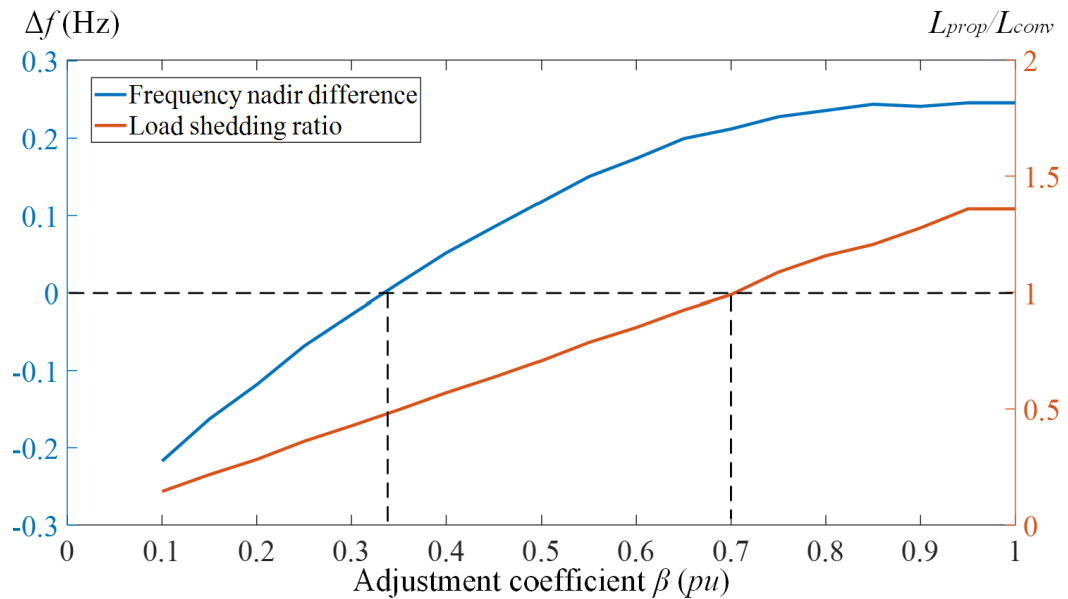


Figure 7-8: The frequency response of the proposed UFLS scheme following LoG events of different size.

By decreasing the adjustment factor, the amount of load shed by the proposed method will decrease at the expense of reaching lower nadirs. When β is set to 0.7, the amount of load shed by the proposed scheme will be fairly equal to that by the conventional scheme, but with a higher nadir. The reason is that the load shedding process by the proposed scheme is done at once as soon as frequency falls below 49.5 Hz, while this is done in several steps using the conventional scheme. Further reducing β gives rise to both higher frequency nadirs and less amount of load shed by the proposed scheme compared to the conventional one, which clearly confirms the superiority of the former. This is the case up until $\beta=0.34$ for which the nadir with both schemes will be the same, while the amount of load shed by the proposed scheme is less than 50 % of that by the conventional one.

Figure 7-9 demonstrates the frequency response of the system for a 1000-MW LoG event using the proposed UFLS scheme and compared it with that of the conventional schemes. As explained, when β is set to 0.7 pu, the proposed scheme will shed the same amount of load as that by the conventional scheme. In this case, the frequency deviation is arrested by the proposed scheme at around 0.21 Hz higher than using the conventional UFLS scheme. The figure also shows how the same nadir would be achieved by the proposed scheme by setting β to 0.35 pu only by shedding less than 50 % of the load shed by the conventional

scheme. In this case, the time to reach nadir is increased, which gives the opportunity for primary and secondary control mechanisms to return the frequency within an acceptable range in due time. In brief, the proposed scheme can provide higher frequency nadirs than that with conventional UFLS scheme, with equal or even less amount of load shed.

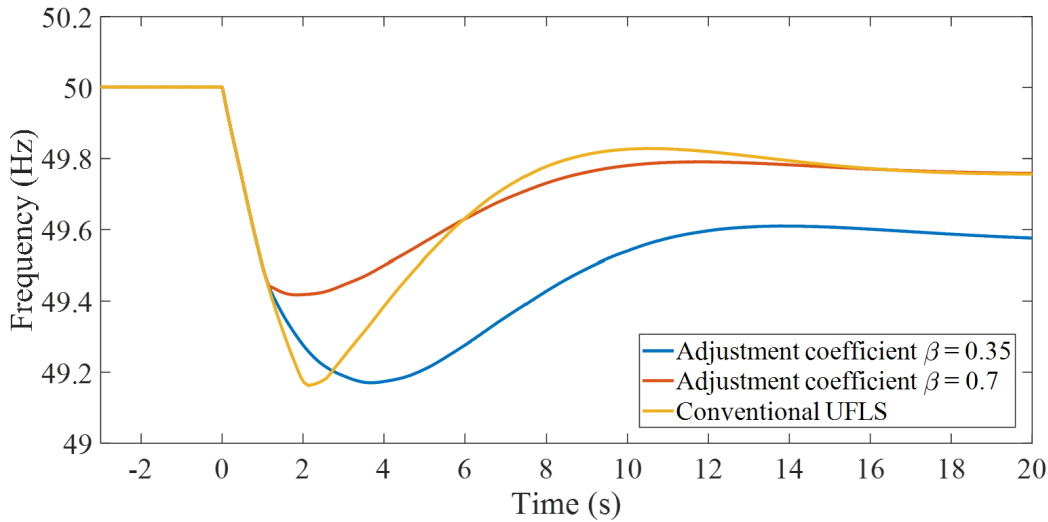


Figure 7-9: The frequency response of the proposed UFLS scheme following LoG events of different size.

7.5 Validation in the GB Test System

In this section, the proposed adaptive UFLS scheme is tested on a model of the GB transmission network, which is a practical example of a large AC power system. The dynamic model of the GB test system was adopted from National Grid's 36-zone model in DIGSILENT PowerFactory for this study. The dynamic model of the system used for this study included all components in the power system. This extends the extensive tests carried out on the modified IEEE 39-bus test system as the GB transmission network is an isolated system with a few interconnectors to the external grid, predicted to encounter low inertia problem in the future.

The network is converted into RTDS, shown in Figure 7-10, with a reduced number of zones (compared to the 36 zones), allowing the incorporation of more complex resource models. Each zone will have a different generation mix and certain significant resources (e.g. large offshore wind farms or new nuclear plants) will appear as distinct entities connected to sub networks within the zone. By this, the GB test system model consists of

a total of 26 busbars, 20 synchronous generators and 25 asynchronously connected generations (inverter-based generation) with 26 lumped loads. The nominal voltage of transmission lines is 400 kV, in this network.

In this case, eight designed UFLS relays are implemented at heavy loading busbars across the system, as shown in Table 7-6 and marked in Figure 7-10.

Table 7-6: UFLS relay placement in GB test system.

Region	Zone
South	1,2,8,9
North	13,15,20,23

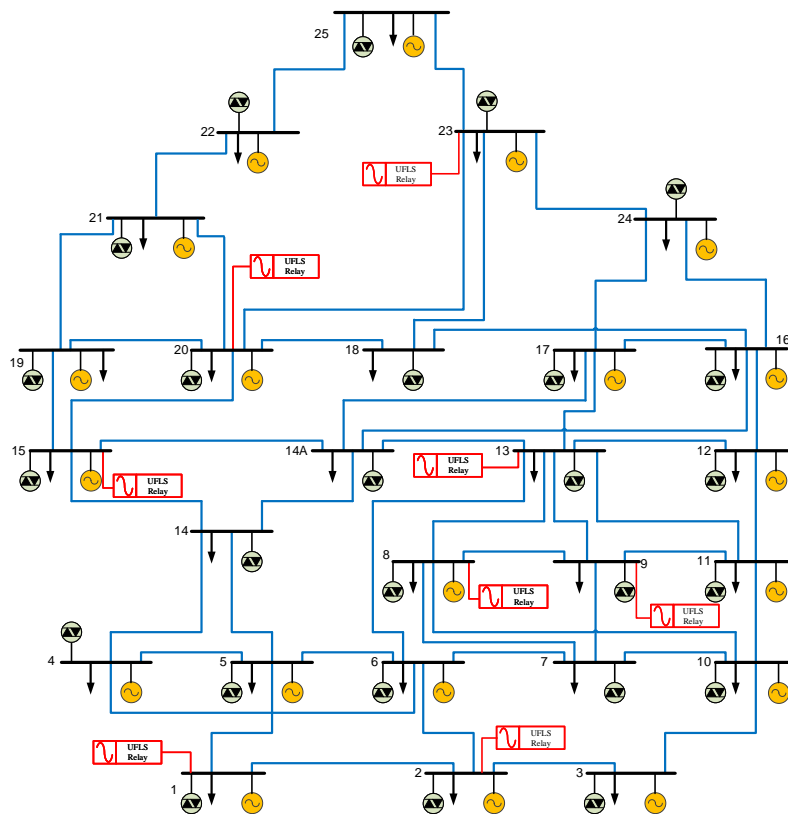


Figure 7-10: Single-line diagram of GB test system in RTDS.

The inertia level is 80 GVA.s presenting a system inertia predication in year 2020-2025 and the total system demand is 38 GW. 43% of the demand is supplied with non-synchronous generation and modelled as PQ sources.

The setting of proposed adaptive relay remains the same as it is designed to accommodate different system inertia level. The conventional UFLS relay is given in Table 7-7. For

practice in real system, simulation results are presented in absolute value instead of in per unit in the previous section.

Table 7-7: Specifications of conventional UFLS settings in GB test system.

Stages	Category	Threshold	Size
1	Conventional	49.2	1200 MW
2	Conventional	48.8	1200 MW
3	Conventional	48.6	1800 MW
4	Conventional	48.2	1800 MW

The performance of the conventional and proposed UFLS schemes are presented in Table 7-8 and Table 7-9. It is noted the proposed one-stage UFLS scheme can effectively estimate RoCoF with high accuracy and respond proportionally to the event size. The frequency nadir is considerably improved especially. The performance of RoCoF estimation by the proposed method is also included in Table 7-8 which again valid the effectiveness of proposed RoCoF estimation method and adaptive UFLS scheme.

Table 7-8: Performance of proposed UFLS scheme in GB test system.

Event Size (MW)	Freq Nadir (Hz)	Final Freq (Hz)	Freq Recovery (Sec)	Load Shed (MW)	Estimated RoCoF (Hz/s)	Max Relative Error (%)	Ave Relative Error (%)
1500	49.36	49.97	16.20	999	-0.31	2.05	1.38
1500	49.36	49.97	16.21	981	-0.30	1.72	0.87
2000	49.22	49.94	17.40	1315	-0.41	3.18	2.22
2000	49.23	49.94	16.90	1321	-0.41	3.48	1.93
2500	49.11	49.93	17.62	1714	-0.53	6.67	2.54
2500	49.08	49.93	17.92	1682	-0.52	8.69	4.57
3000	48.96	49.91	18.46	2070	-0.64	3.34	1.87
3000	48.98	49.92	18.31	2128	-0.66	2.90	1.81
3500	48.83	49.90	18.62	2450	-0.76	4.65	2.88
3500	48.85	49.90	18.32	2483	-0.77	4.01	2.27
3500	48.78	49.89	18.77	2431	-0.75	8.83	5.08
4000	48.73	49.89	18.24	2908	-0.90	5.45	3.88

7.6 Chapter Summary

This chapter has demonstrated a method that allows the accurate estimation of CoI's RoCoF without communication system and, therefore, the accurate estimation of LoG and to shed

Table 7-9: Performance of conventional UFLS scheme in GB test system.

Event Size (MW)	Freq Nadir (Hz)	Final Freq (Hz)	Freq Recovery (s)	Load Shed (MW)
1500	49.14	50.02	12.79	1200
1500	49.14	50.03	12.61	1200
2000	49.00	49.95	16.89	1200
2000	49.00	49.95	16.90	1200
2500	49.01	49.94	16.45	1200
2500	48.68	50.14	11.18	2400
3000	48.68	50.14	11.18	2400
3000	48.63	50.01	13.52	2400
3500	48.63	50.01	13.71	2400
3500	48.48	49.93	16.42	2400
3500	48.48	49.92	16.31	2400
4000	48.47	49.92	16.53	4200

the proper amount of load using the proposed adaptive UFLS scheme.

Traditional UFLS schemes operate when measured frequency falls below the predefined thresholds and shed predefined amounts of loads in multiple steps. Such a scheme is expected to experience over shedding issues when a fixed set of settings is used in another system with higher renewable integration.

Unlike the traditional method, the newly proposed UFLS scheme utilises local frequency measurement to estimate the RoCoF of the CoI of the system and adaptively change the size of load shedding. The inflection points on frequency curves are exploited to be used to estimate the CoI frequency and calculate an approximation of the RoCoF of the CoI.

Performance of the proposed UFLS scheme is assessed using both IEEE 39-bus test system and GB test system. The obtained results have shown that the proposed method can adequately protect the system from frequency instability. The estimation of RoCoF is accurate, thus can successfully reflect the actual disturbance size and decide the amount of load shedding. Compared with conventional UFLS scheme, the proposed method can achieve better performance in terms of higher nadir and correct load shedding amount.

Additionally, an algorithm to compensate for the reduction of the system inertia due to generator tripping is created, the post-event system inertia can then be corrected to produce a more accurate LoG estimation.

Chapter 8

Fast Frequency Response using Wide Area Monitoring and Control System

This chapter describes a novel wide area monitoring and control scheme for fast frequency response and its validation using HIL testing. The background of the method is discussed in Section 8.1. Section 8.2 presents the concept of the scheme, and the validation methodology is provided in Section 8.3. Section 8.4 presented the result of the performance assessment of the scheme. The conclusion is given in Section 8.5.

8.1 Chapter Introduction

This chapter presents the design and performance of the Enhanced Frequency Control Capability (EFCC) scheme, using representation model of the future lower-inertia GB system simulated by the proposed RTDS testbed, as described in chapter 6. In section 4.3, the importance of FFR in future power systems and the feasibility for FFR to be achieved using a range of technologies has been discussed. However, the key shortcoming and gap of the existing work is that they only focus on a specific technology or type of energy source without the consideration of the optimised coordination of different resources, which could have significantly different characteristics and capabilities in providing frequency support. Furthermore, the existing work has very limited consideration of the regional impact of frequency events. In [8], the regional impact of frequency events was considered, but again only one specific resource was investigated without consideration of contribution from or coordination with other FFR providers.

It can be seen from the literature review that, while the need for FFR in systems with low inertia has been widely recognized, the following issues still remain unresolved: 1) the locational impact of FFR has not been fully considered, where frequency stability has been addressed as an independent issue from rotor angle stability and the risks of accelerating frequency control using local measurements has not been recognized; 2) the coordination of responses from different resources has not been considered when deploying the FFR from different resources with different characteristics and capability, which leads to the overall response not being optimal in performance; and 3) the need for monitoring of the status and capability of resources providing frequency response is not well recognized, which could result in the mismatch between the expected response and the actual power delivered by renewable generation.

The focus of the chapter is to assess the performance of proposed scheme and to report its success or issues across a series of defined tests of typical power system disturbance conditions. The RTDS simulation environment has been dispatched to capture typical future transmission system performance against scenarios as defined within National Grid's Future Energy Scenarios (FES). It should be noted that the design of the scheme is conducted by GE which is part of the EFCC project [59], [105]¹. The novelty of this chapter is the testing and validation methodology and the analysis of testing result for such a very first WAMPAC scheme of its kind in the world.

8.2 Monitoring and Control Scheme

This section presents the design of the novel Wide Area Monitoring Protection and Control (WAMPAC) system, termed "Enhanced Frequency Control Capability (EFCC)". The presented scheme addresses the aforementioned challenges of frequency control and the need for faster frequency response with consideration of the regional impact of events and the coordination of a range of different resources for responding on a localised basis.

The scheme uses real-time data from PMUs installed at both transmission and distribution levels for monitoring the network and determining the required responses. The system takes into account the impact of the frequency event on different parts of the network and

¹The description of the proposed the scheme has been published in the paper Q. Hong, M. Karimi, M. Sun et al., "Design and Validation of a Wide Area Monitoring and Control System for Fast Frequency Response," vol. 11, no. 4, pp. 3394–3404, 2020. © 2020 IEEE

allocates responses at a regional level. The characteristics and capabilities of different connected resources are considered, so that a coordinated and optimised response is dispatched during and immediately following the event, thereby providing effective and enhanced frequency control for low-inertia power systems.

8.2.1 Overview of the EFCC Scheme

The EFCC scheme has been designed with the following high-level requirements to address the challenges brought by the lower system inertia:

- Bound total response magnitude to predictably limit over/under response to events;
- The response must be within 500 ms of event initiation;
- Minimise the impact of control actions on the transient stability of the network;
- Maximise utilisation of available resources;
- Be capable of dealing with communications performance issues and failures in resource deployment.

The system uses a distributed control approach as indicated in [106], where the monitoring and control functions are executed using three functional elements: the Central Supervisor (CS), Local Controllers (LCs) and Regional Aggregators (RAs).

In Figure 8-1, the scheme is designed with two main data paths:

- One real-time “fast-communication” path for PMU measurements and command for resources.
- One near-real-time communication path for sharing resource information.

The CS monitors the capabilities and characteristics of resources in near-real-time scale (i.e. 1 s from status change). Based on the resource information, the CS identifies the optimal combination of resources to achieve the most desirable coordinated response, e.g. a short delay and high ramp-up capability with sufficient duration. The CS sends the optimisation results (in the form of a set of priority values and rankings for each resource) and system operating conditions (i.e. system inertia) to all LCs. This information is used by

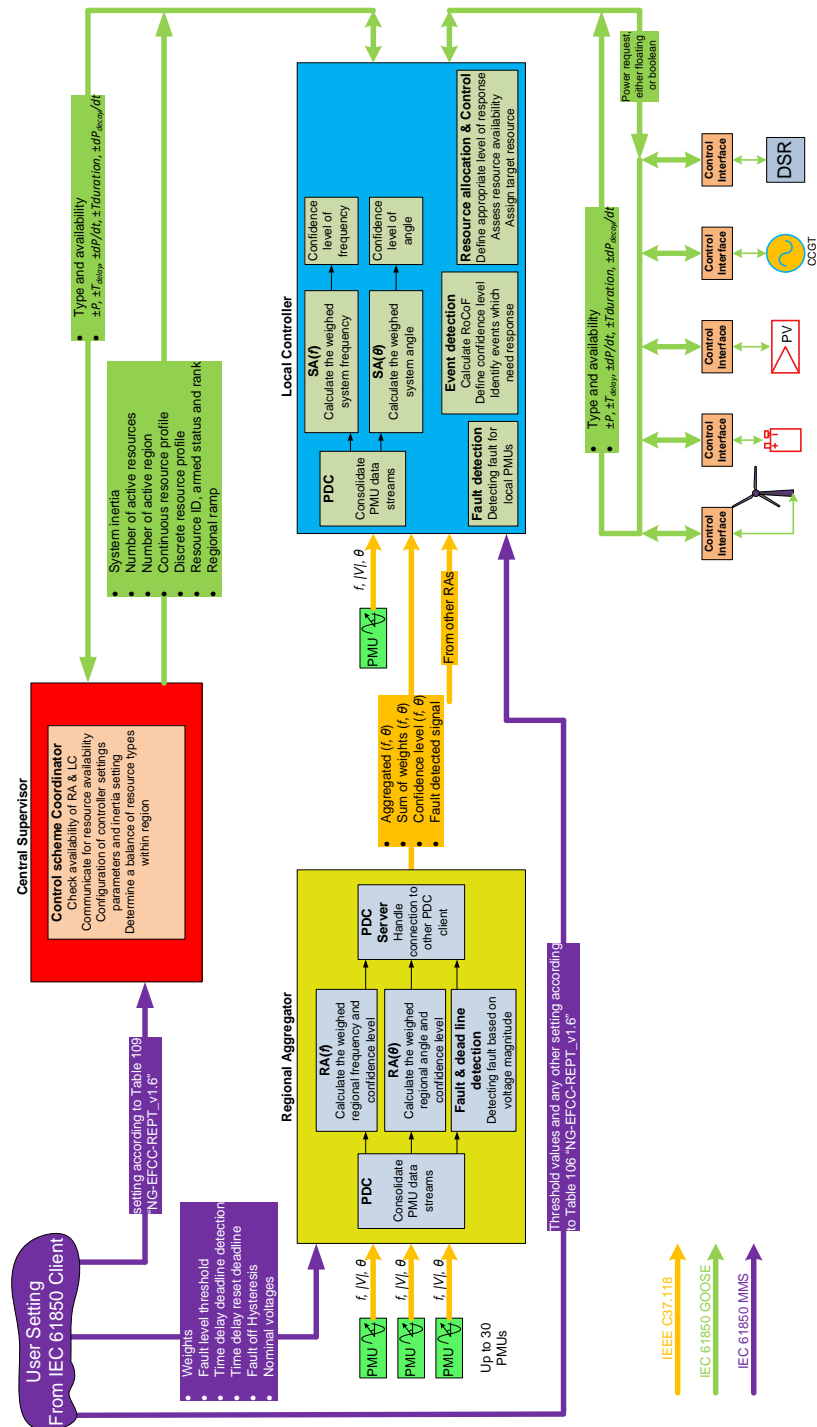


Figure 8-1: Schematic of the design of the EFCC scheme.

LC when calculating the required response from individual resources. This is discussed in Section 8.2.3 and 8.2.4.

For the fast-data measurements, the power system is divided into regions, where the boundaries would be formed based on suitable coherency studies [107]. Within each region, a number of PMUs are installed close to the dominant inertial sources in the region. PMU data in each region is collected by the RA, which perform aggregating algorithms to produce an equivalent frequency and angle value for its region. The outputs of the RAs are broadcast to all LCs, which perform real-time monitoring and control functions. The LCs are installed at the resource sites that provide the FFR service. Each resource is equipped with one LC and a local measurement device (typically a PMU), which acts as a backup in the event of loss of wide-area communications.

When a disturbance occurs, each of the distributed LCs detects the event based on the wide-area measurements or the local backup measurement. Each LC will then determine the overall response required for the event and from that, their individual contribution to the overall response. The contribution of the regions, and hence individual resources within the regions, is determined based on analysis of the wide-area phase angle movement as a result of the event. Deploying response with respect to the wide-area phase angle movement ensures minimal impact on the overall transient stability of the system. The selection of which particular resource to use within each region is based on the information received pre-event from the CS. Using the priority tables, resources are deployed according to their effectiveness in halting the frequency decline.

It should be noted that EFCC aims to deploy responses with a shorter time delay than conventional droop-based responses, thereby enhancing containment of frequency deviations. Droop control is of course still required in the system for frequency regulation. The design of each of the three main elements and the algorithms to achieve the associated functions are described in detail in the following sections.

8.2.2 Design of Regional Aggregators (RA)

An RA is installed in each region to collect and process PMU measurements and produce a regionally aggregated frequency and angle to represent the regional behaviour. Compared to a centralised control scheme, this has the benefit of reducing the amount of data sent from a

region. Also, it reduces the effect of local modes of oscillations in a region through the aggregating function. In order to represent a region's frequency, sufficient PMUs are required within the region to represent the inertial resources' frequency behaviours, and ensure that the effects of system reconfiguration/outage and resource unavailability do not significantly impact the accuracy of the overall measurement synthesis. A weighting factor (W_{Rn}^i) is assigned to each PMU measurement to reflect its observability of the surrounding inertia in the region. Clearly, in real-world applications, there are threats to data quality, measurement accuracy and communications systems integrity. Accordingly, quality handling is incorporated in all functions.

The regional equivalent frequency is calculated using (8-1):

$$f_{Rn} = \frac{\sum f_{Rn}^i \times W_{Rn}^i \times Q_{Rn}^i}{\sum f_{Rn}^i \times W_{Rn}^i} \quad (8-1)$$

where: Q_{Rn}^i is a quality metric derived for the measurement data based on elements such as communications quality and signal metadata such as defined by the IEEE C37.118.2 standard [108].

The regional aggregated angle θ_{Rn} is calculated using a similar method as shown in (8-2).

$$\theta_{Rn} = \frac{\sum \theta_{Rn}^i \times W_{Rn}^i \times Q_{Rn}^i}{\sum \theta_{Rn}^i \times W_{Rn}^i} \quad (8-2)$$

A confidence level of the region is defined to assess the quality and the availability of PMU data in the RA is calculated as shown below in (8-3):

$$C_{Rn} = \frac{\sum W_{Rn}^i \times Q_{Rn}^i}{\sum W_{Rn}^i} \quad (8-3)$$

In the LC, which processes the RA data, the confidence level C_{Rn} is used to determine if the signal from a particular region is of sufficient quality to be used by the scheme. If the confidence from that regions' calculation is too low, it will be excluded from calculations, however, this does not necessarily prevent the scheme from operating. A threshold for overall confidence of the whole system is used to decide whether WAMS is reliable enough to operate. If not, LC discards the wide area measurements and operates based on local measurement. This is part of the graceful degradation design of the scheme.

The output of an RA is a vector $R = [f_{Rn} \quad \theta_{Rn} \quad C_{Rn}]$, which will be used by LCs for detecting events and calculating the response required in each region.

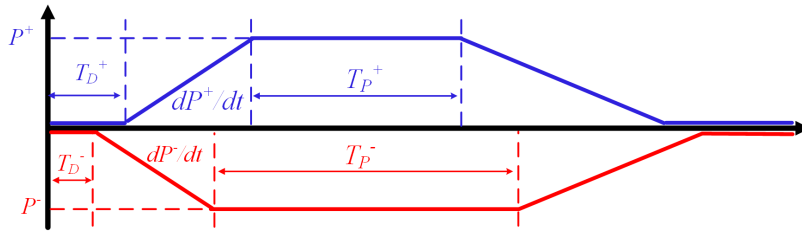


Figure 8-2: Response characteristics of resources

8.2.3 Design of Central Supervisor (CS)

The main task of the CS is to inform all LCs regarding the latest system condition (e.g. overall system inertia) and provide near-real time assessment and coordination of resources across the system. Based on the availability, capabilities and characteristics of the resources that can provide FFR, an optimisation process is performed by the CS to prioritise the available resources in terms of response speed and duration capabilities.

Each resource providing FFR is characterised as shown in Figure 8-2 using a number of parameters to describe its capability, e.g. P^+ and dP^+/dt describe the total amount of positive power and the ramp up rate of the positive active power respectively. The LCs will report such information to the CS periodically or whenever there is a change to the resource status. The CS will receive this information from all LCs and perform the optimisation function to assign resource priorities, i.e. ranking resources' frequency response effectiveness.

In this example of the optimisation algorithm, the priority value of a resource (ζ) is calculated based on the speed by which a resource can respond and the duration of that response. The response characteristics of resources are defined with an initial delay of T_D and average ramping rate dP/dt . From Figure 8-2, it can be seen that, the speed of response is associated with delay and ramp rate, i.e. T_D^+ and dP^+/dt for a positive response. Due to the variety of the resources and their different delay and ramp rate, it is challenging to directly compare different types of resources and prioritise them in the resource allocation process. Therefore, a pseudo ramp rate (\bar{P}), associated with delay and ramp rate, is defined to compare the response speed of different resources. The definition of pseudo ramp rates is illustrated in Figure 8-3. In this section, the positive response of a resource for under-frequency event is used as an example to explain the design of CS. The negative direction of response will follow the same principle.

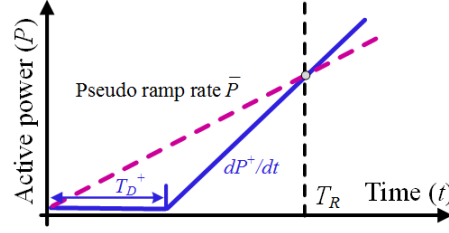


Figure 8-3: Definition of the pseudo ramp rate

Firstly, the resource profile can be expressed as (8-4):

$$P = \frac{dP^+}{dt} \times T_R - \frac{dP^+}{dt} \times T_D^+ \quad (8-4)$$

At a defined time T_R , the pseudo ramp rate \bar{P} can be calculated as (8-5):

$$\bar{P} = \frac{\frac{dP^+}{dt} \times T_R - \frac{dP^+}{dt} \times T_D^+}{T_R} \quad (8-5)$$

The value of T_R is configured based on the desired response window, i.e. 1-2s where it effectively represents the regional deployment of resources once triggering action has occurred, but also accounting for delays in the resource deployment.

Once the pseudo ramp rate is calculated, the priority of each resource may be obtained using (8-6):

$$\zeta_k = \alpha \frac{\bar{P}^k}{\max(\bar{P})} + \beta \frac{T_P^k}{\max(T_P)} \quad (8-6)$$

Where \bar{P}^k and T_P^k are the pseudo ramp rate and the power duration of the k^{th} resource in a region respectively, while $\max(\bar{P})$ and $\max(T_P)$ are the largest ramp rate and the longest duration for all resources within a region; α is the weighting of the positive/negative response rate; β is the weighting of positive/negative response duration. A relatively higher priority will be assigned to a resource with a faster response and/or longer duration capability compared to other resources. The weights α and β are configurable settings in the CS.

The calculated priority values (ζ_k) will be used to produce a ranking table for all the resources in the region. The ranking table is sent to the LCs, along with system information (e.g. system inertia, number of active regions and resources, etc.), which is used by the LCs to determine the nature and amount of their responses.

8.2.4 Design of Local Controller (LC)

The LCs are distributed controllers that are installed at (or close to) resource sites. LCs autonomously detect events and calculate the resource deployment based on real-time measurements from RAs and ranking information from the CS. There are a number of steps and function blocks involved in the decision-making process; these are described in detail in the following subsections.

System aggregation

The outputs from RAs contains information relating to regional behaviour, such as the effects of inter-area oscillations. To evaluate the system power imbalance from an event, the data from RAs is further aggregated using the same methodology as used in the RA, producing a system-wide equivalent frequency and angle using (8-7) and (8-8) respectively. This process is referred to as system aggregation and it is necessary for:

- Create a system signal from which to detect system events.
- Create the reference by which to compare each of the regions for the locational targeting of the control scheme.
- Provide a filtering effect for inter-area oscillations due to averaging between the oscillating regions.

The latter is important as it reduces the effects of inter-area oscillations on the performance of event detection and subsequent power imbalance calculations, each of which would otherwise be sensitive to the effects of these oscillations.

$$f_S = \frac{\sum f_{Rn} \times W_{Rn} \times Q_{Rn}}{f_{Rn} \times W_{Rn}} \quad (8-7)$$

$$\theta_S = \frac{\sum \theta_{Rn} \times W_{Rn} \times Q_{Rn}}{\theta_{Rn} \times W_{Rn}} \quad (8-8)$$

Event detection

The control scheme is only triggered when a frequency event is detected. The effects of local phenomena such as line trips, which will affect local frequency measurements, do not

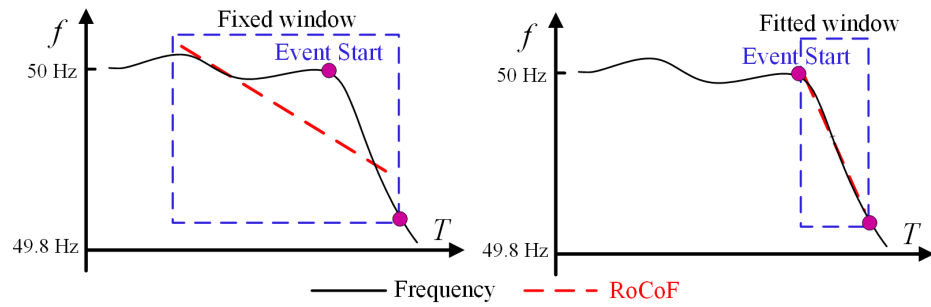


Figure 8-4: Comparison of detection window on RoCoF

trigger the scheme. The events are detected using a pre-defined RoCoF threshold. Conventional methods of calculating RoCoF from PMU measurements can lead to a long delay due to the averaging window used. For this scheme, a novel fast event detection algorithm is used, which limits the delays associated with fixed windowing methods. The approach uses a window-fitting approach to target the samples surrounding the frequency excursion. The detection window contains frequency values which are received every 20ms from the measurement devices. The detector employs multiple stages of detection for verification, and best-fit calculations to increase the accuracy of the detection method without unnecessary delay. There are a series of settings which allows user configuration and tuning of the behaviour of the detection algorithms, such as changing thresholds, adjusting sensitivity, etc. The algorithm is designed to “ride-through” gaps in data which may occur in wide-area networks, and remain operational when gaps are present.

The event detector algorithm will provide an event trigger but also a RoCoF calculation, where the event window method captures the event gradient more effectively than a fixed window approach as shown in Figure 8-4. Use of a smaller window allows faster detection, as the calculated RoCoF will violate the triggering threshold sooner, but also provides a faster assessment of the resultant system RoCoF due to the event.

Resource allocation

Once an event is detected, the LC must determine the amount of individual power contribution from the resource it is controlling, based on the scale of the detected event, the impact of the event on its region and the ranking information from the CS. This process is referred to as resource allocation. The event scale is estimated using the swing equation as shown in

(8-9) [109]:

$$\frac{2H_S \times S_{rated}}{\omega_{syn}} \times \omega_{pu} \times RoCoF_S = \Delta P \tag{8-9}$$

ΔP is the estimated total amount of power imbalance following a frequency disturbance. The system inertia H_s should be equivalent to the current inertia in the system, but this may be difficult to assess accurately, so the value used in the algorithm allows for error, using a self-correcting mechanism during deployment. When an event occurs, the LCs use the wide-area measurements to evaluate which regions are most affected by the disturbance, identifying the leading and lagging regions based on their individual angular acceleration.

A factor K_{Rn} is defined using (8-10):

$$K_{Rn} = \underbrace{\Delta\theta_{Rn}}_{\theta_{Rn}^- - \theta_{Rn}^+} - \underbrace{\Delta\theta_S}_{\theta_S^- - \theta_S^+} \tag{8-10}$$

Where, θ_S^- and θ_{Rn}^- are pre-event system and regional angle respectively, while θ_S^+ and θ_{Rn}^+ are system and regional angle at the time when the event is detected. The impact of an event on each region can therefore be quantified through the above analysis of angles deviation levels due to the event.

The total power imbalance is then allocated to the most affected regions, but biased initially towards the regions which are “leading” the event, i.e. ahead of the system frequency. By targeting control to these regions, the angular separation between the regions can be reduced, thus reducing the risk of transient instability or system splits. The amount of power, P_{Rm} , that a region requires to respond appropriately to the event can be calculated using (8-11).

$$P_{Rm} = \frac{K_{Rm}}{\sum_{j=1}^m K_{Rj}} \times \Delta P \tag{8-11}$$

Regions m represent the regions that are allowed to provide frequency response during the initial control period where the risk of instability is a concern.

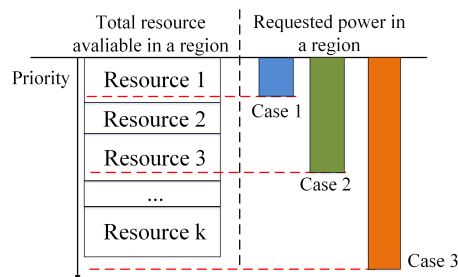


Figure 8-5: Examples of resource allocation within a region.

Once the effects of the event on the angular separation have passed, typically after the first swing following the event, the risk of applying resources without region bias is reduced. The scheme will then transition to a coordinated control stage, where additional resources from regions which were initially blocked can be utilized, i.e. regions not included in Regions m can begin to respond and contribute to the frequency response. This is particularly useful if there was insufficient resource available in the most affected regions. The chosen design principle maximizes the use of available resources without jeopardizing system stability.

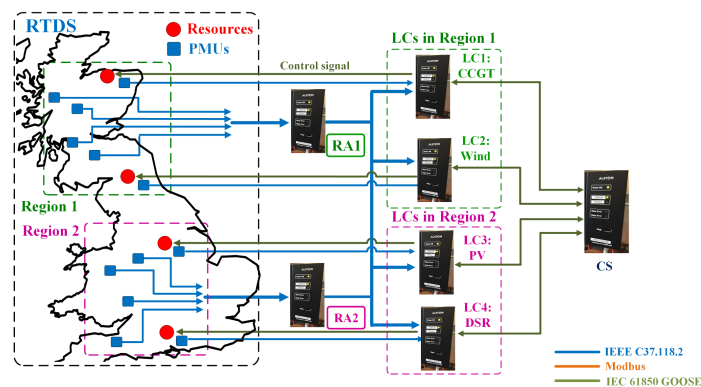


Figure 8-6: Test setup for validation of the EFCC scheme.

Within each region, there can be multiple resources controlled by multiple LCs. The responses from these resources are coordinated by their capability and characteristics so that the overall response is fast and of sufficient duration for handover to primary response. This is illustrated in Figure 8-5. The total requested power will be taken from the available power based on the priority, which is determined by the CS based on the resources' ramp rate and duration (as presented in Section 8.2.3). In case 1, resource 1 is sufficient to supply all the requested power and has the highest priority, so all requested power will be dispatched from resource 1. In case 2, the requested power is resource 1 and 2 will be fully dispatched while the remaining power will be taken from resource 3. If the requested power is greater than the available power, all the available power will be dispatched as shown in case 3.

8.3 Validation of the EFCC Scheme

In this section, the methods used for testing the EFCC scheme and the associated test results are presented to demonstrate the effectiveness of EFCC in enhancing frequency control in a

low-inertia system. The validation of the scheme has been performed in using Controller-Hardware-in-the-Loop (CHIL) approach. CHIL is suitable for applications where the interaction between simulation and the physical devices involves analogue and digital signals [110].

The main reason for testing the EFCC scheme using CHIL approach is that CHIL is more flexible and easier in the configuration of the network operating conditions, which allows a relatively large number of tests to be conducted with a lower cost and shorter period of time.

8.3.1 GB Test System Modelling in RTDS

This test uses a GB network test system that is designed to be representative of the GB system. The reduced number of zones (compared to the 36 zones) will allow the incorporation of more complex converter-based resource models, i.e. RES models. The reduced model of 36-zone GB network system is built and simulated in RTDS.

The modelled GB network test system consists of 20 synchronous generators and 25 asynchronously connected generations (converter-based generation) with 26 lumped loads is selected for the validation and HIL testing. The single line diagram of the test system is shown in Figure 8-7. In this model, four different types of service providers are modelled and integrated. Photovoltaic (PV), Doubly Fed Induction Generator (DFIG), Combined Cycle Gas Turbine (CCGT) and Demand Side Response (DSR) are connected at buses 4, 20, 25 and 9, respectively. The nominal voltage of transmission lines is 400 kV in this network.

In EFCC scheme, total system inertia is an essential parameter in the scheme to calculate the imbalance power. System inertia value is used for the estimate of the event size along with the RoCoF value. Power imbalance, P , will be calculated based on equation swing equation introduced previously which is presented below:

For validation of entire scheme, the test system model is configured to conditions reflective of future transmission system levels in the year 2020 of inertia including generator inertia and inertia from demand and all other kinds of components which have kinetic energy, and generation technology and demand type, referred as “H2020” in the thesis. Total value of inertia of the whole system can be obtained from various estimation method.

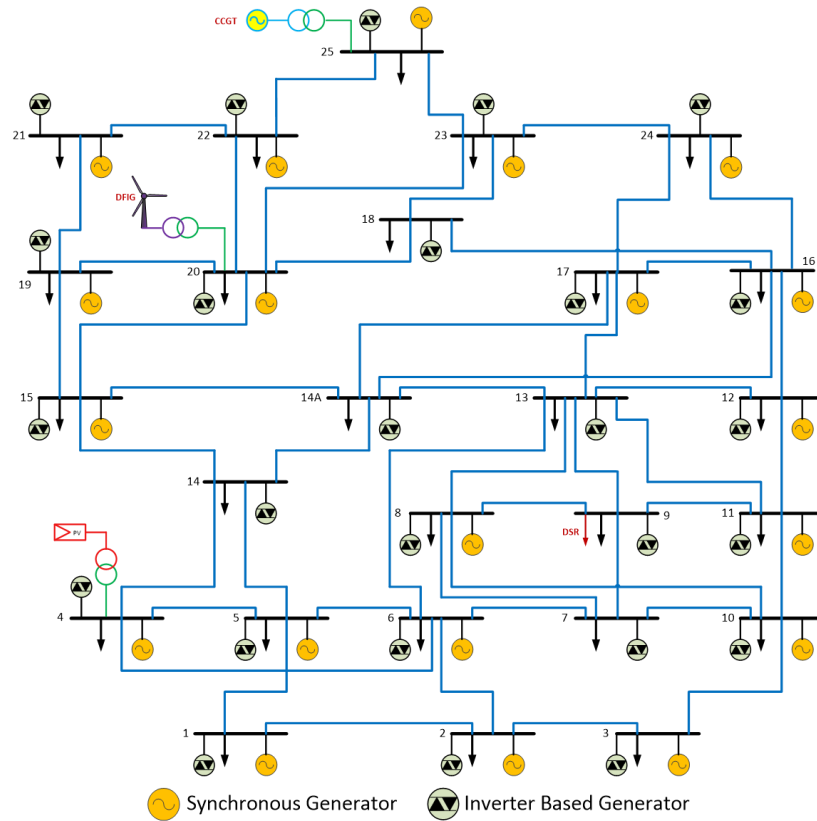


Figure 8-7: Single line diagram of the GB test system.

8.3.2 CHIL Validation of the EFCC Scheme

The CHIL test setup for validating the EFCC scheme is illustrated in Figure 8-6. A reduced GB network model is constructed in RTDS for emulating frequency disturbances. In these tests, the EFCC scheme contains four LCs, two RAs and one CS. The network is configured to have two different regions (corresponding to the two RAs), with each region containing a mix of synchronous generators and converter-based generation. There are in total four resources (corresponding to the four LCs), with each region containing two resources providing the EFCC responses. The resource information is provided in Table 8-1. Total rated power of synchronous generators in the GB test system is 31045 MVA. The network model is dispatched to represent the lowest inertia level with stored kinetic energy of 80 GVAs in the GB transmission system in 2021/2 based on the studies conducted in [111].

8.3.3 Virtual PMUs Placement and PMU's Weight Calculation

The aggregation of input signals (PMU frequency and angle) is based on the weightings applied to each input signal as defined by the user. So it is vital important to set the weightings

Table 8-1: EFCC resource information for CHIL test.

Parameter	LC1	LC2	LC3	LC4
<i>Type</i>	CCGT	Wind	PV	DSR
<i>A</i>	Yes	Yes(caseA1) No(caseA2)	Yes	Yes
P^+	200 MW	300 MW	300 MW	200 MW
P^-	300 MW	200 MW	100 MW	0 MW
T_D^+	300 ms	100 ms	100 ms	N/A
T_D^-	300 ms	100 ms	100 ms	N/A
dP^+/dt	300 MW/s	1000 MW/s	1000 MW/s	N/A
dP^-/dt	300 MW/s	1000 MW/s	1000 MW/s	N/A
T_P^+	10 s	10 s	10 s	120 s
T_P^-	10 s	10 s	10 s	N/A
Region	1	1	2	2
Ranking	2	1	1	2

in order to obtain the best possible aggregated system frequency and angle for the scheme.

In the test, Virtual PMU of RTDS, simulated PMU by RTDS, is used to measure the voltages and currents of the local busbar, and provide the IEEE C37.118 streams for the controller of the scheme remotely. Virtual PMUs of RTDS have been configured and connected to the controllers. The detail of the configuration is explained below.

PMUs Placement in GB Network

Virtual PMUs which are configured with Regional Aggregators (RAs) are presented in Table 8-2. In this table, The RA which PMU connected, and bus number which PMU installed are presented. PMUs 1, 2, 3, and 4 are mapped with RA1 and PMUs 5, 6, 7, and 8 are mapped with RA2. PMUs configurations with RAs for GB network test system are illustrated in Figure 8-6.

Virtual PMUs which are configured to connect to GE PhasorPoint. GE PhasorPoint is the Phasor Data Concentrator (PDC) and it has been designed for Wide Area Monitoring System (WAMS) and phasor applications solution for system operators and transmission companies. In the test, PhasorPoint is used for recording the test data from all PhasorControllers and PMUs.

Table 8-2: PMU placements in GB test system.

No.	Virtual PMU	Connect to	Bus number
1	PMU Z11	RA1	1
2	PMU Z12	RA1	12
3	PMU Z13	RA1	10
4	PMU Z14	RA1	4
5	PMU Z21	RA2	16
6	PMU Z22	RA2	19
7	PMU Z23	RA2	23
8	PMU Z24	RA2	25

Virtual PMUs Weight Calculation

As there is no defined equation or method to weight the PMUs in the scheme, therefore following equation for the calculation of PMUs' weights is proposed for GB system model, by calculating a ratio between individual generator inertia and the regional inertia:

$$\text{Weight}_{\text{PMU}}^i = \frac{H_{SG}^i S_{SG}^i}{H_{\text{region}} S_{\text{region}}} \quad (8-12)$$

As it mentioned in Table 8-2, some buses are chosen for monitoring purposes with PMUs. It is worth to mention that selecting these buses for monitoring by PMUs will result in monitoring of 66% of total inertia in region 1.

The same procedure is conducted for calculation of PMUs' weights in region 2. It is worth mentioning that in this case, the inertia of the two regions are similar. In practice, the weightings for all regions should reflect the difference of regional inertia as in future there is likely to have a less even inertia distributed system.

8.4 Test Description and Cases

Real-time simulations provide a suitable testbed to perform HIL testing, in which the transient processes in a real power system has been simulated using the RTDS. The RTDS produces test signals to be fed into the device under test, which in this study is the GE phasor controller loaded with the designed EFCC control algorithm. The RTDS testing facility provides sufficient flexibility to perform tests with a number of different test scenarios with all mentioned service providers modelled.

The test scenario delivered is based on a framework where RTDS uses virtual PMUs to provide IEEE C37.118 streams of the measured frequency and angle signals to the controller hardware and receives control output from it as input feedback into the real-time simulation. This “closes the loop” between the simulator and the controller allows the real-time simulation to incorporate the response of the control hardware. The modelled GB test system is selected considering the requirements of producing adequate results and the fact that only limited hardware is available places limitations on the size of the test system and the complexity of the equipment models that can be included in the test system.

The testing focuses on the performance of the entire EFCC scheme for the GB test system and made up of the following stages and individual tests:

1. Load increment and disconnection in region 1 and region 2.
2. Security against Short Circuits.
3. Frequency events followed by a short circuit fault.
4. Sensitivity analysis:
 - Impact of PMU weights on the estimated system frequency.
 - Impact of the amount of frequency response from service providers.
 - Impact of ramp up rate of service provider response.

Test1: Sudden connection of a 1000 MW load

In this case, the availability of service provider PV, as shown in Table 8-3 is set to 1300 MW to be sufficient for the disturbance size which is 1000 MW. In Figure 8-8, the system frequency is obtained from the local controller using Phasor Point software. Two cases are compared when the EFCC scheme is activated and not. The effect of EFCC is significant as the frequency nadir is improved from 49.35 Hz which has violated 49.5 Hz limit to 49.65 Hz. In Figure 8-9, system RoCoF, event detection signal and response of service provider is given below. It is noted that the RoCoF estimation is 0.2 Hz/s which is larger than predefined threshold 0.15 Hz/s, so that the event is detected, and service provider has responded. In this case, 700 MW is requested from PV. To further illustrate how EFCC scheme has responded, Figure 8-11 is given which shows the details in the first 2 seconds when disturbance happened. It is noted that the event detection and response request time is 250 ms.

Table 8-3: Availability of service providers in test case 1.

	Service provider	Available power (MW)
Region 1	DSR	200
	PV	1300
Region 2	CCGT	200
	Wind	300

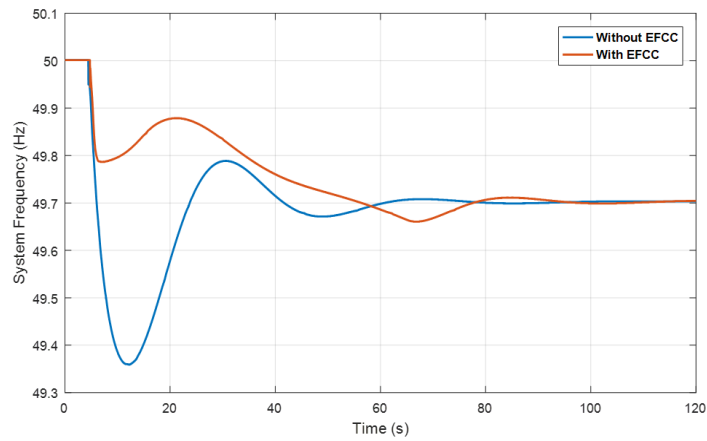


Figure 8-8: System frequency response of a 1000 MW load increase event at bus 9 of region 1.

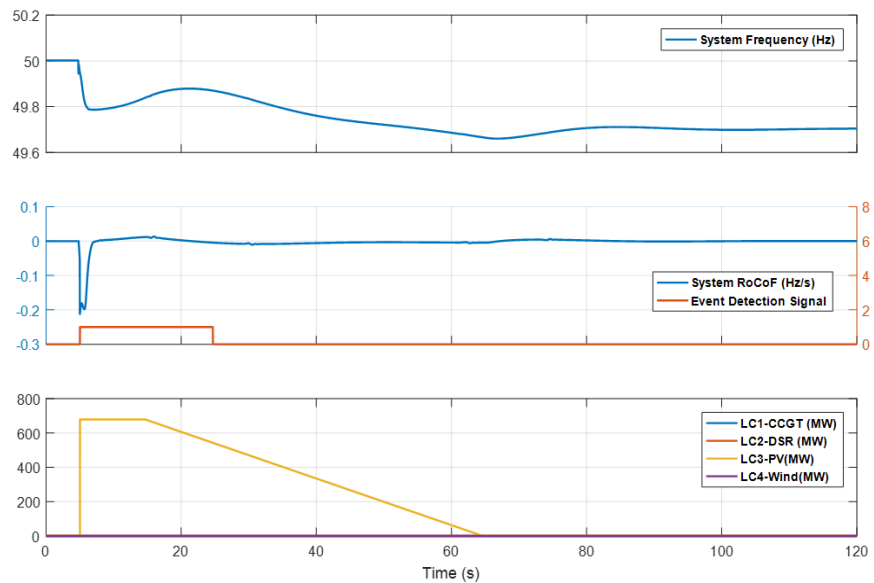


Figure 8-9: Simulation results of a 1000 MW load increase event at bus 9 of region 1.

Additionally, at the beginning of the event (at 1s), there is a spike in the system frequency which caused by the sudden system angle changes due to the sudden power imbalance, which is not reflecting the actual system frequency. The scheme can detect this abnormal spike and not to response initial transient but rather the longer-term frequency trend.

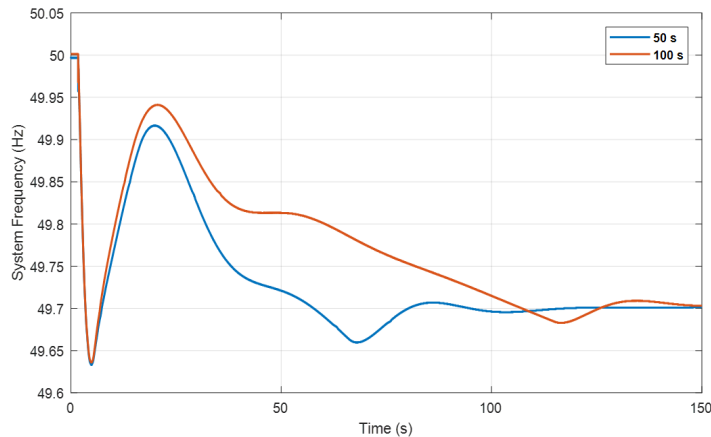


Figure 8-10: Simulation results of a 1000 MW load increase at bus 9 of region 1 with two different service pulling off speed.

It is also notable that after the service provider has dispatched its power and start to pull off, a second frequency drop is observed. In Figure 8-10, a study is conducted to show the effect of the pulling off speed of service provider (50 s and 100 s for pulling off the service provider). If ramping down of FFR at a slower speed, a better frequency behaviour after 40 s can be achieved, as the governors are now slowly responding to slower falling frequency. However, it means that the service providers are required to be able to sustain the output for a longer period.

It should also be pointed out that the post-contingency steady-state frequency is below 49.8 Hz. In practice, secondary control should kick in and improve the frequency back above 49.8 Hz. In the test, secondary control is not considered. Therefore, the steady-state frequency after the event is mainly determined by the droop setting of the generator governor.

Test2: Sudden connection of a 1500 MW load

To further explore the capability of the scheme, the disturbance size is set to 1500 MW which is close to the maximum possible generator loss in the current GB system. The availability of service providers remains the same as test case 1. The RoCoF measured in Figure 8-13

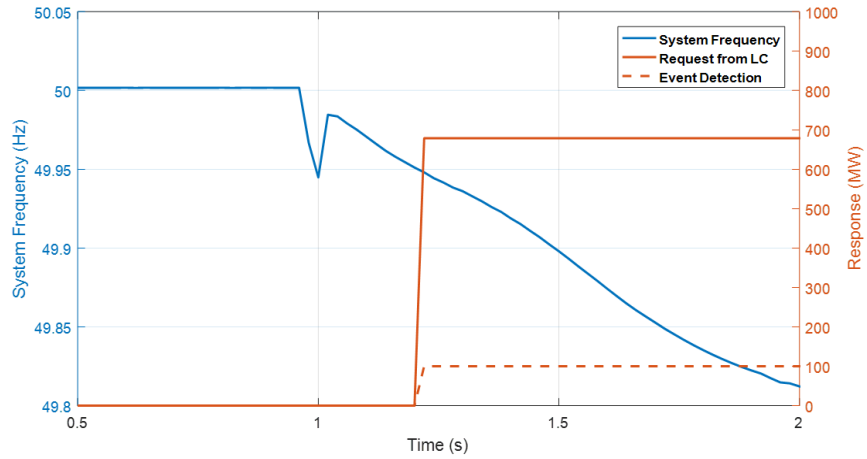


Figure 8-11: Simulation results of a 1000 MW load increase at bus 9 of region 1.

is 0.3 Hz/s while the frequency response is given in Figure 8-12. Despite the larger size of the active power deficit, the requested response is not significantly increased, due to the initial frequency spike caused by a large disturbance which forces controllers to hold until the spike damps out. Then the moment to estimate RoCoF is later than the initial point. In this way, the security of the scheme is assured without compromising the required frequency response.

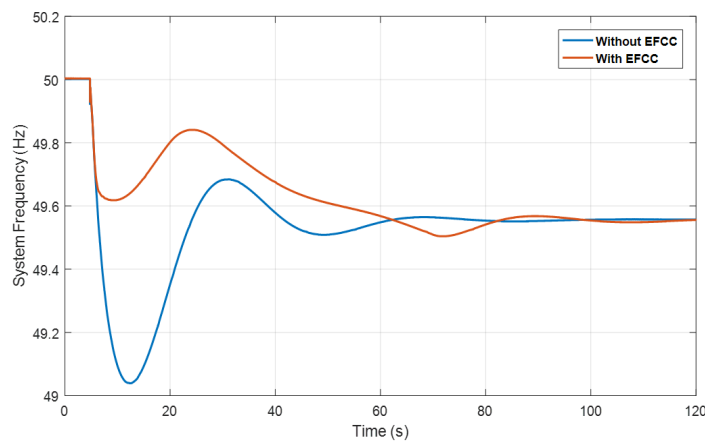


Figure 8-12: System frequency response of a 1500 MW load increase event at bus 9 of region 1.

Test3: Sudden connection of a 1000 MW load in a different region

In this case, the location of the disturbance is moved to the other region to test if the EFCC can correctly detect the location and issue the corresponding command.

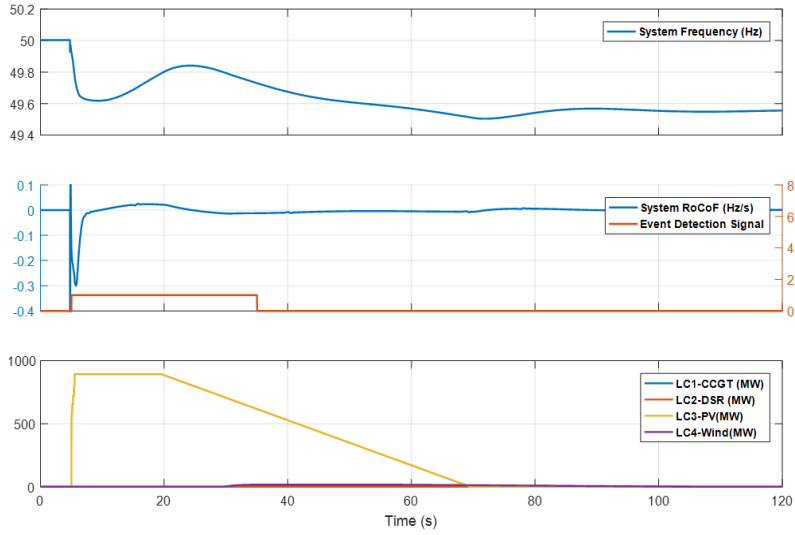


Figure 8-13: Simulation results of a 1500 MW load increase event at bus 9 of region 1.

Table 8-4: Availability of service providers in test case 3.

	Service provider	Available power (MW)
Region 1	DSR	200
	PV	300
Region 2	CCGT	200
	Wind	1300

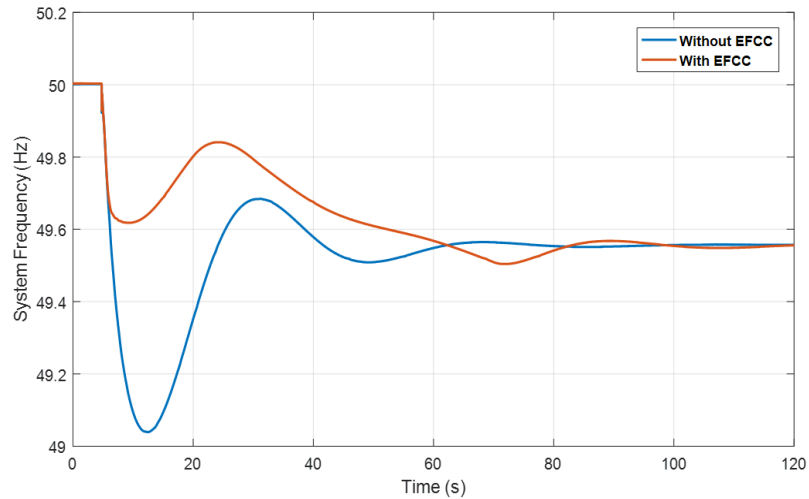


Figure 8-14: System frequency of a 1000 MW load increase event at bus 21 of region 2

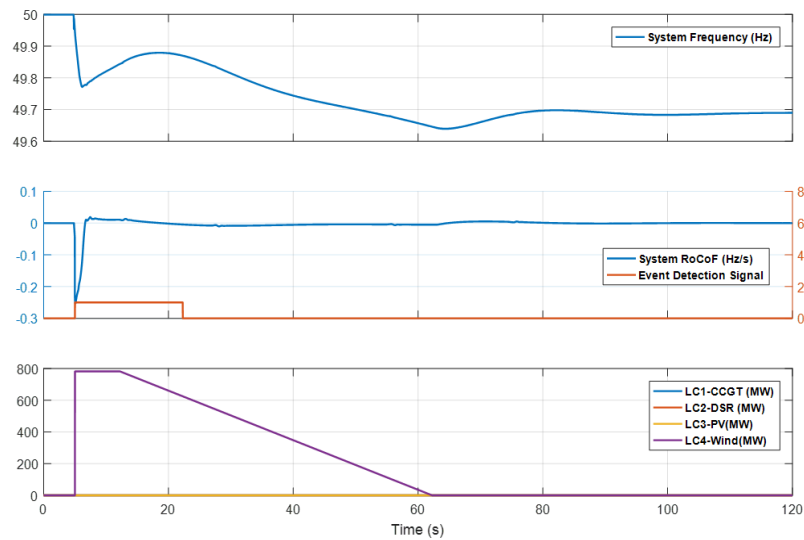


Figure 8-15: Simulation results of a 1000 MW load increase event at bus 21 of region 2

Test4: Effects of short circuit fault

From Figure 8-16, it can be seen that regional aggregator has detected a fault in the system and effectively issued a fault detection signal preventing any maloperation. After fault cleared in the system, the controller started to calculate the RoCoF. However in this case, the post-event RoCoF did not violate the defined threshold. Therefore, the scheme was not triggered and no frequency response was instructed. From Figure 8-17, it can be seen that the voltage at region 1 dropped below threshold (0.85 p.u.) which triggered fault detection block. On the other hand, it is also noted that the voltage in the system is largely depressed through the whole system. The closer to the fault location, the deeper voltage

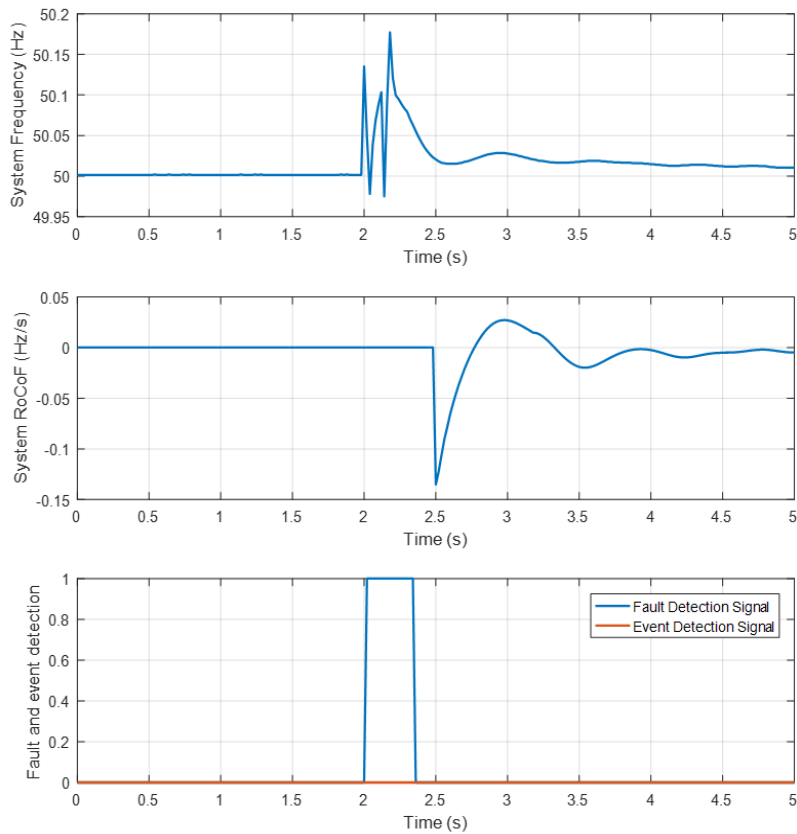


Figure 8-16: Simulation result of a 140 ms single line ground fault at bus 3 of region 1

drop is observed.

Test5: Generator tripping after a short circuit fault at bus 5

In this case, a 140 ms single phase ground fault is applied at bus 5 and then a generator (1000 MW) at bus 5 is tripped. As shown in the figure 8-19 and 8-20, similarly to the cases with load connection, the fault is detected and temporarily paused the event triggering, and event detection is enabled after fault cleared. As the estimated RoCoF has violated the 0.15 Hz/s threshold, the scheme is enabled and the amount of requested power from PV is 850 MW. Figure 8-19 demonstrates status of the signals in a zoomed period shortly after the disturbance. It proves that the scheme is able to correctly detect and respond to events that occur in the aftermath of faults. The scheme is secure against line disconnection after a fault.

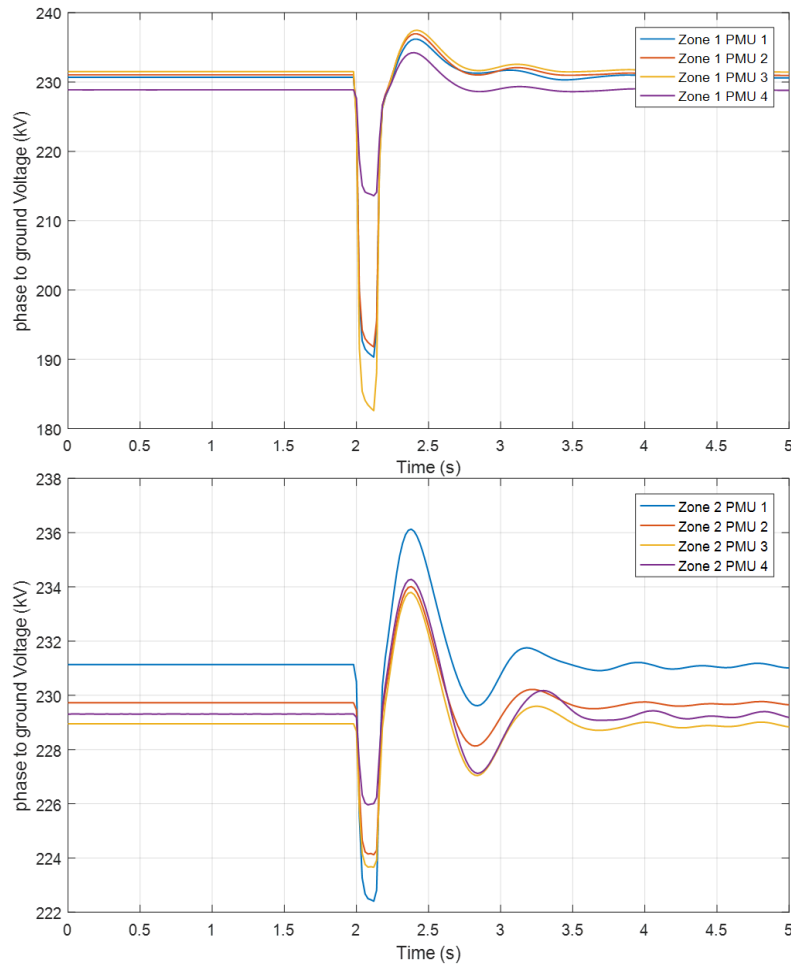


Figure 8-17: Voltages measured by PMU during 140 ms single line ground fault at bus 3 of region 1

Sensitivity analysis: Impact of PMU weights on system frequency by comparing f_{COI} from RTDS

In this test case, PMUs are weighted in two ways. The first one is to equally set all weights to 25. The second one is to calculate weights based on the generator inertia connected at the same bus, described in previous section. The COI frequency is derived from RTDS and based on the generator speed which represents system frequency most accurately. To illustrate the difference, a 1000 MW load is connected at 12 seconds. It is noted that the transient spike at the beginning of the event is both observed in both PMU weighting method. But that equal weighting is removing more of the oscillation in the frequency while the proximity weighting shows more frequency oscillation. The reason to see such results is that we have a limited number of PMUs (total 8 out of 25 buses) due to the limitation of RTDS resources. It is suggested to further investigate the impact with a higher number

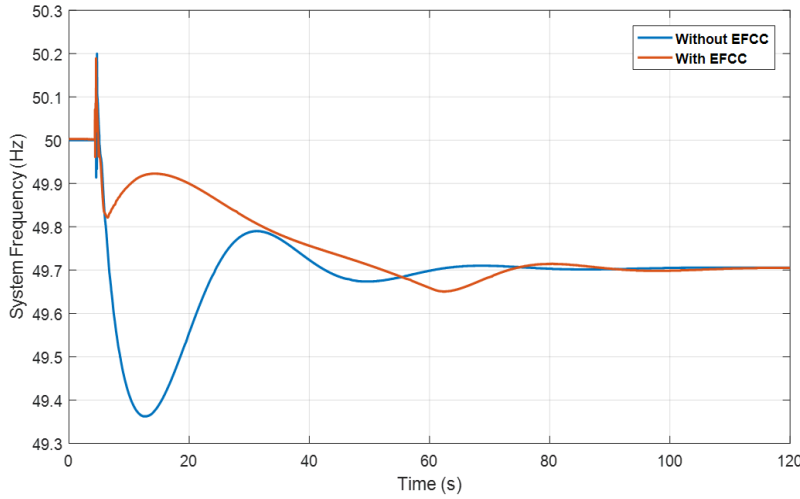


Figure 8-18: System frequency of generator tripping after a fault at bus 5 in region 1

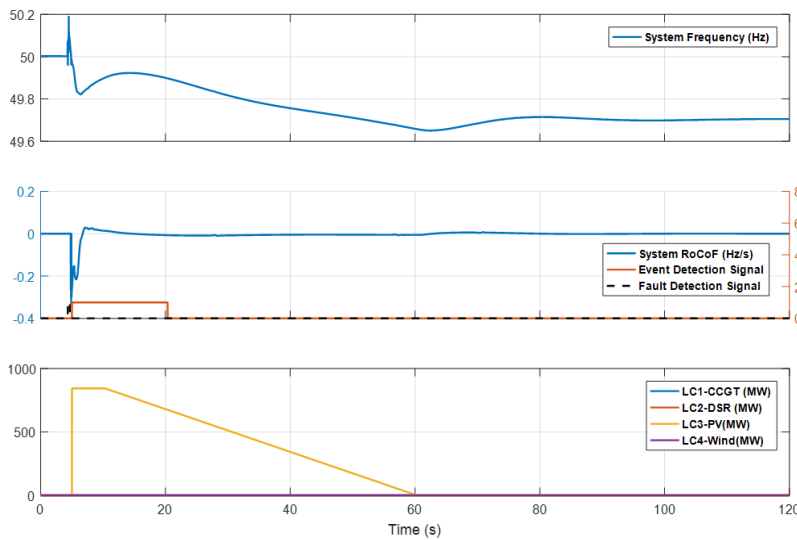


Figure 8-19: Simulation result of generator tripping after a fault at bus 5 of region 1

of PMUs and the optimal way to place PMUs in the system for future study. On the other hand, the visibility can be influenced by the location of the disturbance. Especially, in this case, there is one PMU having a higher weight located at the disturbed bus, therefore the oscillation at this particular bus is introduced to the aggregated frequency. In Figure 8-23, the difference of two PMU weight setting method is clearly shown. For the equal weight method, the RoCoF is underestimated to the actual COI value.

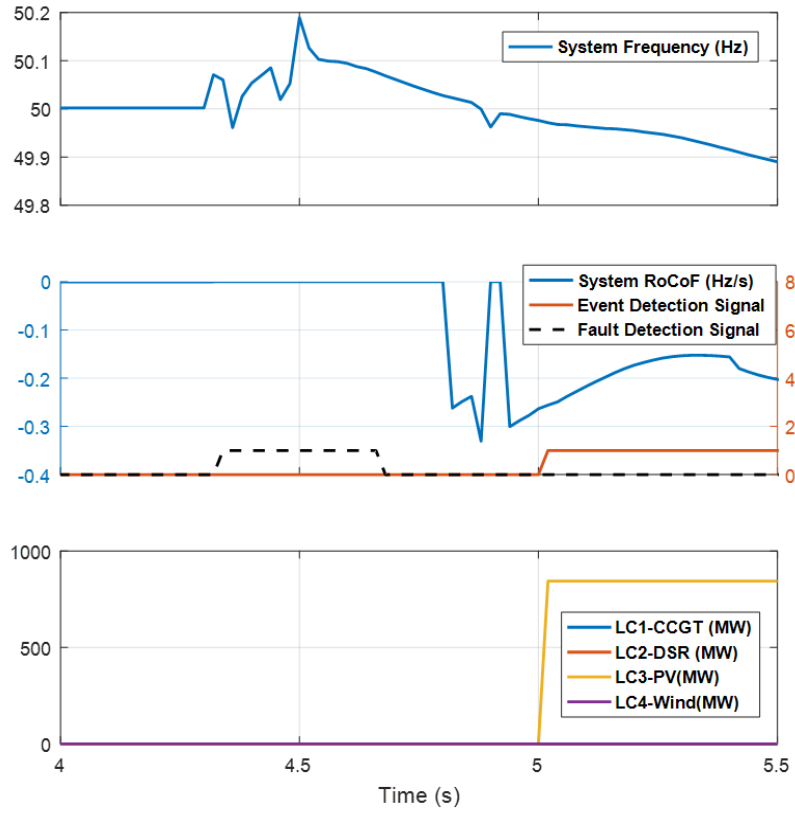


Figure 8-20: Simulation result of generator tripping after a fault at bus 5 of region 1 (zoomed)

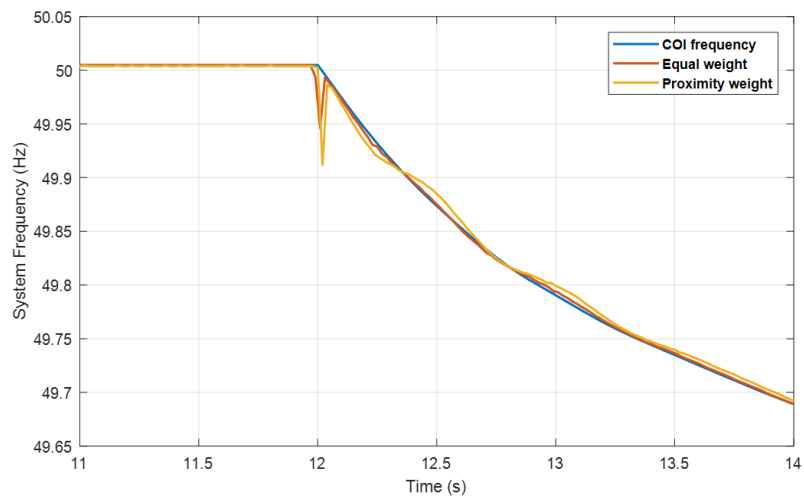


Figure 8-21: System frequency of different PMU weight configurations

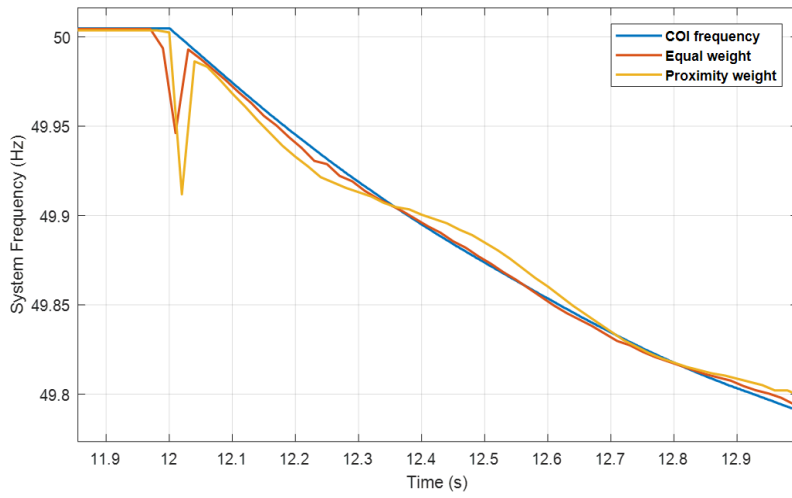


Figure 8-22: System frequency of different PMU weight configurations (zoomed)

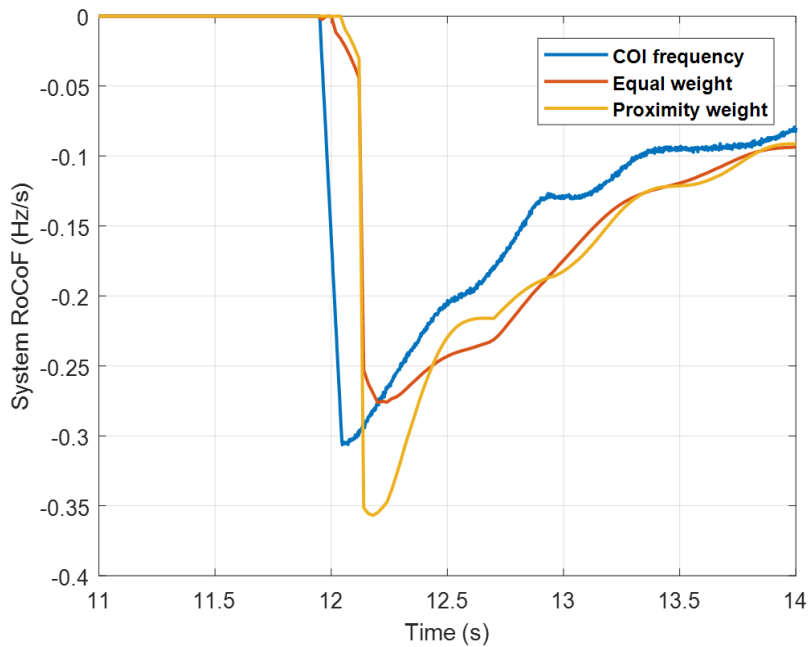


Figure 8-23: System RoCoF of different PMU weight configurations

8.5 Chapter Summary

This chapter has presented the design and validation of a WAMC system capable of detecting and analysing the regional impact of disturbances, and subsequently deploying fast and coordinated responses with consideration of the characteristics and capabilities of a range of different resources.

Case studies have been presented, using CHIL approach to test the scheme. The test results have demonstrated that the scheme is capable of fast detection of frequency events and deploying FFR in a coordinated and optimised manner to enhance frequency restoration in low-inertia systems, thus providing a promising solution for the frequency control of future power systems.

Chapter 9

Thesis Summary

This chapter presents the conclusions of the research, summarises the main contributions and suggestions for future research in the area of frequency control in a power system with high penetration of Power Electronic interfaced sources.

9.1 Conclusion

In this thesis, the research presented is to create new frequency control methods for a power system with high penetration of Power Electronic interfaced sources.

The research first starts with a review of existing frequency control in Chapter 2. It has revealed that the existing control methods will no longer be effective in a high PE-penetrated system due to the uncertainty and reduced system inertia. To improve those methods, there is a need to implement SMT and WAMPC into the system to support critical system information for new frequency control methods.

A study of PE converter modelling and control is conducted to understand further how the PE converter could affect the system frequency control. The study of its model and control allows a deeper understanding of the PE converter's role in the future system and highlights its potential benefit for new frequency control methods because of VSC converters' fast response speed. A high-fidelity model of PE converter and its control are then modelled, and simulation results have proved its frequency support capability.

Then, the system frequency response in low-inertia systems is investigated in chapter 4, revealing that current primary control is not sufficient in a low-inertia system. Furthermore,

the impact of RoCoF relay on the system frequency stability is also assessed. A GB transmission network with DG models is used for this study. The obtained results have shown that the unwittingly tripping of DGs during a large frequency event could further stress the system frequency stability. Fast frequency response is also simulated to compare with existing primary control. The benefit of the fast frequency response is proved. However, it also reveals that the time frame of such a fast frequency response is very short, requiring a faster and more reliable communication system.

As the importance of inertia has been addressed in previous chapters and studies, it is vital to investigate a method for online estimation of the system inertia. Instead of a post-mortem approach, wide area measurements and the swing equation are used to create an online inertia estimation algorithm. The accuracy of estimation is satisfactory for further application of inertia based frequency control. The proposed method can also be utilised to estimate the inertia of various power system components, i.e., a distribution network with embedded DGs or a certain region of the network as long as the power balance in and out of the region can be measured at the boundary.

With estimated inertia, a decentralised under frequency load shedding strategy is proposed to adaptively adjust load shedding amounts according to system inertia using local measurements. The performance of the proposed UFLS scheme is assessed using both the IEEE 39-bus test system and the GB test system. The obtained results have shown that the proposed method can adequately protect the system from frequency instability. The estimation of RoCoF is accurate, thus it can successfully reflect the actual disturbance size and decide the amount of load shedding. Compared with the conventional UFLS scheme, the proposed method can achieve better performance in terms of higher nadir and correct load shedding amount. This is particularly effective before a full Wide Area Monitoring System (WAMS) scheme can be established in the system and can be an important protection scheme in parallel with future WAMS based frequency control scheme. Additionally, an algorithm to compensate for the reduction of the system inertia due to generator tripping is created, the post-event system inertia can then be corrected to produce a more accurate LoG estimation.

In the case of SMT and WAMS system implemented, a fast frequency control scheme using WAMS is then presented, which uses real time frequency data from PMUs and determines the required responses. The system takes into account the impact of the frequency

event on different parts of the network and allocates responses at a regional level. The characteristics and capabilities of different connected resources are considered so that a co-ordinated and optimised response can be dispatched immediately following the event.

Besides all created methods, a high fidelity RTDS based real time simulation testbed is constructed in the lab to facilitate the simulation and validation of proposed frequency control methods, using Controller-in-the-loop (CIL) and Hardware-in-the-Loop (HIL) techniques. Algorithms or devices under test can be verified through real-time simulation in a closed-loop manner.

9.2 Future Developments

The work presented in this research has met all its objectives and successfully made a number of contributions. Nevertheless, there are still several areas where further developments could be made in order to extend the ideas and improve the methods created in this thesis.

As the topic of this thesis is about the impact of PE converters on system frequency control, it is suggested that future development could include the FFR and synthetic inertia functions into the power electronic model used. Therefore, the interactions between the proposed frequency control methods and FFR and synthetic inertia can be further assessed.

The inertia estimation method presented in chapter 5 could be further verified using real measurements in the system. As there is no complete wide area monitoring system existing in the system, data from one single PMU at a generator busbar can be the next step for validation of the method in the near future. PMUs at the grid connection point between transmission network and distribution network could also be used to assess the inertia level of the down stream distribution network. By doing this, the equivalent inertia of the demand could be estimated if the inertia of all rotating machines in the distribution network are known.

Another suggestion is to include a PMU placement strategy for the WAMS based fast frequency control. The number of PMUs used in chapter 8 is limited by the RTDS resources in this study and also in the real network due to the slow adoption of SMT technology around the world. It would be of great interest to develop an optimal PMU placing and weighting algorithm to improve the performance of the proposed method. It is vital to maximise the accuracy of any such scheme in systems with limited PMUs in a real system.

Across chapter 5 to chapter 7, conventional generators and renewable generators are mainly considered as the source of the frequency response. Nevertheless, the proposed methods can also be applied for demand side response. Demand response is the ability to control the demand side loads to change their consumption based on situation and in response to system changes. By extending the UFLS scheme in chapter 7, a hybrid frequency control scheme could be further developed with the proposed RoCoF estimation method, which utilises the demand response or other FFR resources for fast frequency control and only trigger the adaptive load shedding when the frequency falls further below the statutory limit.

Additionally, the decentralise UFLS scheme can be combined with a WAMS based fast frequency service when there is a WAMS available to explore, which can improve the overall reliability in case of a communication failure.

It is also important to mention there is wider fundamental evidence research behind the premise of frequency support challenges. The economic analysis of all the newly proposed method is always an interesting topic to be further explored. A comprehensive and effective pricing strategy could be really beneficial for rolling out the new frequency control techniques.

Bibliography

- [1] REN21, *REN21. Renewables 2018-global status report, Paris, REN21 Secretariate; 2018*, 2018.
- [2] C40, “25 cities commit to become emissions neutral by 2050 to deliver on their share of the Paris Agreement.” [Online]. Available: <http://www.c40.org/{%}0Apress{-}releases/25-cities-emissions-neutral-by-2050>.
- [3] RGGI, “Regional Greenhouse Gas Initiative (RGGI).” [Online]. Available: <https://www.c2es.org/content/regional-greenhouse-gas-initiative-rggi/>
- [4] ENTSOE, “Completing the map,” 2018.
- [5] National Grid ESO, “Electricity Ten Year Statement,” National Grid, Tech. Rep. November, 2018. [Online]. Available: <https://www.nationalgrideso.com/document/133836/download>
- [6] EUROPEAN COMMISSION, “Energy Roadmap 2050,” Tech. Rep., 2011.
- [7] M. P. Kazmierkowski, *Power Electronics for Renewable and Distributed Energy Systems*, 2014, vol. 8, no. 2.
- [8] D. J. Hill, G. Verbi, F. Milano, D. Florian, and Z. Eth, “Foundations and Challenges of Low-Inertia Systems,” p. 26.
- [9] P. Kundur, J. Paserba, V. Ajjarapu, G. Andersson, A. Bose, C. Canizares, N. Hatziairgyriou, D. Hill, A. Stankovic, C. Taylor, and Others, “Definition and classification of power system stability,” *IEEE transactions on Power Systems*, vol. 19, no. 2, pp. 1387–1401, 2004.

- [10] L. L. Grigsby, *Power system stability and control*. McGraw-hill New York, 2017, vol. 7.
- [11] U.S.-Canada Power System Outage Task Force, “Final Report on the August 14, 2003 Blackout in the United States and Canada: Causes and Recommendations,” Tech. Rep., 2004. [Online]. Available: <https://www.energy.gov/oe/downloads/blackout-2003-final-report-august-14-2003-blackout-united-states-and-canada-causes-and>
- [12] G. Strbac, N. Jenkins, and T. Green, “Future network technologies,” *Report to DTI*, 2006.
- [13] K. Morison, L. Wang, and P. Kundur, “Power system security assessment,” *IEEE Power and Energy Magazine*, vol. 2, no. 5, pp. 30–39, 2004.
- [14] S. Jacobsson and A. Johnson, “The diffusion of renewable energy technology: An analytical framework and key issues for research,” *Energy Policy*, vol. 28, no. 9, pp. 625–640, 2000.
- [15] WWEA, “WIND POWER CAPACITY REACHES 539 GW,” 2018. [Online]. Available: <http://wwindea.org/blog/2018/02/12/2017-statistics/>
- [16] Boythorpe Wind Energy, “Onshore vs Offshore Wind Energy.” [Online]. Available: <https://www.boythorpewindenergy.co.uk/wind-turbine-advice/onshore-vs-offshore-wind-energy/>
- [17] V. Vittal and R. Ayyanar, *Grid Integration and Dynamic Impact of Wind Energy*, ser. Power Electronics and Power Systems. Springer New York, 2012. [Online]. Available: <https://books.google.co.uk/books?id=IIIdrMzGt1QC>
- [18] C. Bajracharya, “Control of VSC-HVDC for wind power,” *Department of Electrical Power Engineering*, vol. MSs Thesis, no. June, p. 75, 2008.
- [19] M. Dreidy, H. Mokhlis, and S. Mekhilef, “Inertia response and frequency control techniques for renewable energy sources: A review,” *Renewable and Sustainable Energy Reviews*, vol. 69, no. November 2015, pp. 144–155, 2017. [Online]. Available: <http://dx.doi.org/10.1016/j.rser.2016.11.170>

- [20] —, “Inertia response and frequency control techniques for renewable energy sources: A review,” *Renewable and Sustainable Energy Reviews*, vol. 69, no. November 2015, pp. 144–155, 2017. [Online]. Available: <http://dx.doi.org/10.1016/j.rser.2016.11.170>
- [21] C. Marinescu, I. Serban, and R. Teodorescu, “Energy storage systems impact on the short-term frequency stability of distributed autonomous microgrids, an analysis using aggregate models,” *IET Renewable Power Generation*, vol. 7, no. February, pp. 531–539, 2013.
- [22] Siemens, “HV Direct Current Transmission System (HVDC),” 2017. [Online]. Available: <http://www.energy.siemens.com/hq/en/power-transmission/hvdc/>
- [23] H. Liu and Z. Chen, “Contribution of VSC-HVDC to Frequency Regulation of Power Systems with Offshore Wind Generation,” *IEEE Transactions on Energy Conversion*, vol. 30, no. 3, pp. 918–926, 2015.
- [24] M. H. Albadi and E. F. El-Saadany, “A summary of demand response in electricity markets,” *Electric power systems research*, vol. 78, no. 11, pp. 1989–1996, 2008.
- [25] P. Babahajiani, Q. Shafiee, and H. Bevrani, “Intelligent Demand Response Contribution in Frequency Control of Multi-Area Power Systems,” *IEEE Trans. on Smart Grid*, vol. 9, no. 2, pp. 1282–1291, mar 2018.
- [26] B. L. Schenkman, D. G. Wilson, R. D. Robinett, and K. Kukolich, “Photovoltaic distributed generation for lanai power grid real-time simulation and control integration scenario,” in *SPEEDAM 2010*. IEEE, 2010, pp. 154–157.
- [27] W. Kramer, S. Chakraborty, B. Kroposki, and H. Thomas, “Advanced Power Electronic Interfaces for Distributed Energy Systems,” no. March, p. 132, 2008.
- [28] G. Ramtharan, J. B. Ekanayake, and N. Jenkins, “Frequency support from doubly fed induction generator wind turbines,” *Renewable Power Generation, IET*, vol. 1, pp. 3–9, 2007.
- [29] G. Delille, B. Francois, and G. Malarange, “Dynamic Frequency Control Support by Energy Storage to Reduce the Impact of Wind and Solar Generation on Isolated

- Power System's Inertia," *IEEE Transactions on Sustainable Energy*, vol. 3, no. 4, pp. 931–939, oct 2012.
- [30] F. Gonzalez-Longatt, E. Chikuni, and E. Rashayi, "Effects of the Synthetic Inertia from wind power on the total system inertia after a frequency disturbance," *Proceedings of the IEEE International Conference on Industrial Technology*, pp. 826–832, 2013.
- [31] A. G. Phadke and J. S. Thorp, *Synchronized phasor measurements and their applications*. Springer, 2008, vol. 1.
- [32] S. Chakrabarti, E. Kyriakides, T. Bi, D. Cai, and V. Terzija, "Measurements get together," *IEEE Power and Energy Magazine*, vol. 7, no. 1, pp. 41–49, 2009.
- [33] P. Crossley, F. Ilar, and D. Karlsson, "System protection schemes in power networks: existing installations and ideas for future development," in *2001 Seventh International Conference on Developments in Power System Protection (IEE)*, apr 2001, pp. 450–453.
- [34] G. Trudel, S. Bernard, and G. Scott, "Hydro-Quebec's defence plan against extreme contingencies," *IEEE Transactions on Power Systems*, vol. 14, no. 3, pp. 958–965, aug 1999.
- [35] A. S. Bakshi, A. Velayutham, S. C. Srivastava, K. Agrawal, R. Nayak, S. Soonee, and B. Singh, "Report of the enquiry committee on grid disturbance in Northern Region on 30th July 2012 and in Northern, Eastern & North-Eastern Region on 31st July 2012," *New Delhi, India*, 2012.
- [36] National Grid Electricity Transmission, "U.K The grid code," no. 5, 2015.
- [37] Y. G. Rebours, D. S. Kirschen, M. Trotignon, and S. Rossignol, "A survey of frequency and voltage control ancillary services - Part II: Economic features," *Ieee Transactions on Power Systems*, vol. 22, no. 1, pp. 358–366, 2007. [Online]. Available: <http://www2.econ.iastate.edu/tesfatsi/VoltageControlASPart2.Kirschen2007.IEEEas{ }econ2007.pdf>
- [38] G. F. Wood and W. W. Hung, "Generating plant frequency control services," 1995.

- [39] Power System Dynamic Performance Committee, “Dynamic Models for Turbine-Governors in Power System Studies,” Tech. Rep., 2013.
- [40] J. Machowski, J. Bialek, and J. Bumby, *Power system dynamics: stability and control*. John Wiley & Sons, 2011.
- [41] V. V. Terzija, “Adaptive underfrequency load shedding based on the magnitude of the disturbance estimation,” *IEEE Transactions on Power Systems*, vol. 21, no. 3, pp. 1260–1266, 2006.
- [42] U. Rudez and R. Mihalic, “WAMS-Based Underfrequency Load Shedding with Short-Term Frequency Prediction,” *IEEE Transactions on Power Delivery*, vol. 31, no. 4, pp. 1912–1920, 2016.
- [43] M. Karimi, P. Wall, H. Mokhlis, and V. Terzija, “A New Centralized Adaptive Underfrequency Load Shedding Controller for Microgrids Based on a Distribution State Estimator,” *IEEE Transactions on Power Delivery*, vol. 32, no. 1, pp. 370–380, 2017.
- [44] T. Shekari, F. Aminifar, and M. Sanaye-Pasand, “An analytical adaptive load shedding scheme against severe combinational disturbances,” *IEEE Transactions on Power Systems*, vol. 31, no. 5, pp. 4135–4143, 2016.
- [45] National Grid, “Transmission Annual Report for 2009 -10 Document Type : Annual Report Overview :,” *Control*, no. March 2010, 2011.
- [46] PSNH, “Final Report on the August 14, 2003 Blackout in the United States and Canada: Causes and Recommendations, April 2004, U.S.-Canada Power System Outage Task Force,” no. April, 2003. [Online]. Available: <https://www3.epa.gov/region1/npdes/merrimackstation/pdfs/ar/AR-1165.pdf>
- [47] A. Y. N Chaudhuri, B Chaudhuri, R Majumder, *Multi-terminal direct-current grids: Modeling, analysis, and control*. John Wiley & Sons, 2014.
- [48] J. Arrillaga, Y. H. Liu, and N. R. Watson, *Flexible power transmission: the HVDC options*. John Wiley & Sons, 2007.
- [49] K. Ma, M. Liserre, and F. Blaabjerg, “Power Controllability of Three-phase Converter with Unbalanced AC Source,” vol. 30, no. 3, pp. 342–350, 2013.

- [50] A. Moawwad, M. S. El Moursi, and W. Xiao, "A novel transient control strategy for VSC-HVDC connecting offshore wind power plant," *IEEE Transactions on Sustainable Energy*, vol. 5, no. 4, pp. 1056–1069, 2014.
- [51] O. Jasim, H. Q. S. Dang, G. E. Energy, C. Grid, and S. Leonard, "Advanced Control Method for VSC-HVDC Systems Connected to Weak Grids Keywords," no. Vcc, pp. 1–10.
- [52] C. Bajracharya, "Control of VSC-HVDC for wind power," Master's thesis, Institutt for elkraftteknikk, 2008.
- [53] R. Marquardt, "Modular Multilevel Converter: An universal concept for HVDC-Networks and extended DC-Bus-applications," in *Power Electronics Conference (IPEC), 2010 International*. IEEE, 2010, pp. 502–507.
- [54] A. Lesnicar and R. Marquardt, "An innovative modular multilevel converter topology suitable for a wide power range," in *Power Tech Conference Proceedings, 2003 IEEE Bologna*, vol. 3. IEEE, 2003, pp. 6—pp.
- [55] S. Preitl and R.-E. Precup, "An extension of tuning relations after symmetrical optimum method for PI and PID controllers," *Automatica*, vol. 35, no. 10, pp. 1731–1736, 1999.
- [56] P. Kundur, *Power System Stability And Control*. McGraw-Hill, Inc, 1994.
- [57] National Grid, "System Operability Framework 2016," Tech. Rep. November, 2016. [Online]. Available: <https://www.nationalgrideso.com/insights/system-operability-framework-sof>
- [58] EirGrid, "Rate of Change of Frequency (ROCOF) Workstream," no. November, pp. 1–7, 2011.
- [59] National Grid, "Enhanced Frequency Control Capability (EFCC)." [Online]. Available: <https://www.nationalgrideso.com/innovation/projects/enhanced-frequency-control-capability-efcc>

- [60] A. Junyent-Ferr, Y. Pipelzadeh, and T. C. Green, “Blending HVDC-Link Energy Storage and Offshore Wind Turbine Inertia for Fast Frequency Response,” *IEEE Transactions on Sustainable Energy*, vol. 6, no. 3, pp. 1059–1066, jul 2015.
- [61] O. D. Adeuyi, M. Cheah-Mane, J. Liang, and N. Jenkins, “Fast Frequency Response From Offshore Multiterminal VSC–HVDC Schemes,” *IEEE Transactions on Power Delivery*, vol. 32, no. 6, pp. 2442–2452, dec 2017.
- [62] E. Vrettos, C. Ziras, and G. Andersson, “Fast and Reliable Primary Frequency Reserves From Refrigerators With Decentralized Stochastic Control,” *IEEE Transactions on Power Systems*, vol. 32, no. 4, pp. 2924–2941, jul 2017.
- [63] D. Chakravorty, B. Chaudhuri, and S. Y. R. Hui, “Rapid Frequency Response From Smart Loads in Great Britain Power System,” *IEEE Transactions on Smart Grid*, vol. 8, no. 5, pp. 2160–2169, 2017.
- [64] D. Ochoa and S. Martinez, “Fast-Frequency Response Provided by DFIG-Wind Turbines and its Impact on the Grid,” *IEEE Transactions on Power Systems*, vol. 32, no. 5, pp. 4002–4011, 2017.
- [65] A. F. Hoke, M. Shirazi, S. Chakraborty, E. Muljadi, and D. Maksimovic, “Rapid Active Power Control of Photovoltaic Systems for Grid Frequency Support,” *IEEE Journal of Emerging and Selected Topics in Power Electronics*, vol. 5, no. 3, pp. 1154–1163, 2017.
- [66] T. Xu, W. Jang, and T. Overbye, “Commitment of Fast-Responding Storage Devices to Mimic Inertia for the Enhancement of Primary Frequency Response,” *IEEE Transactions on Power Systems*, vol. 33, no. 2, pp. 1219–1230, mar 2018.
- [67] F. Teng, V. Trovato, and G. Strbac, “Stochastic Scheduling With Inertia-Dependent Fast Frequency Response Requirements,” *IEEE Transactions on Power Systems*, vol. 31, no. 2, pp. 1557–1566, mar 2016.
- [68] F. Wilches-Bernal, R. Concepcion, J. C. Neely, R. H. Byrne, and A. Ellis, “Communication Enabled—Fast Acting Imbalance Reserve (CE-FAIR),” *IEEE Transactions on Power Systems*, vol. 33, no. 1, pp. 1101–1103, jan 2018.

- [69] C. F. Ten and P. A. Crossley, "Evaluation of ROCOF relay performances on networks with distributed generation," 2008.
- [70] R. Bugdal, A. Dysko, G. M. Burt, and J. R. McDonald, "Performance analysis of the ROCOF and vector shift methods using a dynamic protection modelling approach," in *15th International Conference on Power System Protection*, 2006, pp. 139–144.
- [71] M. Grebla, J. R. A. K. Yellajosula, and H. K. Høidalen, "Adaptive Frequency Estimation Method for ROCOF Islanding Detection Relay," *IEEE Transactions on Power Delivery*, vol. 35, no. 4, pp. 1867–1875, aug 2020.
- [72] P. Castello, J. Liu, C. Muscas, P. A. Pegoraro, F. Ponci, and A. Monti, "A Fast and Accurate PMU Algorithm for P+M Class Measurement of Synchrophasor and Frequency," *IEEE Transactions on Instrumentation and Measurement*, vol. 63, no. 12, pp. 2837–2845, dec 2014.
- [73] X. Cao, B. Stephen, I. F. Abdulhadi, C. D. Booth, and G. M. Burt, "Switching Markov Gaussian Models for Dynamic Power System Inertia Estimation," *IEEE Transactions on Power Systems*, vol. 31, no. 5, pp. 3394–3403, 2016.
- [74] A. Ulbig, T. S. Borsche, and G. Andersson, "Impact of low rotational inertia on power system stability and operation," *IFAC Proceedings Volumes (IFAC-PapersOnline)*, vol. 19, pp. 7290–7297, 2014.
- [75] B. V. Terzija, G. Valverde, D. Cai, P. Regulski, V. Madani, J. Fitch, S. Skok, M. M. Begovic, and A. Phadke, "Wide-Area Monitoring , Protection , and Control of Future Electric Power Networks," vol. 99, no. 1, 2011.
- [76] T. Inoue, H. Taniguchi, Y. Ikeguchi, and K. Yoshida, "Estimation of power system inertia constant and capacity of spinning-reserve support generators using measured frequency transients," *IEEE Transactions on Power Systems*, vol. 12, no. 1, pp. 136–143, 1997.
- [77] D. P. Chassin, Z. Huang, M. K. Donnelly, C. Hassler, E. Ramirez, and C. Ray, "Estimation of WECC system inertia using observed frequency transients," *IEEE Transactions on Power Systems*, vol. 20, no. 2, pp. 1190–1192, 2005.

- [78] K. Tuttelberg, J. Kilter, D. Wilson, and K. Uhlen, "Estimation of Power System Inertia From Ambient Wide Area Measurements," *IEEE Transactions on Power Systems*, vol. 33, no. 6, pp. 7249–7257, nov 2018.
- [79] V. Terzija, M. Djuric, and B. Kovacevic, "A new self-tuning algorithm for the frequency estimation of distorted signals," *IEEE Transactions on Power Delivery*, vol. 10, no. 4, pp. 1779–1785, 1995.
- [80] V. V. Terzija, M. B. Djuric, and B. D. Kovacevic, "Voltage phasor and local system frequency estimation using Newton type algorithm," *IEEE Transactions on Power Delivery*, vol. 9, no. 3, pp. 1368–1374, 1994.
- [81] P. M. Anderson and A. A. Fouad, *Power system control and stability*. John Wiley & Sons, 2008.
- [82] J. M. Blackledge, *Digital Signal Processing: Mathematical and Computational Methods, Software Development and Applications*, ser. Woodhead Publishing Series in Electronic and Optical Materials. Elsevier Science, 2006. [Online]. Available: <https://books.google.co.uk/books?id=g4ekAgAAQBAJ>
- [83] R. technologies, "Real Time Digital Power System Simulator."
- [84] CIRCE, "Real Time Digital Simulator: Laboratory - RTDS," 2019. [Online]. Available: <http://www.fcirce.es/web/page.aspx?id=labs>
- [85] V. Skendzic and A. Guzman, "Enhancing power system automation through the use of real-time ethernet," in *2006 Power Systems Conference: Advanced Metering, Protection, Control, Communication, and Distributed Resources*. IEEE, 2006, pp. 480–495.
- [86] GridProtectionAlliance, "OpenPDC." [Online]. Available: <https://github.com/GridProtectionAlliance/openPDC>
- [87] Copadata, "Straton-Industrial software for IEC 61131-3 applications." [Online]. Available: <https://www.copadata.com/en/hmi-scada-solutions/straton/>

- [88] B. Lundstrom, S. Chakraborty, B. Kramer, D. Terlip, and B. Kroposki, "An advanced platform for development and evaluation of photovoltaic inverters using hardware-in-the-loop," *International Journal of Distributed Energy Resources and Smart Grids*, vol. 9, no. NREL/JA-5D00-55880, 2013.
- [89] C. Zhang, V. K. Vijapurapu, A. K. Srivastava, N. N. Schulz, J. Bastos, and R. Wierckx, "Hardware-in-the-loop simulation of distance relay using RTDS," in *Proceedings of the 2007 summer computer simulation conference*. Society for Computer Simulation International, 2007, pp. 149–154.
- [90] D. Prasetijo, W. R. Lachs, and D. Sutanto, "A new load shedding scheme for limiting underfrequency," *IEEE Transactions on Power Systems*, vol. 9, no. 3, pp. 1371–1378, 1994.
- [91] "Future Energy Scenarios," National Grid, Tech. Rep., 2018. [Online]. Available: <http://fes.nationalgrid.com/>
- [92] D. Wilson, S. Clark, et al., "Advances in Wide Area Monitoring and Control to address Emerging Requirements related to Inertia, Stability and Power Transfer," in *CIGRE Paris Session*, 2016.
- [93] F. Milano, "Rotor speed-free estimation of the frequency of the center of inertia," *IEEE Transactions on Power Systems*, vol. 33, no. 1, pp. 1153–1155, 2018.
- [94] B. Shi, X. Xie, and Y. Han, "WAMS-based load shedding for systems suffering power deficit," *Proceedings of the IEEE Power Engineering Society Transmission and Distribution Conference*, vol. 2005, pp. 1–5, 2005.
- [95] S. Abd Elwahid, "Hardware implementation of an automatic adaptive centralized under frequency load shedding," vol. 29, no. 6, pp. 2664–2673, 2013.
- [96] L. Shun, L. Qingfen, and W. Jiali, "Dynamic optimization of adaptive under-frequency load shedding based on WAMS," *Proceedings of 2016 IEEE Information Technology, Networking, Electronic and Automation Control Conference, ITNEC 2016*, pp. 920–926, 2016.

- [97] L. Sigrist, "A UFLS Scheme for Small Isolated Power Systems Using Rate-of-Change of Frequency," *IEEE Transactions on Power Systems*, vol. 30, no. 4, pp. 2192–2193, 2015.
- [98] J. Zhao, Y. Tang, and V. Terzija, "Robust Online Estimation of Power System Center of Inertia Frequency," *IEEE Transactions on Power Systems*, vol. 34, no. 1, pp. 821–825, jan 2019.
- [99] B. Ahmadzadeh-Shooshtari, R. Torkzadeh, M. Kordi, H. Marzooghi, and F. Eghtedarnia, "SG parameters estimation based on synchrophasor data," *IET Generation, Transmission Distribution*, vol. 12, no. 12, pp. 2958–2967, 2018.
- [100] P. M. Ashton, C. S. Saunders, G. A. Taylor, A. M. Carter, and M. E. Bradley, "Inertia estimation of the GB power system using synchrophasor measurements," *IEEE Transactions on Power Systems*, vol. 30, no. 2, pp. 701–709, 2015.
- [101] U. Rudez and R. Mihalic, "Analysis of underfrequency load shedding using a frequency gradient," *IEEE Transactions on Power Delivery*, vol. 26, no. 2, pp. 565–575, 2011.
- [102] R. Azizipanah-Abarghooee, M. Malekpour, M. Paolone, and V. Terzija, "A New Approach to the On-line Estimation of the Loss of Generation Size in Power Systems," *IEEE Transactions on Power Systems*, vol. PP, no. c, pp. 1–1, 2018. [Online]. Available: <https://ieeexplore.ieee.org/document/8521679/>
- [103] S. H. Horowitz and A. G. Phadke, *Power system relaying*. John Wiley & Sons, 2008.
- [104] M. Lu, W. A. ZainalAbidin, T. Masri, D. H. Lee, and S. Chen, "Under-frequency load shedding (UFLS) schemes – A survey," *International Journal of Applied Engineering Research*, vol. 11, no. 1, pp. 456–472, 2016.
- [105] Q. Hong, M. Karimi, M. Sun, S. Norris, O. Bagleybter, D. Wilson, I. F. Abdulhadi, V. Terzija, B. Marshall, and C. D. Booth, "Design and Validation of a Wide Area Monitoring and Control System for Fast Frequency Response," vol. 11, no. 4, pp. 3394–3404, 2020.

- [106] D. Wilson, O. Bagleybter, S. Norris and K. Maleka, "Control of an electrical power network," Patent WO2016174476A3, Nov 03, 2016. [Online]. Available: <https://patents.google.com/patent/WO2016174476A3/en>
- [107] H. You, V. Vittal, and X. Wang, "Slow coherency-based islanding," *IEEE Trans. on Power Systems*, vol. 19, no. 1, pp. 483–491, Feb 2004.
- [108] "IEEE Std C37.118.1-2011 - IEEE Standard for Synchrophasor Measurements for Power Systems," 2011.
- [109] P. Kundur, *Power System Stability and Control*. McGraw-Hill, 1993.
- [110] A. Vijay, S. Doolla, and M. Chandorkar, "Real-time testing approaches for microgrids," *IEEE Journal of Emerging and Selected Topics in Power Electronics*, vol. 5, no. 3, pp. 1356–1376, Sept 2017.
- [111] National Grid, "System Operability Framework 2016," Tech. Rep., 2016.

Appendix A

Network Data of Test Systems

This appendix will provide the data required in order to perform dynamic studies on the test systems used throughout this thesis. The parameters for Kundur's two area test system, IEEE 9-Bus and IEEE 39-Bus test systems that were used to perform simulations for this research.

A.1 Kundur's Two-Area Test System

Original data of the test system is adopted from Power System Stability and Control by P. Kundur. [56]

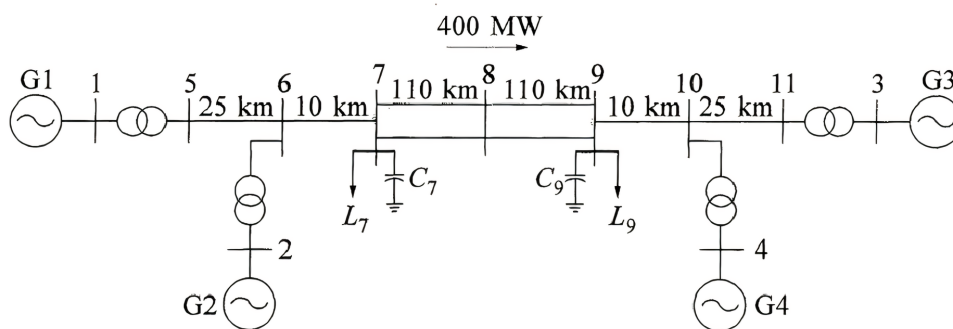


Figure A-1: Single line diagram of Kundur's two area test system.

The line impedance data for the network is presented in Table A-1. Load flow data is included in Table A-2.

A.2 IEEE 9-Bus Test System

Table A-1: Line data for the Kundur's two-area test network

From bus	To bus	R (pu)	X (pu)	B(pu)
1	5	0	0.15/9	0
2	6	0	0.15/9	0
3	11	0	0.15/9	0
4	10	0	0.15/9	0
5	6	25x0.0001	25x0.001	25x0.00175
10	11	25x0.0001	25x0.001	25x0.00175
6	7	10x0.0001	10x0.001	10x0.00175
9	10	10x0.0001	10x0.001	10x0.00175
7	8	110x0.0001	110x0.001	110x0.00175
7	8	110x0.0001	110x0.001	110x0.00175
8	9	110x0.0001	110x0.001	110x0.00175
8	9	110x0.0001	110x0.001	110x0.00175

Table A-2: Load flow data for the Kundur's two-area test network

Bus	V(pu)	P_G (MW)	P_L (MW)	Q_L (MVar)	Q_C (MVar)
1	1.03	-	-	-	-
2	1.01	700	-	-	-
3	1.03	719	-	-	-
4	1.01	700	-	-	-
7	-	-	967	100	200
9	-	-	1767	200	350

Table A-3: Generator dynamic data for the Kundur's two-area test network

Generator	Rating (MVA)	X_d (pu)	X'_d (pu)	X''_d (pu)	X'_{d0} (pu)	X''_{d0} (pu)	X'_q (pu)	X''_q (pu)	X'_{q0} (pu)	X''_{q0} (pu)	H (s)
G1	900	1.8	0.3	0.25	8	0.03	1.7	0.25	0.4	0.05	6.5
G2	900	1.8	0.3	0.25	8	0.03	1.7	0.25	0.4	0.05	6.5
G3	900	1.8	0.3	0.25	8	0.03	1.7	0.25	0.4	0.05	6.175
G4	900	1.8	0.3	0.25	8	0.03	1.7	0.25	0.4	0.05	6.175

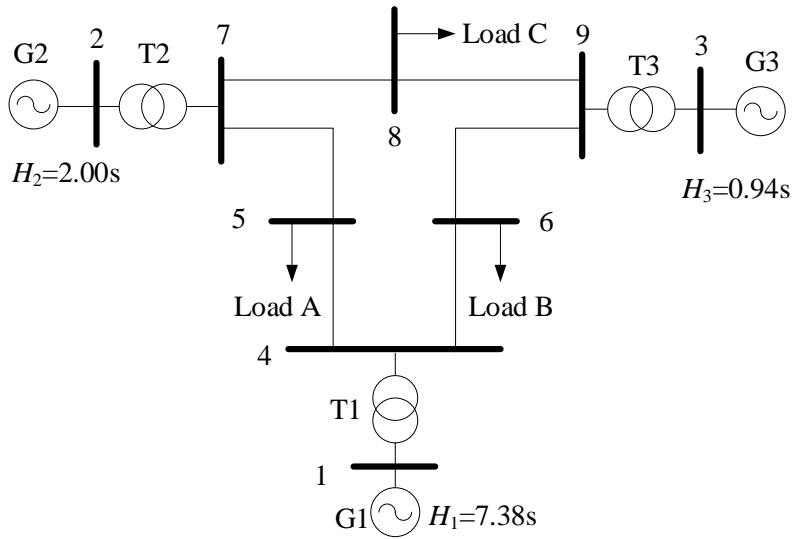


Figure A-2: Single line diagram of IEEE 9-bus test system.

Table A-4: Synchronous machine parameters

	SM1	SM2	SM3
Nominal Power (MVA)	512	270	125
Nominal Voltage (kV RMS L-L)	24	18	15.5
X_d (pu)	1.7	1.7	1.22
X'_d (pu)	0.27	0.256	0.174
X''_d (pu)	0.2	0.185	0.134
T'_{do} (s)	3.8	4.8	8.97
T''_{do} (s)	0.01	0.01	0.033
X_q (pu)	1.65	1.62	1.16
X'_q (pu)	0.47	0.245	0.25
X''_q (pu)	0.2	0.185	0.134
T'_{qo} (s)	0.48	0.5	0.5
T''_{qo} (s)	0.0007	0.0007	0.07
R_a (pu)	0.004	0.0016	0.004
X_l (pu)	0.16	0.155	0.0078
$S(1.0)$	0.09	0.125	0.1026
$S(1.2)$	0.4	0.45	0.432
H (s)	2.6312	4.1296	4.768
D (pu)	2	2	2

Table A-5: Exciter parameters

	SM1	SM2	SM3
Kp	5.3	5.3	5.3
Ka	200	30	25
Kf	0.0635	0.05	0.108
Tr (s)	0	0	0.06
Ta (s)	0.395	0.4	0.2
Tf (s)	1	1.3	0.35
Vt min (pu)	0.1	0.1	0.1
Vt max (pu)	100	100	100
Vr min (pu)	-3.84	-4.59	-3
Vr max (pu)	3.84	4.59	3

Table A-6: Transformer parameters

	T1	T2	T3
Nominal primary voltage (kV RMS L-L)	24	18	15.5
Nominal secondary voltage (kV RMS L-L)	230	230	230
R1 (pu)	1.00E-10	1.00E-10	1.00E-10
L1 (pu)	2.88E-02	3.13E-02	2.93E-02
R2 (pu)	1.00E-10	1.00E-10	1.00E-10
L2 (pu)	2.88E-02	3.13E-02	2.93E-02
Rm (pu)	5.00E+03	5.00E+03	5.00E+03
Lm (pu)	5.00E+03	5.00E+03	5.00E+03
Vr min (pu)	-3.84	-4.59	-3
Vr max (pu)	3.84	4.59	3

Table A-7: Line parameters

Line From	To	Length(km)	R0(o/km)	L0(H/km)	C0 (F/km)	R1 (o/km)	L1 (H/km)	C1 (F/km)
4	5	89.93	5.88E-01	3.98E-03	5.89E-09	5.88E-02	1.33E-03	9.81E-09
4	6	97.336	9.24E-01	3.98E-03	4.88E-09	9.24E-02	1.33E-03	8.14E-09
5	7	170.338	9.94E-01	3.98E-03	5.41E-09	9.94E-02	1.33E-03	9.01E-09
6	9	179.86	1.15E+00	3.98E-03	5.99E-09	1.15E-01	1.33E-03	9.98E-09
7	8	76.176	5.90E-01	3.98E-03	5.89E-09	5.90E-02	1.33E-03	9.81E-09
8	9	106.646	5.90E-01	3.98E-03	5.90E-09	5.90E-02	1.33E-03	9.83E-09

Table A-8: Load parameters

	Load5	Load6	Load8
Nominal Active Power (MW)	125	90	100
Nominal Reactive Power (MVar)	50	30	35

A.3 IEEE 39-Bus Test System

IEEE 39-Bus system is a reduced equivalent of the New England test system (NETS) [103].

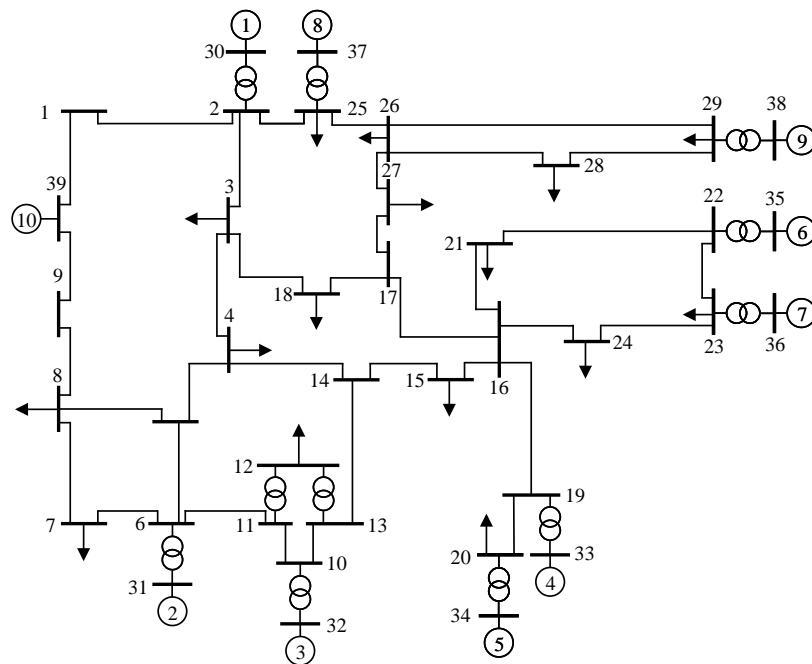


Figure A-3: Single line diagram of IEEE 39-bus test system.

Table A-9: Transformer Data

From BUS	To BUS	R (pu)	X (pu)	Tap Ratio
12	11	0.0016	0.0435	1.006
12	13	0.0016	0.0435	1.006
6	31	0	0.0250	1.070
10	32	0	0.0200	1.070
19	33	0.0007	0.0142	1.070
20	34	0.0009	0.0180	1.009
22	35	0	0.0143	1.025
23	36	0.0005	0.0272	1.000
25	37	0.0006	0.0232	1.025
2	30	0	0.0181	1.025
29	38	0.0008	0.0156	1.025
19	20	0.0007	0.0138	1.060

Table A-10: Bus Data

BUS	Type	—V— (pu)	PGEN (MW)	PLOAD (MW)	QLOAD (MVar)
1	P-Q	-	-	-	-
2	P-Q	-	-	-	-
3	P-Q	-	-	322	2.4
4	P-Q	-	-	500	184
5	P-Q	-	-	-	-
6	P-Q	-	-	-	-
7	P-Q	-	-	233.8	84
8	P-Q	-	-	522	176
9	P-Q	-	-	-	-
10	P-Q	-	-	-	-
11	P-Q	-	-	-	-
12	P-Q	-	-	7.5	88
13	P-Q	-	-	-	-
14	P-Q	-	-	-	-
15	P-Q	-	-	320	153
16	P-Q	-	-	329	32.3
17	P-Q	-	-	-	-
18	P-Q	-	-	158	30
19	P-Q	-	-	-	-
20	P-Q	-	-	628	103
21	P-Q	-	-	274	115
22	P-Q	-	-	-	-
23	P-Q	-	-	247.5	84.6
24	P-Q	-	-	308.6	-92
25	P-Q	-	-	224	47.2
26	P-Q	-	-	139	17
27	P-Q	-	-	281	75.5
28	P-Q	-	-	206	27.6
29	P-Q	-	-	283.5	26.9
30	P-V	1.0475	250	-	-
31	SLACK	0.9820	-	9.2	4.6
32	P-V	0.9831	650	-	-
33	P-V	0.9972	632	-	-
34	P-V	1.0123	508	-	-
35	P-V	1.0493	650	-	-
36	P-V	1.0635	560	-	-
37	P-V	1.0278	540	-	-
38	P-V	1.0265	830	-	-
39	P-V	1.0300	1000	1104	250

Table A-11: Transmission Line Data

From BUS	To BUS	R (pu)	X (pu)	B (pu)
1	2	0.0035	0.0411	0.6987
1	39	0.0010	0.0250	0.7500
2	3	0.0013	0.0151	0.2572
2	25	0.0070	0.0086	0.1460
3	4	0.0013	0.0213	0.2214
3	18	0.0011	0.0133	0.2138
4	5	0.0008	0.0128	0.1342
4	14	0.0008	0.0129	0.1382
5	6	0.0002	0.0026	0.0434
5	8	0.0008	0.0112	0.1476
6	7	0.0006	0.0092	0.1130
6	11	0.0007	0.0082	0.1389
7	8	0.0004	0.0046	0.0780
8	9	0.0023	0.0363	0.3804
9	39	0.0010	0.0250	1.2000
10	11	0.0004	0.0043	0.0729
10	13	0.0004	0.0043	0.0729
13	14	0.0009	0.0101	0.1723
14	15	0.0018	0.0217	0.3660
15	16	0.0009	0.0094	0.1710
16	17	0.0007	0.0089	0.1342
16	19	0.0016	0.0195	0.3040
16	21	0.0008	0.0135	0.2548
16	24	0.0003	0.0059	0.0680
17	18	0.0007	0.0082	0.1319
17	27	0.0013	0.0173	0.3216
21	22	0.0008	0.0140	0.2565
22	23	0.0006	0.0096	0.1846
23	24	0.0022	0.0350	0.3610
25	26	0.0032	0.0323	0.5130
26	27	0.0014	0.0147	0.2396
26	28	0.0043	0.0474	0.7802
26	29	0.0057	0.0625	1.0290
28	29	0.0014	0.0151	0.2490

Appendix B

List of Publications

Journal

1. Sun, M., Feng, Y., Wall, P., Azizi, S., Yu, J., & Terzija, V. (2019). On-line power system inertia calculation using wide area measurements, in *International Journal of Electrical Power & Energy Systems*, 109, 325–331. Accepted
2. Sun, M., Azizi, S., Liu, G. Popov, M., & Terzija, V. Underfrequency Load Shedding using Locally Estimated RoCoF of the Center of Inertia, in *IEEE Transaction on Power System*. Under review
3. Azizi, S., Sun, M., Liu, G. & Terzija, V. Local Frequency-Based Estimation of the Rate of Change of Frequency of the Center of Inertia, in *IEEE Power Engineering Letters*. Accepted
4. Liu, G., Azizi, S., Sun, M., Popov, M., & Terzija, V. (2018). Performance of out-of-step tripping protection under renewable integration, in *The Journal of Engineering*, 2018(15), 1216–1222. <https://doi.org/10.1049/joe.2018.0180> Accepted
5. Azizi, S., Sun, M., Liu, G., Popov, M., & Terzija, V. High-Speed Distance Relaying of the Entire Length of Transmission Lines without Signaling, in *IEEE Transactions on Power Delivery*, doi: 10.1109/TPWRD.2019.2957302. Accepted
6. Hong, Q., Karimi, M., Sun, M., Norris, S., Bagleybter, O. Design and Validation of a Wide Area Monitoring and Control System for Fast Frequency Response, in

IEEE Transactions on Smart Grid, vol. 11, no. 4, pp. 3394-3404, July 2020, doi: 10.1109/TSG.2019.2963796. Accepted

Conference

1. Azizi, S., Sun, M., Popov, M., & Terzija, V. (2019). Non-communication Accelerated Sequential Tripping for Remote-End Faults on Transmission Lines, in *IEEE Milan PowerTech, 2019* Accepted
2. Hong, Q., Norris, S., Sun, M., Bagleybter, O., & Terzija, V. Application of Wide-Area and Monitoring and Control Techniques for Fast Frequency Control in Power Systems with Low Inertia, in *CIGRE Paris Session, 2020*. Accepted